



## Durham E-Theses

---

### *Cross-sections for neutral channels in $K P$ interactions between 1470 and 1560 MeV C.M. energy*

Fallahi, Mohammad Taghi

#### How to cite:

---

Fallahi, Mohammad Taghi (1978) *Cross-sections for neutral channels in  $K P$  interactions between 1470 and 1560 MeV C.M. energy*, Durham theses, Durham University. Available at Durham E-Theses Online: <http://etheses.dur.ac.uk/8416/>

#### Use policy

---

The full-text may be used and/or reproduced, and given to third parties in any format or medium, without prior permission or charge, for personal research or study, educational, or not-for-profit purposes provided that:

- a full bibliographic reference is made to the original source
- a [link](#) is made to the metadata record in Durham E-Theses
- the full-text is not changed in any way

The full-text must not be sold in any format or medium without the formal permission of the copyright holders.

Please consult the [full Durham E-Theses policy](#) for further details.

---

Academic Support Office, Durham University, University Office, Old Elvet, Durham DH1 3HP  
e-mail: [e-theses.admin@dur.ac.uk](mailto:e-theses.admin@dur.ac.uk) Tel: +44 0191 334 6107  
<http://etheses.dur.ac.uk>

The copyright of this thesis rests with the author.  
No quotation from it should be published without  
his prior written consent and information derived  
from it should be acknowledged.

CROSS-SECTIONS FOR NEUTRAL CHANNELS IN

$K^-P$  INTERACTIONS BETWEEN

1470 and 1560 MeV C.M. ENERGY

by

MOHAMMAD TAGHI FALLAHI, M.Sc.

Graduate Society

A thesis submitted to the University of Durham

in candidature for the degree of

Doctor of Philosophy

April 1978



## ABSTRACT

The results presented in this thesis are from the preliminary data on a  $K^-P$  formation experiment. The experiment was carried out at the Rutherford Laboratory using the British National Hydrogen bubble chamber with a Track Sensitive Target (T.S.T.) to afford gamma-ray detection. The final states selected for the analysis are  $\Lambda^0\pi^0$ ,  $\Sigma^0\pi^0$  and  $\bar{K}^0n$  at incident momenta between 200 and 500  $\frac{\text{MeV}}{c}$ .

The T.S.T. technique employed in this experiment is discussed in detail, in particular its limitations and how they should be handled are described.

The cross-sections for  $\Lambda^0$  + neutrals,  $\Lambda^0\pi^+\pi^-$  and  $\bar{K}^0n$  channels are obtained in 20  $\frac{\text{MeV}}{c}$  momentum intervals and the presence of the  $\Lambda(1520)$  is quite clear. The kaon flux is determined by using the observed tau-decays.

The data is divided into 6 intervals of incident momentum between 250 and 500  $\frac{\text{MeV}}{c}$  and fits are made to the distribution of missing mass squared to the  $\Lambda^0$ -hyperon, the production angular distribution and the polarisation of the  $\Lambda^0$ . These fits gave the Legendre expansion coefficients describing the angular distributions and the polarisations for the  $\Lambda^0\pi^0$  and  $\Sigma^0\pi^0$  final states. The results are in good agreement with the previous data.

Finally events fitted as  $\Lambda^0\pi^0$  and  $\Sigma^0\pi^0$  hypotheses with one associated gamma-ray are chosen. Here the gamma-ray is used to resolve the  $\Lambda^0/\Sigma^0$  ambiguity. The observed production angular distributions for these events are compared with the results from the fit above using  $\Lambda^0$  and  $\Sigma^0$  events without gamma-rays. Also, the decay proton angular distribution of the fitted  $\Sigma^0\pi^0$  events is compared with the results from the fit. There is a good consistency between the two results and that of the previous data.

## CONTENTS

	<u>Page No.</u>	
CHAPTER 1	INTRODUCTION	1
	1.1 Review of low-energy $K^-p$ interactions	2
	1.2 Motivation of the experiment	8
	1.3 The present experiment	10
	1.4 Bubble Chamber Technique and Track Sensitive Target	11
	1.5 Outline of the Thesis	14
CHAPTER 2	EXPERIMENTAL DETAILS (I)	16
	2.1 The British National Hydrogen Bubble Chamber	16
	2.2 Description of Track Sensitive Target (T.S.T.)	16
	2.3 The Exposure	18
	2.4 The Beam	18
	2.5 Contamination of the Beam	19
	2.6 Limitation of the T.S.T. Chamber	20
	2.7 Precision of the T.S.T. Chamber	22
CHAPTER 3	EXPERIMENTAL DETAILS (II)	27
	3.1 Scanning of Events	27
	3.2 Measuring of Events	30
	3.2.1 Accuracy of the Measuring System	31
	3.3 Processing of Events	34
	3.3.1 REAP	34
	3.3.2 TRANS	34
	3.3.3 Geometrical Reconstruction	35
	3.3.4 Kinematic fitting	37
	3.3.5 Judge	38
	3.3.6 Data Summary Tape (D.S.T.)	40
	3.3.7 Masterlist	40
CHAPTER 4	BASIC EXPERIMENTAL DATA	41
	4.1 Scanning	41
	4.1.1 Scanning Efficiencies	41
	4.2 Measurement	43
	4.3 Gamma Rays Detection Efficiency	43
	4.4 Gamma Conversion Length	45
	4.5 Calibration of The Magnetic Field	46
	4.6 Reconstruction Accuracy in the T.S.T. Stretch Distribution of tau-mesons	48

4.6.1	Importance, if any, of non-zero stretch	49
4.6.2	Causes of non-zero stretch on $\tan \lambda$	50
4.7	Conclusion	52
CHAPTER 5	EVENT SELECTION AND ABSOLUTE CROSS-SECTIONS	53
5.1	Kinematical Fitting	54
5.2	Data Selection	55
5.3	Determination of Tracklength from tau-mesons	57
5.3.1	Determination of $N(L,P)$	58
5.4	Unbiased Acceptance of Events	64
5.5	Selection of Unbiased $\Lambda^0$ 's Sample	65
5.6	Correction factors	69
5.7	Selection of unbiased $\bar{K}^0$ events	71
5.8	Cross-section Evaluation	72
CHAPTER 6	DIFFERENTIAL CROSS-SECTIONS AND POLARISATIONS IN THE NEUTRAL CHANNELS	75
6.1	Separating $\Lambda^0 \pi^0$ and $\Sigma^0 \pi^0$ Channels	75
6.2	Angular Distribution Expansion Coefficients	80
6.3	Polarisation Expansion Coefficients	86
6.4	The $\Lambda^0 \pi^0$ and $\Sigma^0 \pi^0$ constrained channels	91
6.4.1	Separating the Ambiguous $\Lambda^0 \pi^0 / \Sigma^0 \pi^0$ constrained channels	91
6.4.2	Angular Distribution	92
6.4.3	Polarisation	93
CHAPTER 7	GENERAL CONCLUSIONS	96
APPENDIX A		99
APPENDIX B		101
APPENDIX C		105
APPENDIX D		108
APPENDIX E		110
REFERENCES		113

## CHAPTER 1

### INTRODUCTION

During recent years several experiments have been carried out to study  $K^-p$  interactions at low energy. Looking first at the status of bubble chamber experiments, in Figure 1.1 a summary of the exposures taken place below  $2 \frac{\text{GeV}}{c}$  is shown. The ordinate is number of events per millibarn per  $25 \frac{\text{MeV}}{c}$  momentum interval. These experiments are all of the so-called formation type. As can be seen, above  $650 \frac{\text{MeV}}{c}$  incident momentum experiments have been carried out at a level of at least 1000 events/mb per  $25 \frac{\text{MeV}}{c}$ . In the Tripp series of experiments (LBL 1965), this level reaches about 3000 events/mb per  $25 \frac{\text{MeV}}{c}$  over a region of 350 to  $450 \frac{\text{MeV}}{c}$  incident momentum. However, it is noticeable that in the region of 450 to  $650 \frac{\text{MeV}}{c}$ , not only the number of experiments carried out is quite small, but these are also relatively low-statistics experiments. The situation, from the point of view of the statistics, gets worse below  $150 \frac{\text{MeV}}{c}$ . The conclusion is, therefore, that above primary momenta of about  $650 \frac{\text{MeV}}{c}$  the interaction of negative kaons with nucleons have been investigated comparatively well experimentally. Below this value of momentum the number of experiments that has been performed is quite low so that correspondingly the availability of good experimental data is poor.

A major problem with low-momentum exposures stems from difficulty in constructing low-momentum  $K^-$ -beams of high intensity and well-defined momentum. Otherwise, counter experiments could be employed to accumulate high statistics. Even so, the detailed processes would have to be left to bubble chamber experiments. One reason for this is that in each of the final states produced as a result of  $K^-p$  interaction there is one



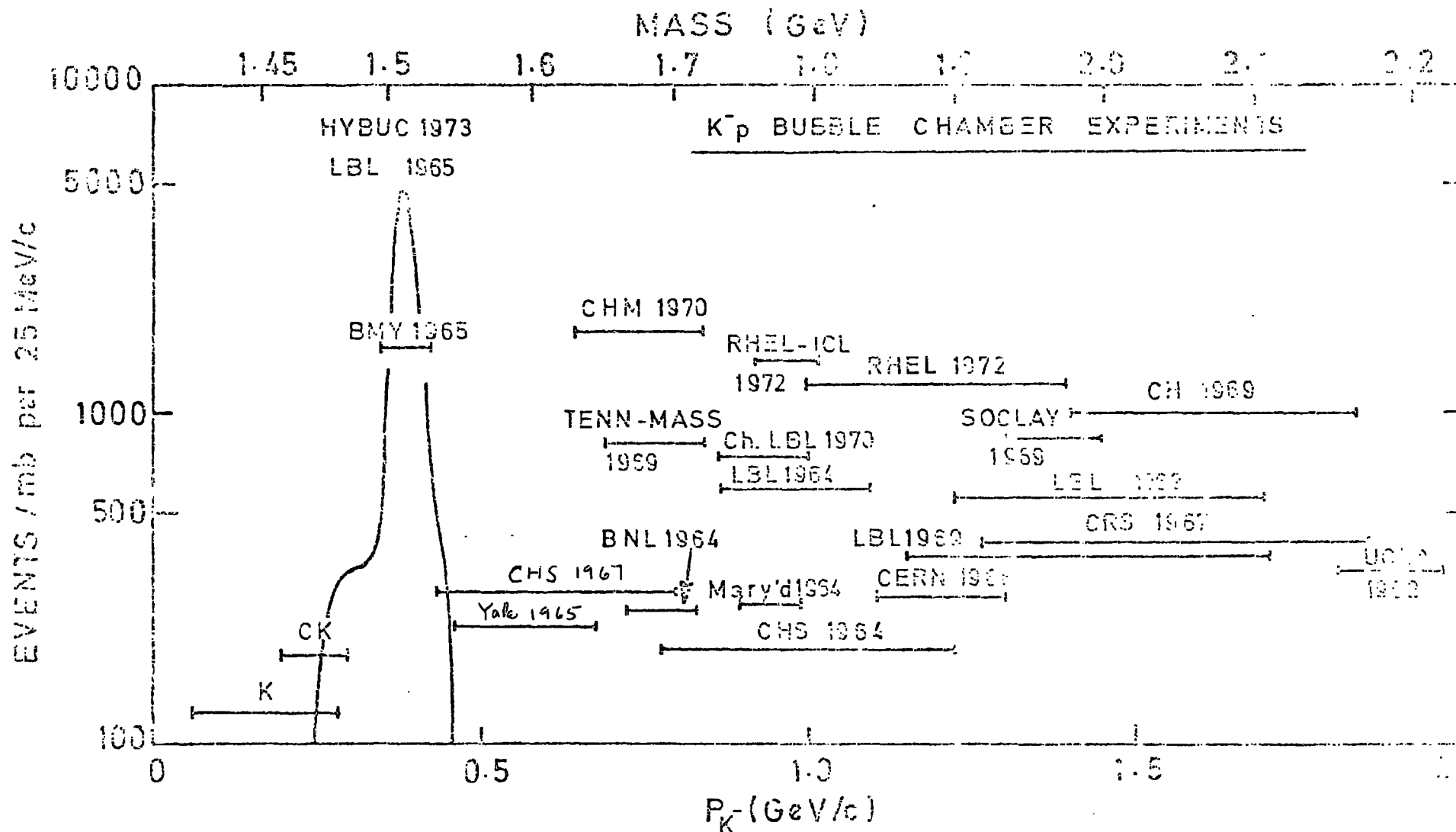


FIG. 1-1  $K^-p$  bubble chamber path lengths below 2 GeV/c. Numbers refer to the approximate date of the exposure. Horizontal lines show the momentum interval and the average level of the exposure over that interval. The path length is averaged over the indicated momentum interval of the experiment (except for LBL 1965). References are given in Ref. (1-21).

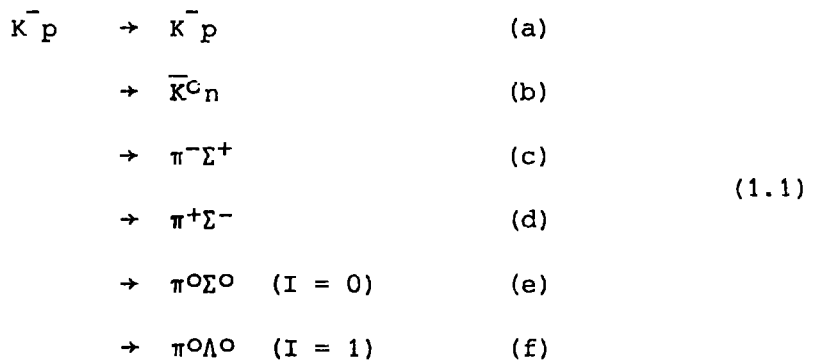


particle with a rather short lifetime (see reactions listed in 1.1) which makes the use of counter techniques very difficult. However, handling of low-energy interactions in bubble chambers is very difficult too. For example, effects like rapid energy loss makes the determination of momentum difficult and/or leads to short-length tracks which are difficult to detect and measure. For experiments below  $150 \frac{\text{MeV}}{c}$ , there is an absolute need for a very well-defined momentum so that the beam momentum at the point of interaction is determined by its position in the chamber and not by direct measurement. As a result of these difficulties all the data available for incident momentum below  $150 \frac{\text{MeV}}{c}$  come from at-rest interactions; there are no in-flight data. Moreover, with the development of accelerating machines of higher and higher energies the main interest of investigators has moved away from physics of low-energy interactions or even higher energies of the order of tens of GeV to hundreds of GeV.

Consequently, it is clear that just from the point of view of adequate statistics, experiments are needed in the range below  $\sim 350 \frac{\text{MeV}}{c}$  and between 450 to 650  $\frac{\text{MeV}}{c}$   $K^-$ -laboratory momentum. Apart from the "adequate statistics" point of view, there are also compelling reasons from the physics point of view. These will emerge as a series of problems in Section 1.2 below.

### 1.1 Review of low-energy $K^-p$ interactions

The main channels in low-energy  $K^-p$  interactions are:



Multipion final states of the  $K^-p$  interactions are possible but, apart from  $\Lambda^0\pi^+\pi^-$  channel in the region of  $\Lambda(1520)$ , their contribution at low momentum to the total interaction cross-section is negligible.

All the reactions (a) to (f) have been studied in different experiments. The first large statistics experiment below  $280 \frac{\text{MeV}}{c} K^-$ -laboratory moment was made by Humphrey and Ross (ref. 1.1). A similar analysis was later carried out by Kim (ref. 1.2) in an experiment with about 10 times larger statistics. Experimental cross-sections and angular distributions for the reactions (a) to (f) as well as  $\Sigma^-:\Sigma^+:\Sigma^0:\Lambda^0$  branching ratios at rest were obtained in the two experiments. The experimental results were then fitted to the Dalitz-Tuan theory (ref. 1.3) which assumes that the effective range is zero for  $K^-p$ -system. This theory is briefly reviewed below.

From SU2, the  $K^-p$  system has equal amplitude in the isotopic spin states  $I = 0$  and  $1$

$$|K^-p\rangle = \frac{1}{\sqrt{2}} |I_0\rangle + \frac{1}{\sqrt{2}} |I_1\rangle$$

Here  $I_0$  and  $I_1$  are the isotopic spin 0 and 1 states respectively. In the first four reactions listed above, both isotopic spin states are involved. The neutral channels, leading to  $\Sigma^0$  and  $\Lambda^0$  production are respectively pure isotopic spin 0, or isotopic spin 1 reactions. With charge independence, the isotopic spin eigenstates for the  $\bar{K}N$  system are:

$$\begin{aligned} \psi_0 &= \frac{1}{\sqrt{2}} \left[ |K^-p\rangle - |\bar{K}^0n\rangle \right] \\ \psi_1 &= \frac{1}{\sqrt{2}} \left[ |K^-p\rangle + |\bar{K}^0n\rangle \right] \\ \phi_0 &= \frac{1}{\sqrt{3}} \left[ |\Sigma^+\pi^-\rangle - |\Sigma^0\pi^0\rangle + |\Sigma^-\pi^+\rangle \right] \\ \phi_1 &= \frac{1}{\sqrt{2}} \left[ |\Sigma^+\pi^-\rangle - |\Sigma^-\pi^+\rangle \right] \\ \chi_1 &= |\Lambda^0\pi^0\rangle \end{aligned}$$

From these, and knowing reaction amplitudes, the cross-sections are:

$$\sigma_{K^-p} = 4\pi \left| \frac{\frac{1}{2}(A_1 + A_0) - iKA_0A_1}{(1 - iKA_0)(1 - iKA_1)} \right|^2$$

$$\sigma_{K^0n} = 4\pi \left| \frac{\frac{1}{2}(A_1 - A_0)}{(1 - iKA_0)(1 - iKA_1)} \right|^2$$

$$\sigma_{\Sigma^+\pi^-} = \frac{4\pi q_L}{K} \left| \frac{1}{\sqrt{6}} \frac{M_0}{1 - iKA_0} + \frac{1}{2} \frac{M_1}{1 - iKA_1} \right|^2$$

$$\sigma_{\Sigma^-\pi^+} = \frac{4\pi q_\Sigma}{K} \left| \frac{1}{\sqrt{6}} \frac{M_0}{1 - iKA_0} - \frac{1}{2} \frac{M_1}{1 - iKA_1} \right|^2$$

$$\sigma_{\Sigma^0\pi^0} = \frac{4\pi q_\Sigma}{K} \left| \frac{1}{\sqrt{6}} \frac{M_0}{1 - iKA_0} \right|^2$$

$$\sigma_{\Lambda^0\pi^0} = \frac{4\pi q_\Lambda}{K} \left| \frac{1}{\sqrt{2}} \frac{N_1}{1 - iKA_1} \right|^2$$

where

$A_0, A_1$  = the complex scattering lengths for  $I = 0$  and  $I = 1$  channels ( $A_0 = a_0 + ib_0$ ,  $A_1 = a_1 + ib_1$ ) assumed constant over the momentum region.

$M_0, M_1, N_1$  = reaction amplitudes for  $(\Sigma\pi)_{I=0}$ ,  $(\Sigma\pi)_{I=1}$  and  $\Lambda^0\pi^0$  final states.

$q_\Sigma, q_\Lambda$  = centre of mass momenta of the hyperons ( $\Sigma$  and  $\Lambda$ )

$K$  = centre of mass momentum of  $K^-$ .

As mentioned earlier, these cross-sections are based on the charge-independence assumption. In practice, however, these are modified by the

effects arising from the electromagnetic interactions which give a measure of the breakdown of charge independence. One such effect is the mass difference of ( $K^-$ ,  $\bar{K}^0$ ) and (p,n) which makes the charge-exchange reaction impossible below  $\sim 90 \frac{\text{MeV}}{C}$   $K^-$ -laboratory momentum. Another effect is that of the  $K^-p$  Coloumb interactions which is expected to become important at low energy. When this latter correction is formulated it leads to about 8% correction to the elastic scattering cross-section at  $\sim 100 \frac{\text{MeV}}{C}$  and 2% correction at  $\sim 400 \frac{\text{MeV}}{C}$ . To the precision of most experiments these corrections are not important. However, taking into account these effects, the cross-sections are given by

$$\frac{d\sigma_{el}}{d\Omega} = \left| \frac{\text{Csc}^2(\theta/2)}{2BK^2} \exp \left[ \frac{2i}{KB} \ln \sin(\theta/2) \right] + \frac{\frac{1}{2}C^2 (A_0 + A_1 - 2iK_0 A_0 A_1)}{D} \right|^2$$

$$\sigma_{\bar{K}^0 n} = \frac{\pi K_0}{K} \left| \frac{A_0 - A_1}{D} \right|^2$$

$$\sigma_0 = \frac{4\pi b_0}{K} \left| \frac{1 - iK_0 A_1}{D} \right|^2$$

$$\sigma_1 = \frac{4\pi b_1}{K} \left| \frac{1 - iK_0 A_0}{D} \right|^2$$

where

$$D = 1 - \frac{i}{2} (A_0 + A_1) (K + K_0) - K_0 K A_0 A_1$$

$$b_0 = c_{\Sigma} \left| M_0 \right|^2$$

$$b_1 = c_{\Sigma} \left| M_1 \right|^2 + c_{\Lambda} \left| N_1 \right|^2$$

$K_0$  is the centre of mass wave number for the charge-exchange reaction,

$\theta$  is the scattering angle,  $B$  is the Bohr radius of the  $K^-p$  system and  $C^2 = \frac{2\pi}{KB} \left[ 1 - \exp\left(-\frac{2\pi}{KB}\right) \right]^{-1}$  is the Coulomb penetration factor. The hyperon cross-sections can be expressed in terms of six parameters, four contained

in the complex scattering lengths  $A_0$  and  $A_1$  and two defined by,

$$(a) \quad \phi = \text{Arg} \left( \frac{M_0 (1 - i K_0 A_1)}{M_1 (1 - i K_0 A_0)} \right) = \phi_{th} + \text{Arg} \left( \frac{1 - i K_0 A_1}{1 - i K_0 A_0} \right)$$

where  $\phi$  is the phase difference between  $I = 0$  and  $I = 1$  amplitudes for  $\Sigma \pi$  production and  $\phi_{th} = \text{Arg} \left( \frac{M_0}{M_1} \right)$  is the phase difference at the charge-exchange threshold; and

$$(b) \quad \epsilon = \frac{q_\Lambda |N_1|^2}{q_\Sigma |M_1|^2 + q_\Lambda |N_1|^2}$$

where  $\epsilon$  is the fraction of  $I = 1$  production going via  $\Lambda$ -production.

Then,

$$\sigma_{\Sigma^+\pi^-} = \frac{1}{6} \sigma_0 + \frac{1}{4} (1 - \epsilon) \sigma_1 - \left[ \frac{1}{6} \sigma_0 \sigma_1 (1 - \epsilon) \right]^{\frac{1}{2}} \cos \phi$$

$$\sigma_{\Sigma^-\pi^+} = \frac{1}{6} \sigma_0 + \frac{1}{4} (1 - \epsilon) \sigma_1 + \left[ \frac{1}{6} \sigma_0 \sigma_1 (1 - \epsilon) \right]^{\frac{1}{2}} \cos \phi$$

$$\sigma_{\Sigma^0\pi^0} = \frac{1}{6} \sigma_0$$

and

$$\sigma_{\Lambda^0\pi^0} = \frac{1}{2} \sigma_1 \epsilon$$

The value obtained by Kim for the six parameters are as follows:

$$A_0 = (-1.67 \pm 0.04) + i(0.71 \pm 0.04) \text{ fm}$$

$$A_1 = (-0.07 \pm 0.06) + i(0.68 \pm 0.03) \text{ fm}$$

$$\epsilon = 0.31 \pm 0.02$$

$$\phi_{th} = -53.8 \text{ degrees}$$

It has been shown by Dalitz and Tuan (ref. 1.4) that if the real part of the scattering length is large and negative, and the imaginary part is small, it requires a virtual bound state below the  $\bar{K}N$  threshold,

the mass and the width of which, for  $I = 0$ , are:

$$E_r = m_p + m_{K^-} - (2\mu_K a_0^2)^{-1}$$

$$\Gamma = 2b_0 / (\mu_K |a_0|^3)$$

where  $m_p$  and  $m_{K^-}$  are the masses of proton and  $K^-$  respectively,  $\mu_K$  is the reduced mass of  $K^-p$  system,  $a_0$  and  $b_0$  are the real and imaginary parts of  $I = 0$  scattering length.

Substituting Kim's value of  $a_0$  and  $b_0$  gives

$$E_r = 1410.7 \pm 1.0 \text{ MeV}$$

$$\Gamma = 36.4 \pm 3.2 \text{ MeV}$$

These are very close to the values for  $Y_0^*$  (1405) which is to be understood as an s-wave bound state of the  $K^-p$  system.

In the region of 350 to 430 MeV/c incident  $K^-$ -laboratory momentum, Berley et al. (ref. 1.5) have published data on all neutral channels, more recently there has been a high-statistics experiment carried out by Mast et al. (ref. 1.6) in the region of 240 to 450  $\frac{\text{MeV}}{c}$  laboratory momentum in which have been examined in detail nearly all the  $K^-p$  final states in this region.

The major structure in this interval of incident  $K^-$ -momentum is the well-established  $\Lambda(1520)$  with spin  $3/2$  and negative parity (ref. 1.7) which is an isospin singlet resonance, and decays predominantly into  $N\bar{K}$  and  $\Sigma\pi$ . There has been a tentative identification of a resonance at a laboratory momentum of about 280  $\frac{\text{MeV}}{c}$ . This is the  $\Sigma(1480)$  which is classified as one star state in PDG tables (ref. 1.8).

In a multichannel phase-shift analysis, Kim (ref. 1.9) has some evidence for a resonance at 520  $\frac{\text{MeV}}{c}$  with a mass of 1570 MeV ( $P_{01}$  state)

and in an experiment performed by Armenteros et al. (ref. 1.10), there has been tentatively identified a signal at about  $480 \frac{\text{MeV}}{c}$  with a mass of 1554 MeV ( $P_{11}$  state). Recently Bowen et al. (ref. 1.11) have examined the interactions of  $K^-p$  and  $K^-n$  in hydrogen and deuterium respectively. There is evidence for a resonance in the  $\bar{K}N$ ,  $I = 1$  cross-section at about  $580 \frac{\text{MeV}}{c}$ .

## 1.2 Motivation for the experiment

From the brief survey of experiments which were carried out in the field of  $K^-p$  interaction below  $600 \frac{\text{MeV}}{c}$  incident  $K^-$ -laboratory momentum, some of the motivation for performing this experiment can be stated as follows:

(a) Cross-sections The results obtained by Kim below  $280 \frac{\text{MeV}}{c}$  are very important and the experiment giving rise to it must be examined critically. Although it is not intended to suggest that these results are wrong, there are many features of the Kim work which raise doubts about its overall accuracy. From the point of view of working at very low momenta, there is no evidence that energy loss is properly taken into account in determining momenta. Indeed primary momenta are quoted which correspond to Kaon of zero-range and could not be measured. Where the data from the experiment can be compared in detail with other experiments inconsistencies appear.

For example, the ratio of the transition rate

$$\gamma = \frac{K^-p \rightarrow \Sigma^- \pi^+}{K^-p \rightarrow \Sigma^+ \pi^-}$$

for events produced at rest is determined by Kim to be  $2.06 \pm 0.06$  whereas the value obtained by Tovee et al. (ref. 1.12), using emulsions, is  $2.40 \pm 0.06$ .

In the analysis by A.D. Martin (ref. 1.13) using dispersion relation to link higher and low momentum data for both  $K^+$  and  $K^-$  interactions, discrepancies were again noted in the Kim data. For these reasons it is clear that there should be an independent experiment and analysis of the low-momentum Kaon interactions below about  $300 \frac{\text{MeV}}{c}$ . This requires good determination of the cross-sections.

(b) Resonance Production As mentioned before, in the momentum region below  $600 \frac{\text{MeV}}{c}$  incident  $K^-$ -laboratory momentum, only the general behaviour of the resonant  $D_{03}$  amplitude,  $\Lambda(1520)$ , is fairly well understood. The existence of others like  $\Sigma(1480)$ ,  $P_{01}$  and  $P_{11}$  states as described in the previous section and the one predicted at  $580 \frac{\text{MeV}}{c}$  momentum is still in doubt. Therefore, higher statistics experiments of good quality are required to clarify the situation of the existence of resonances other than the  $\Lambda(1520)$  in the low-momentum region.

(c) Partial Waves The angular distribution at low momenta are, obviously, consistent with being purely S-wave. At about  $400 \frac{\text{MeV}}{c}$  incident momentum, the D-wave  $\Lambda(1520)$  is strongly produced. However, the uncertainty still remains concerning the onset of P- and D-wave amplitudes. This needs to be known to delineate the region in which Kim analysis (S-wave analysis) is valid and it requires well-founded angular distributions. The examination of polarisations for the weakly decaying  $\Sigma^0$  and  $\Lambda^0$  hyperons will lead to the examination of the interference of the partial waves and to the onset of p-waves.

(d)  $\Lambda^0/\Sigma^0$  ambiguity Reactions (e) and (f) of those listed in 1.1 are pure isospin  $I = 0$  and  $I = 1$  channels respectively. In other words, the production of the  $\Lambda(1520)$  should be seen only in the  $\Sigma^0 \pi^0$  channel and the existence or otherwise of the  $I = 1$  resonances described earlier



(e.g.  $\Sigma(1480)$ ) should be seen in the  $\Lambda^0$ -production only. The problem arises from the fact that, although the  $\Lambda^0$  is clearly identified in the bubble chamber, whether the  $\Lambda^0$  is produced directly (in  $\Lambda^0\pi^0$  or  $\Lambda^0\pi^0\pi^0$  channels) or indirectly through the decay of  $\Sigma^0$  is much less clearly resolved. This is the well-known  $\Lambda^0/\Sigma^0$  ambiguity and can only be resolved if the gamma-rays associated with the production of the  $\Lambda^0$  and  $\Sigma^0$  through the accompanying  $\pi^0$ -meson, and the gamma-ray from the  $\Sigma^0$  decay are observed. In the previous experiments (e.g. ref. 1.5), this ambiguity has been resolved only by applying a selection to the distribution of missing mass squared to the  $\Lambda^0$ -hyperon. Unfortunately the data have a considerable background from  $\Lambda^0\pi^0$  and  $\Lambda^0\pi^0\pi^0/\Sigma^0\pi^0$  channels which make the result biased. The experiments in a heavy liquid bubble chamber would help resolve the ambiguity but at the same time the uncertainty of the target introduces another ambiguity. Consequently an experiment in hydrogen with good gamma-detection is really needed.

### 1.3 The Present Experiment

This is an exposure of high statistics in a track sensitive target (T.S.T.) bubble chamber described in detail in Section 1.4 of this chapter and also in Chapter 2. In the T.S.T., Kaon interactions can only occur on protons and the surrounding neon-hydrogen chamber will improve gamma-ray detection by a factor of 20 over a conventional hydrogen bubble chamber.

The high-statistics should lead to the determination of cross-sections with good precision and to angular distributions and polarisations of fair precision. The enhanced gamma-conversion should help towards the unambiguous investigation of the separated  $I = 0$  and  $I = 1$  channels. Special attention needs to be given to the determination of low-momenta and to the correction for tracks too short to be seen.

Using a composite chamber for the first time, the technique has to be proved and it has to be demonstrated that what technical problems it introduces are well identified and understood. Because of this it is essential to have a clear, well-known signal such as the  $\Lambda(1520)$  to establish the validity of the technique.

The experiment is in three phases. Firstly the technique has to be demonstrated to work satisfactorily. Its limitations are to be found and properly handled. It is tested by showing that the determination of cross-sections, angular distributions and polarisations in the region of the well-known  $\Lambda(1520)$  do not lead to systematic differences. The work done in this thesis is concerned with this phase of the experiment through the study of all neutral channels.

The second phase is to re-examine the data at low-momentum and to repeat the six parameter analysis of Kim and check the results with the Martin Analysis using dispersion relations.

The third phase is to examine little investigated regions from 450 to  $650 \frac{\text{MeV}}{c}$  incident momentum and to check the existence or otherwise of the  $I = 1$  resonances.

#### 1.4 Bubble Chamber Technique and Track Sensitive Target

To perform an experiment at low momenta as described above in which channels have to be identified clearly requires a technique such as the bubble chamber. The conventional hydrogen/deuterium bubble chamber has become one of the most common detectors for collecting data in high energy physics. Charged particles are detected isotropically in a  $4\pi$  solid angle in this instrument and their trajectories are defined by paths of bubbles which are of the order of a few hundred microns in radius. The chamber has good spatial resolution of better than one millimetre and permits all details of the whole event including the interaction point

to be detected. This is very important in the study of events in which short lived particles are produced and in particular this becomes vital at low energies where the decay lengths of the unstable particles are comparatively short. The chamber has also high spatial precision and measured points can be reconstructed in space with an error which is typically of the order of 100 microns despite errors of reconstruction and errors associated with the chamber such as movement in the liquid. Finally the liquid used in the chamber can be chosen according to the requirements of an experiment. In particular if the chamber is filled with hydrogen there is no ambiguity over the nature of the target nucleon. There are of course, despite all the above merits, some disadvantages associated with the technique, the main ones are as follows:

(a) Because of the low cycling rate of the conventional chamber, about one expansion per second combined with a maximum number of tracks per picture of about 15, the data taking rate is extremely small for low cross section processes. Moreover, unlike the cloud chamber whose expansion can be counter controlled, the expansion of the bubble chamber cannot be triggered on specific reactions and so the collection of the data is non-selective. For example, in an experiment based on  $5 \times 10^5$  pictures with  $\sim 10$  metre track per frame, one can extract only  $\sim 200$  events for a  $10 \mu\text{b}$  cross-section. Lack of selectivity has led to the design of the rapid cycling bubble chamber to be used in conjunction with external counter systems. The external counter system decides if a photograph of the expanded chamber will be taken. In this way, the combination of the merits of the conventional bubble chamber and the electronic counters enables the system to be triggered selectively and to obtain with a high rate of expansions ( $\sim 30$  per sec.) large statistics for small cross-section processes. In this way the rapid cycling technique can come

within about a factor of 20 of the electronic spectrometers. Details of this technique can be found in reference (1.14).

(b) The conventional chamber is inefficient at detecting gamma-rays which arises from the long conversion length ( $\sim 10$  m) for gamma-rays into electron-positron pairs in hydrogen/deuterium liquid. This lack of detection prevents  $\Lambda^0/\Sigma^0$  particles from being directly identified and therefore makes it impossible to analyse kinematically events with more than one neutral particle in their final states. This problem gives rise to a limitation on the technique at high energies where the multi-neutral channels represent a large proportion of the events. At low energies, although the technique has been very successful where the proportion of the number of events containing one or more neutral particles is comparatively large, in studying final states involving several neutral particles, or in resolving the  $\Lambda^0/\Sigma^0$  ambiguity one again comes up against the problem that the gamma-rays produced in the experiment do not convert inside the chamber. To overcome this problem, bubble chambers containing heavy liquids of short radiation length, e.g. xenon of only 3 cm radiation length, have been developed. In these cases, however, problems such as a large number of background interactions, limitation of measuring precision due to Coulomb scattering and the most important of all, losing the advantage of having free proton (hydrogen) and almost free neutron (deuterium) as a target, limits the use of these chambers.

It seems then it would be very useful if the high gamma efficiency of the heavy liquid chambers could be combined with the advantage of the hydrogen/deuterium bubble chamber which provides free protons or quasi free neutrons as target. Therefore attempts have been made to put a hydrogen target inside a heavy liquid chamber. In some early

ones (refs. 1.15 and 1.16) the technique failed as no tracks could be photographed in the hydrogen. In 1964 Goldhaber (ref. 1.17) proposed the use of a neon-hydrogen mixture as a heavy liquid filling for cryogenic bubble chambers. Streett and Jones (ref. 1.18) made a detailed study of phase separation conditions for neon-hydrogen mixture and their results supported Goldhaber's idea. In 1966 Leutz (ref. 1.19) suggested that it was possible to make the hydrogen in the target and the mixture in the chamber simultaneously sensitive. The idea of track sensitive target was then generated and the CERN-DESY collaboration (ref. 1.20) in 1966 successfully operated a flexible mylar container for a track sensitive hydrogen target inside a neon-hydrogen chamber. Following this success the Rutherford-CERN collaboration adopted the idea and committed itself to a four year program using the 1.5 metre British national hydrogen bubble chamber (B.N.H.B.C.). The first run was made in November 1971 in a  $4 \frac{\text{GeV}}{c} \pi^+$  beam and was followed by a short run of  $\bar{p}$  interactions at rest. Finally an experiment with low energy and stopping kaons in hydrogen was made. This exposure is the subject of this thesis.

### 1.5 Outline of the thesis

In Chapter 2 the basic bubble chamber and track sensitive target are described. The limitation and the precision of T.S.T. is studied and a brief description of the beam-line is given. The essential features of the chain of processes are described in Chapter 3, together with a brief discussion on the accuracy of the measuring system. In Chapter 4 some preliminary results from Durham data is shown together with the statistics provided by the Durham group. The correction applied to  $\Lambda^0$  and  $\bar{K}^0$  events for obtaining an unbiased sample of events are described in Chapter 5, followed by the determination of absolute

cross-sections for  $\Lambda^0$  and  $\bar{K}^0$  channels. In Chapter 6 an analysis based on the missing mass squared to  $\Lambda^0$  is done to obtain Legendre expansion coefficients for angular distributions and polarisations for  $\Lambda^0\pi^0$  and  $\Sigma^0\pi^0$  channels. This is followed by the study of fitted  $\Lambda^0\pi^0$  and  $\Sigma^0\pi^0$  channels associated with one gamma-ray, the results of which are compared with those from the earlier analysis in this chapter. Finally the general conclusions are given in Chapter 7.

## CHAPTER 2

### EXPERIMENTAL DETAILS (I)

#### 2.1 The British National Hydrogen Bubble Chamber

The B.N.H.B.C. (ref. 2.1) was filled with neon-hydrogen mixture at a temperature of 29.8 K. The mixture contained about 78 mole percent of neon (radiation length  $\sim 40$  cm) to convert gamma rays into electron-positron pairs. Its internal volume was 150 cm x 50 cm x 45 cm. The windows of the chamber were 15.5 cm thick and their inner faces were 45 cm apart. Three cameras, 139 cm away from the chamber, having their parallel axes on an equilateral triangle of height 48 cm, photographed the chamber. The total volume of the chamber seen by all three cameras at once was about 180 litres and the volume seen by any pair of cameras was about 230 litres. The B.N.H.B.C. with surrounding magnet is shown in Fig. 2.1.

#### 2.2 Description of Track Sensitive Target (T.S.T.)

The track sensitive target filled with liquid hydrogen at a temperature of 29.5 K was chosen as a vertical slice through the centre of the 1.5 metre B.N.H.B.C. The thickness of hydrogen in T.S.T. was 7.5 cm. Fig. 2.2 shows a schematic diagram of T.S.T. The operating temperature and pressure (76 P.S.I.) of the chamber were chosen to make the hydrogen in the target volume and the mixture in the chamber simultaneously track sensitive. The side walls of the target were of  $\sim 10$  mm thick perspex which were essentially transparent to hadrons, gamma rays and visible light. They were also flexible enough to transmit the pressure variations from the neon-hydrogen mixture to the hydrogen in the target. With the expansion of the neon-hydrogen mixture, the flexing

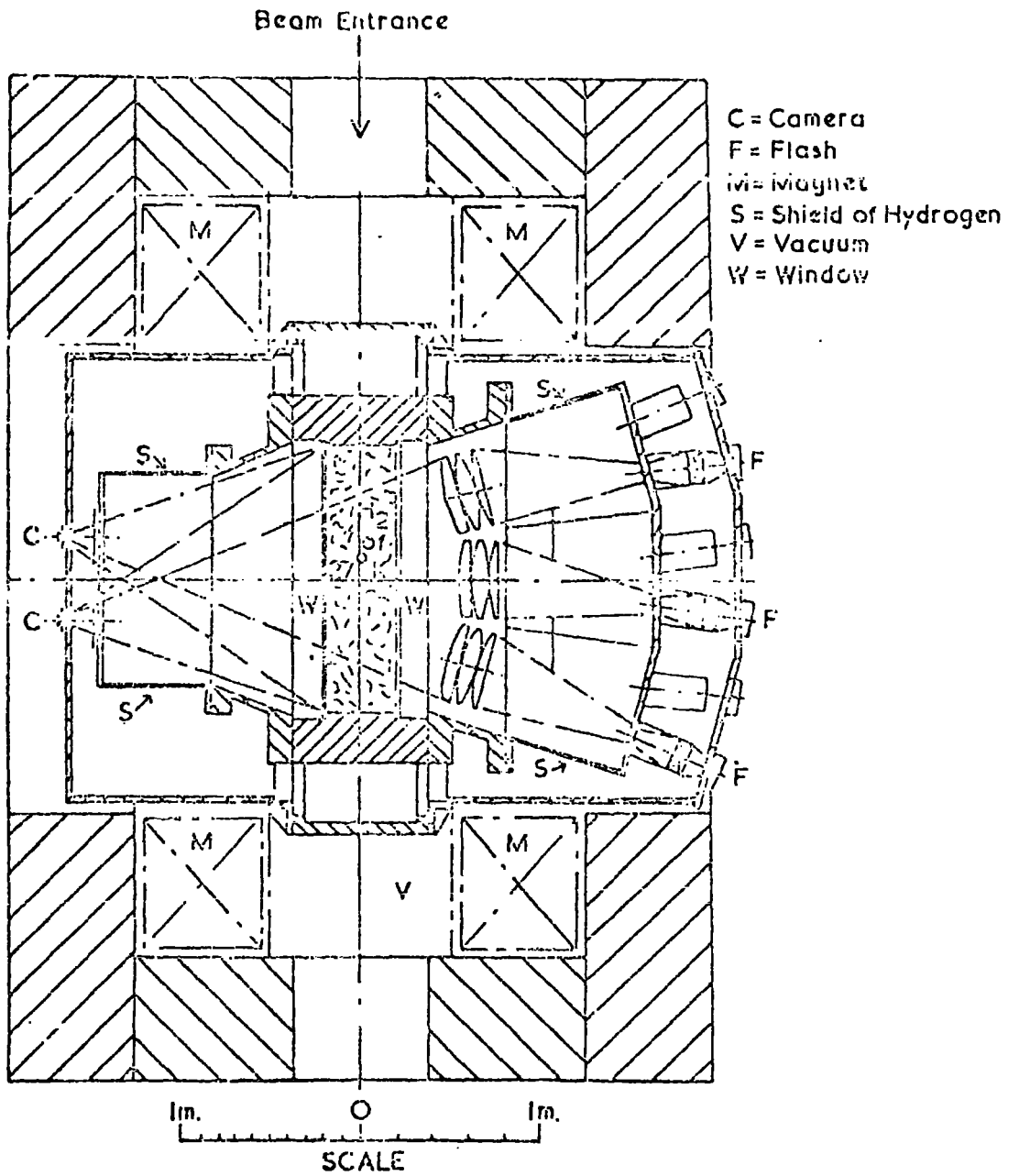


FIG. 2-1 PLAN VIEW OF B.N.H.B.C. SHOWING OPTICAL SYSTEM AND MAGNET



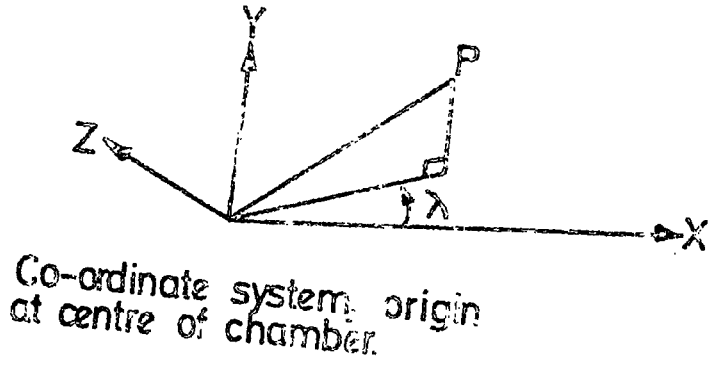
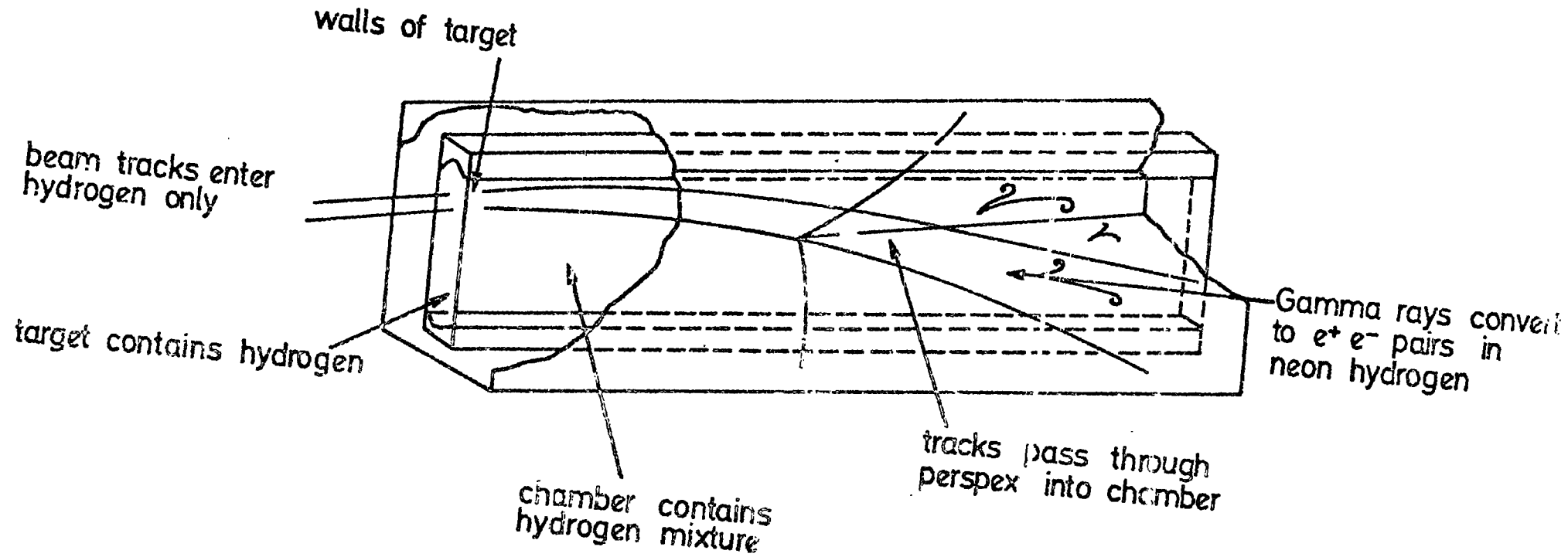


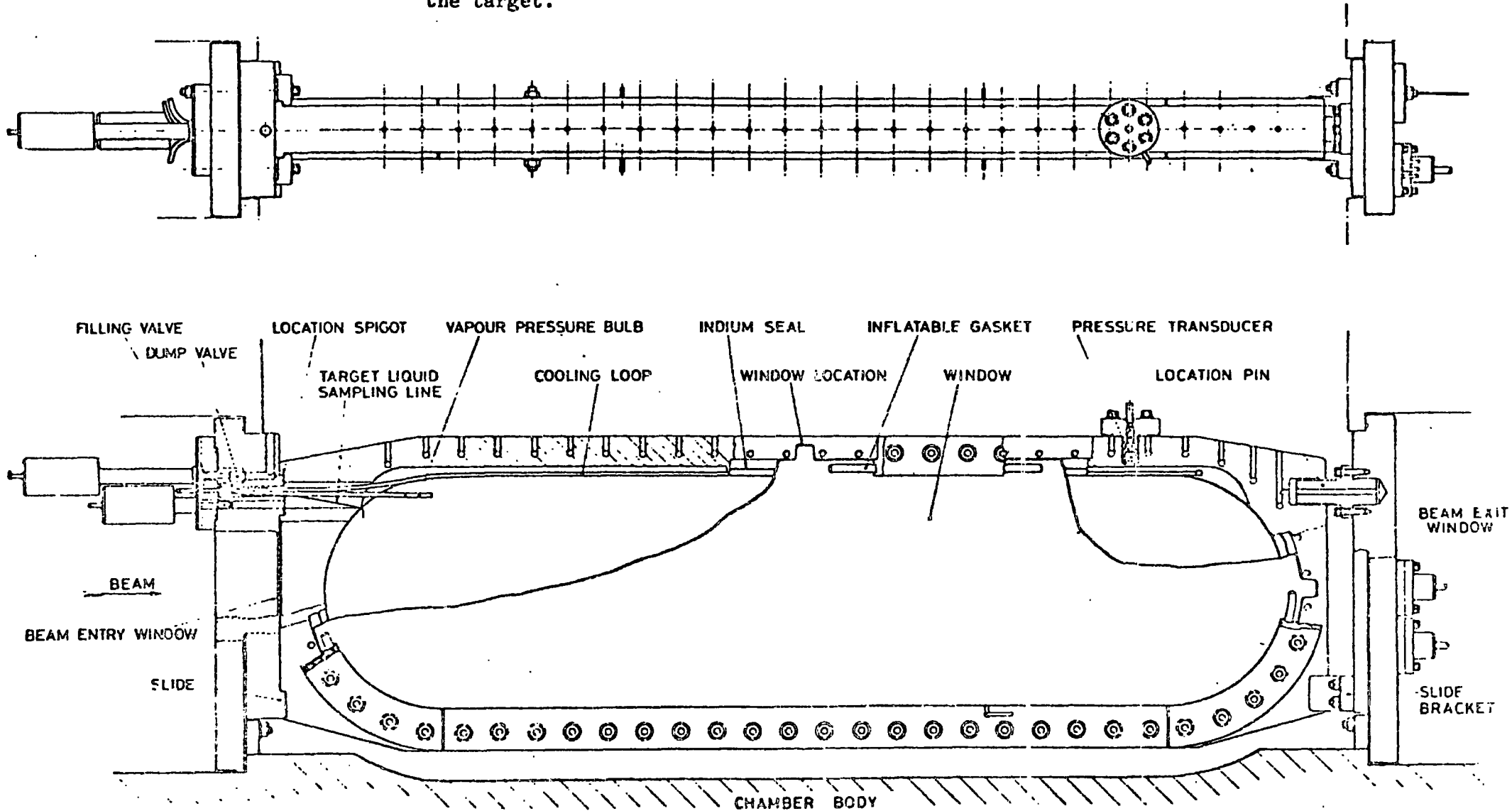
FIG.2.2 SCHEMATIC DIAGRAM OF TRACK SENSITIVE TARGET

of the perspex walls leads to a drop in the hydrostatic pressure inside the T.S.T. and hence it becomes sensitive to bubble formation. The movement of the perspex walls was less than 1 mm at each expansion and this led to a negligible contribution to the optical distortion of the chamber. The beam was injected into the hydrogen and since the T.S.T. was extended to the full length of the chamber, all primary interactions occurred on protons. The surrounding neon-hydrogen mixture presented a large solid angle for the detection of gamma rays emerging from primary and secondary interactions in the target. Two different types of target chamber were used in the exposure. The first one consisted of two flexible perspex windows parallel to the main chamber windows and were sealed to a steel frame by pressing them against indium wires. The frame itself was firmly connected to the bubble chamber body. The internal dimensions of this target were 135 cm x 33.5 cm x 7.5 cm. Figure 2.3 shows the metal framed target and in Figure 2.4 a typical picture from this target is shown. The obvious disadvantage of this target was that the frame which was neither transparent to gamma rays, nor to light, had obscured a significant volume of the bubble chamber and thus limited the gamma detection efficiency. The second target which was completely constructed of plexiglass seemed to overcome the problem of obscured volume. In Figure 2.5 a typical picture from this target is shown. The advantages of this target over the composite one were as follows:-

(a) Since there was a region of neon-hydrogen available above and below the target, its gamma detection efficiency was significantly improved.

(b) Unlike the metal framed target in which the frame had overshadowed the volume, in all perspex target all the chamber volume was visible and there was no shadowing effect. Details of the construction of the targets can be found in references (2.2) and (2.3) respectively.

Fig. 2.3: The Composite target section. The beam enters directly into the hydrogen. The magnetic field produces a curvature in the plane of the target.



TRACK SENSITIVE TARGET FOR 1.5 METRE CHAMBER



FIG. 2. A TYPICAL PICTURE FROM THE METE. FRAMED TARGET



FIG. 2.5 A TYPICAL PICTURE FROM THE ALL PERSEPLEX TARGET

### 2.3 The Exposure

The 1.5 metre B.N.H.B.C. with track sensitive target was exposed to a flux of negative Kaons (from the K 19 beam) from the proton synchrotron, NIMROD, at Rutherford Laboratory. The exposure took place in two runs with different target arrangements in August and November 1973. The author took part in the second exposure only. Approximately  $4.3 \times 10^5$  pictures were taken in the first run at five momenta between 0 - 445 MeV/c using the metal framed target and in the second run some  $4.7 \times 10^4$  pictures were obtained at 14 momenta between 240 - 580 MeV/c using the all perspex target. The films were then distributed among groups from University College London, Birmingham, Université Libre de Bruxelles and Durham (later in October 1975 a group from Warsaw University joined the collaboration). The work presented in this thesis is based only on Birmingham and Durham data from metal framed target.

### 2.4 The Beam

The K 19 beam was produced by interaction of the extracted proton beam from NIMROD with a copper target. The beam was a two stage electrostatically separated beam, a diagram of which is shown in Figure 2.6. Optically the beam could be divided into three independent stages by the locations of the two sets of intermediate collimators. Stage one provided both a well-defined momentum in the horizontal plane and an achromatic image of the target at the vertical plane. Particles produced in the target were focussed into horizontal collimator CH2 which had a fixed aperture by quadrupoles Q208 and Q216. The bending magnet M119 dispersed different momentum components of the particles at CH2 so that this collimator could select the desired momentum bite. The vertical collimator CV2 with a variable aperture at which an image of the target was produced served also as the first mass slit in the line. The second

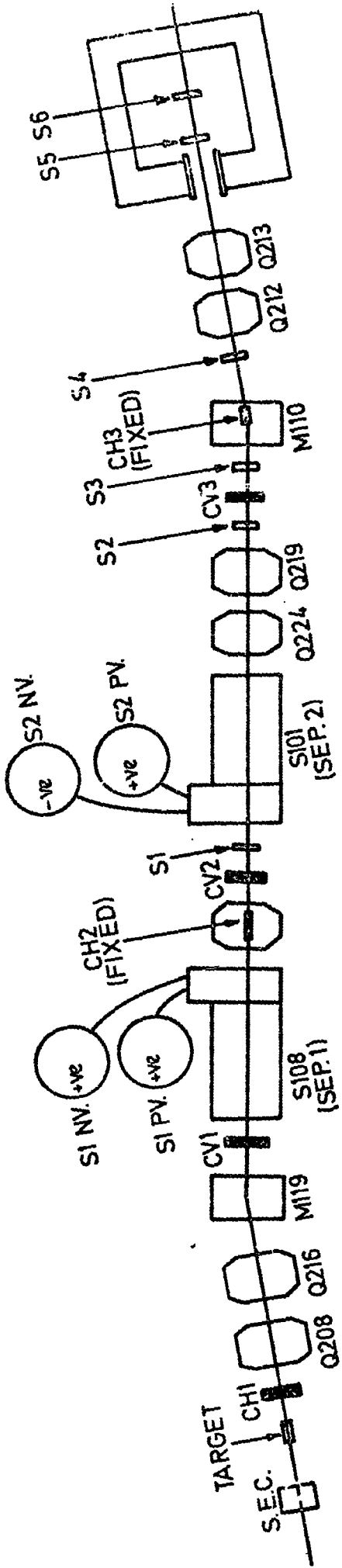


FIG.12-6) K19 BEAM LINE

stage which in fact began in the horizontal plane before the first stage had ended in the vertical plane contained the two electrostatic separators S108 and S101, by which unwanted particles were removed. Quadrupoles Q224 and Q2 19 refocussed the beam at CV3 and the bending magnet M110 gave a better momentum definition at CH3. Thus at the end of this stage an achromatic image of the target was provided in both planes. In the third stage of the beam line, the particles from CH3 and CV3 were transferred to the T.S.T. bubble chamber.

In order to enter the chamber volume horizontally, the beam had to be transported in the region of the bubble chamber magnet with relatively high momentum to avoid excessive curvature in the magnetic field. It was therefore reduced from the transport momentum ( $\sim 700 \text{ MeV}/c$ ) at the time of entering the hydrogen chamber by various thicknesses of an aluminium degrader to momentum in the region  $0-600 \text{ MeV}/c$ . The thickness of the degrader was chosen so that the energy of the beam particles were lowered to that desired in the experiment. In Table 2.1, the data taken in K19 beam are summarised.

There are disadvantages associated with the degrader which can be described as follows:-

- (a) The beam contamination was increased from 5% before entering the degrader to about 25% at the entrance of fiducial volume.
- (b) The beam particles were dispersed by the degrader and since the target was rather narrow, many of these beam particles left the T.S.T. into neon-hydrogen mixture with quite short track lengths.

## 2.5 Contamination of the Beam

The beam contamination before the degrader was mainly due to muons coming from decays in flight in the last separation stage. Moreover, the beam particles passing CV3 which acted as the second mass slit



Table 2.1: K19 DATA TAKING SUMMARY

This experiment was divided into Blocks of film with differing external beam momentum, degrader thickness and target type.

Block No.	Roll Nos.	Thousands of frames	Approx. $K^-$ per frame	Approx. entry momen. MeV/c	Approx. exit momen. MeV/c	Degrader thickness cms. AL	Target frame
1	1-105	229	5	260	0	30	metal
2	106-126	54	8.4	315	235	30	"
3	127-147	45	10.1	370	320	30	"
4	148-168	54	12.3	405	370	30	"
5	169-188	51	8.8	445	410	30	"
6	190-210	52	8.7	320	240	27	perspex
7	211-220	26	7.9	300	190	27	"
8	221-240	51	11.6	370	320	27	"
9	241-250	26	12.2	405	360	27	"
10	251-260	25	10.0	420	380	18	"
11	261-277	44	13.4	450	410	18	"
12	278-286	22	14.2	475	435	18	"
13	287-292	16	17.3	495	455	18	"
14	293-304	28	12.6	505	465	9	"
15	305-314	25	16.6	530	490	9	"
16	315-335	49	20.0	550	510	9	"
17	336-355	49	12.6	560	525	0	"
18	356-365	25	25.7	500	545	0	"
19	366-379	35	15.2	510	475	18	"

could decay and therefore contributed to the beam contamination at the chamber.

Because of the low momenta involved in the experiment, the contamination from negative pions, muons and electrons can be clearly recognized from kaons by eye because of the large difference between their ionisation and that of the kaons. In an experimental survey of the film, the contamination was measured and was found on average to be about 25% of the beam particles.

## 2.6 Limitation of the T.S.T. Chamber

As indicated in 2.4, the shallow depth of the T.S.T. ( $\sim 8$  cm) combined with the diffusion of the beam particles by the degrader, leads to rather short potential path lengths of both primary and secondary particles. For example in the present experiment the  $\tau^0$ -meson decays in the T.S.T. had an average potential path length of about 50 cm for the primaries and about 14 cm for the secondaries. Because of these short lengths, it is necessary to examine what limitations these impose on the general measuring precision of the experiment and this is considered in the next section. Other limitations of the T.S.T. chamber are as follows:

(1) The T.S.T. is bounded by  $\sim 1$  cm thick perspex windows which separates the hydrogen liquid from the neon-hydrogen mixture. A comparison of their approximate stopping powers and mean free paths for strong interaction are shown in Table 2.2. It is clear that the perspex windows present a considerable stopping power to the charged particles and considerable cross-section for nuclear interaction. This is important from two points of view. Firstly there will be one class of interaction which is ambiguous at the scanning stage. This class will look like zero prong absorption of the primary kaons with associated  $V^0$  and, perhaps, gamma

rays. It is expected from the figures in Table 2.2 that approximately one half of the zero prong interactions with  $V^0$  will have occurred in the perspex walls. Secondly if neon diffuses through the seal into the T.S.T., it will be apparent by a change in stopping power and by strong interaction in the neon. The former may be detected, for example, by the variation of range of  $\mu$ -mesons from  $\pi\mu e$  decay. The latter will be manifest by interactions characterized by short black tracks.

(2) The shallow depth of T.S.T. will introduce geometric problems associated with probabilities of detection. At the momenta of this experiment the decay length of the  $\Lambda^0$  will be  $\sim 3$  cm. In a conventional bubble chamber the detection of these would only be limited by visibility considerations (e.g. there is less chance of detecting a steeply dipping  $\Lambda^0$ ). The thickness of the T.S.T. chamber is about 2-3 decay lengths and with the widely dispersed primary beam this means that many  $\Lambda^0$ s will escape from the hydrogen of the T.S.T. where there is precision of measurement, into the neon. This and similar effects will have to be handled by weighting factors.

Table 2.2

Z	Material	Density gm/cm <sup>3</sup>	Stopping power in Equi. cm of H <sub>2</sub>	Mean free path for Strong int. cm	Thickness cm
1	H <sub>2</sub>	.063	1	$\sim 450$	$\sim 8$
3.6	plexiglas	1.2	$\sim 9$	$\sim 50$	$\sim 2$
$\sim 8$	Ne/H <sub>2</sub>	.635	4.5	$\sim 110$	$\sim 37$

Comparison of stopping powers and mean free path for strong interaction for different regions in T.S.T. Chamber.

## 2.7 Precision of the T.S.T. Chamber

The T.S.T. chamber in this present experiment has been used to examine the interactions of relatively low momentum particles. So apart from the limitation that is imposed in measuring accuracy from the reduced track length (because of the shallow depth of the T.S.T.), there is also limitation imposed by Coulomb scattering. In this section the relative importance of these limitations is considered, together with a consideration of the usefulness of making measurements in the neon hydrogen parts of the chamber (which almost certainly is Coulomb dominated). In the following discussion the units will be:

- (1) Length in cm
- (2) Momentum in MeV/c
- (3) Magnetic field in K gauss
- (4) Angles in radians

The measuring inaccuracy of momentum  $P$  on a track of length  $L$  is

$$\left(\frac{\Delta P}{P}\right)_{\text{meas}} \sim \frac{7.8 f_0 P}{0.3 H L^2} \quad (2.1)$$

where  $f_0$  is the accuracy of the measuring system transformed to chamber space, and  $H$  is the magnetic field. The factor 7.8 results from combining three measured views for the 3-dimensional reconstruction of the event.

Regarding Coulomb scattering as a "noise", then the limitation imposed by this is:

$$\left(\frac{\Delta P}{P}\right)_{\text{Coul.}} \sim \frac{45}{\beta H \sqrt{X_0} L} \quad (2.2)$$

where  $\beta$  is the velocity of the particle and the multiple Coulomb scattering constant for hydrogen is 45. This expression does not imply that Coulomb scattering itself decreases as  $\frac{1}{\sqrt{L}}$ . In fact the sagitta due to Coulomb scattering increases as  $L^{3/2}$  but the sagitta due to the magnetic field increases as  $L^2$  and so relative to magnetic deflection the Coulomb scattering falls as  $\frac{1}{\sqrt{L}}$ . Really the Coulomb scattering should be compared with  $f_0$ , the measuring precision. Below a critical length,  $f_0$  is larger than the Coulomb sagitta (which is equivalent to a  $f_0$ ) and so measuring error dominates. Above this length Coulomb error dominates. The track length where the measuring inaccuracy is just equal to the Coulomb inaccuracy is given by :

$$\left(\frac{\Delta P}{P}\right)_{\text{meas.}} \sim \frac{7.8 f_0 P}{0.3 H L^2} \sim \frac{45}{\beta H \sqrt{\chi_0 L}} \sim \left(\frac{\Delta P}{P}\right)_{\text{Coul.}}$$

$$L \sim 0.6937 (P \beta f_0 \sqrt{\chi_0})^{2/3}$$

In the present experiment  $f_0 \sim 0.01$  cm, the radiation length for hydrogen  $\chi_0 \sim 990$  cm and so:

$$L \sim 0.315 (P\beta)^{2/3} \text{ cm} \tag{2.3}$$

This critical length above which Coulomb error determines the accuracy is shown in Table 2.3 for primary kaons in the momentum range of this experiment.

Table 2.3

$P_k \left(\frac{\text{MeV}}{c}\right)$	$\beta_k$	L in H <sub>2</sub> (cm)
200	0.375	5.60
400	0.629	12.55
600	0.772	18.86

The critical length for different momenta at which Coulomb and measuring errors are just identical.

For the secondary particles of the kaon interactions, the momenta are in a similar range and although the  $\beta$  values will be different the  $L$  values will be typified by those in Table 2.3. Consequently in the lower momentum range of the experiment errors are expected to be dominated by Coulomb scattering whereas in the upper momentum range they will be dominated by measuring accuracy.

The above considerations are true for hydrogen, however in the neon-hydrogen part of the chamber, where the radiation length is reduced from  $\sim 990$  cm for hydrogen to about 40 cm for the mixture, then the critical lengths in Table 2.3 should all be reduced by a factor of  $\left(\frac{990}{40}\right)^{1/3}$  which is  $\sim 2.9$ . Consequently even with the longer potential path lengths in the deeper neon-hydrogen chamber the measurements will be limited by Coulomb scattering. It is of interest to decide whether measurements of momentum are worthwhile in the neon. For example if a track crossing from the T.S.T. to the neon is measured in both parts and if the measurement is limited by Coulomb scattering, then the ratio of the inaccuracies will be

$$R = \left(\frac{\Delta P}{P}\right)_{\text{Ne/H}_2}^{\text{Coul.}} \bigg/ \left(\frac{\Delta P}{P}\right)_{\text{H}_2}^{\text{Coul.}} \sim \left(\frac{A_{\text{Ne/H}_2}}{A_{\text{H}_2}} \cdot \frac{L_{\text{H}_2}}{L_{\text{Ne/H}_2}}\right)^{1/2}$$

where

$$A = 4\pi N (Ze^2/P\beta c)^2 \text{ cm}^{-1}$$

For hydrogen  $N_{\text{H}_2} = 3.4 \times 10^{22}$  atoms/cc and for the mixture ( $Z \sim 8$ )  $N_{\text{Ne/H}_2} \sim 2.9 \times 10^{22}$  atoms/cc. Therefore the ratio  $R$  is,

$$R \sim 7.4 (L_{\text{H}}/L_{\text{Ne/H}_2})^{1/2} \quad (2.4)$$

(For detail see references 2.4 and 2.5). To improve the accuracy of the neon measurement to that of the hydrogen, the track length measured in neon would need to be  $\sim (7.4)^2$  times longer than that in hydrogen,

i.e.  $\sim 55$  times longer. This number should be compared to the ratio of potential path lengths in the T.S.T. and in the neon-hydrogen mixture. A typical value of this can be obtained from the ratio of the thickness of the neon mixture to that of the T.S.T. This is about  $\sim 5$  and so even if the full available lengths are measured the inaccuracy of the neon measurement will be on average three times worse than in hydrogen. Obviously for a track which is short in hydrogen but considerably long in neon, then there is every advantage to be gained by measuring in neon. Moreover from the table where the stopping powers are displayed, then every baryon that is produced in kaon interactions in this experiment that penetrates to the neon, will be stopped in the neon. The accurate range measurement will lead to an accurate momentum determination.

The Coulomb scattering as well as measuring inaccuracy also contribute to the estimate of the errors on the azimuthal angle,  $\phi$ , and dip angle,  $\lambda$ , defined as the angle of the track with respect to the plane normal to the direction of the magnetic field. In a similar way to that above, one can find a critical length in hydrogen for the incident track at which the contributions arising from both Coulomb scattering and measuring error are identical. These critical lengths are as follows:

$$L_{\phi} \sim 0.467 (P\beta)^{\frac{2}{3}} \text{ cm}$$

and

$$L_{\lambda} \sim 0.584 (P\beta)^{\frac{2}{3}} \text{ cm} \tag{2.5}$$

Comparing the values obtained from the above equations with those quoted in Table 2.3 shows that as far as the angles are concerned the measuring error usually dominates. For example, at 400 MeV/c,  $L_{\phi} \sim 18.61$  cm and  $L_{\lambda} \sim 23.27$  cm.

For the neon-hydrogen mixture where the critical lengths are reduced by a factor of  $\sim 3$ , the angle errors will be dominated by Coulomb

scattering and since the error due to Coulomb is directly proportional to the length of the track measured, it is always worthwhile to measure tracks in the neon-hydrogen mixture.

For strong interactions, the number of continuations into neon-hydrogen mixture, experimentally, is  $\sim 25\%$ . Since this is relatively small, there is little loss of measuring time in measuring in the neon-hydrogen mixture. Then the general conclusion is that the continuation of tracks into the neon should be measured.



CHAPTER 3

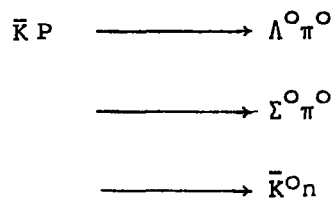
EXPERIMENTAL DETAILS (II)

Before the data analysis of a bubble chamber experiment is reached, the experiment must pass through a chain of processes. These begin with the exposure, which has already been described in Chapter 1, and continue with the scanning, measuring, reconstruction and kinematic analysis of events and lead finally to the production of a data summary tape (DST). A schematic diagram of the data flow is shown in Fig. 3.1 and the essential features of the chain of processes are described below.

3.1 Scanning of events

Events were scanned in a fiducial volume defined by an area of grid squares in view 2. This consisted of 6 columns and 13 rows as shown in Fig. 3.2 and it was chosen so that events within that volume could be seen clearly. An event was accepted if it was in the fiducial volume, provided that the beam track had entered the chamber through the whole length of the degrader. However, gamma conversions and  $V^0$ -decays were not restricted to this fiducial volume and were sought everywhere on the frame in all views. The  $V^0$ -decays were recorded only if they had decayed in the hydrogen of the chamber whereas all gamma conversions were recorded. Events were scanned for in the following topologies:

(a) Zero prong events with a neutral  $V^0$  These events include physical channels such as



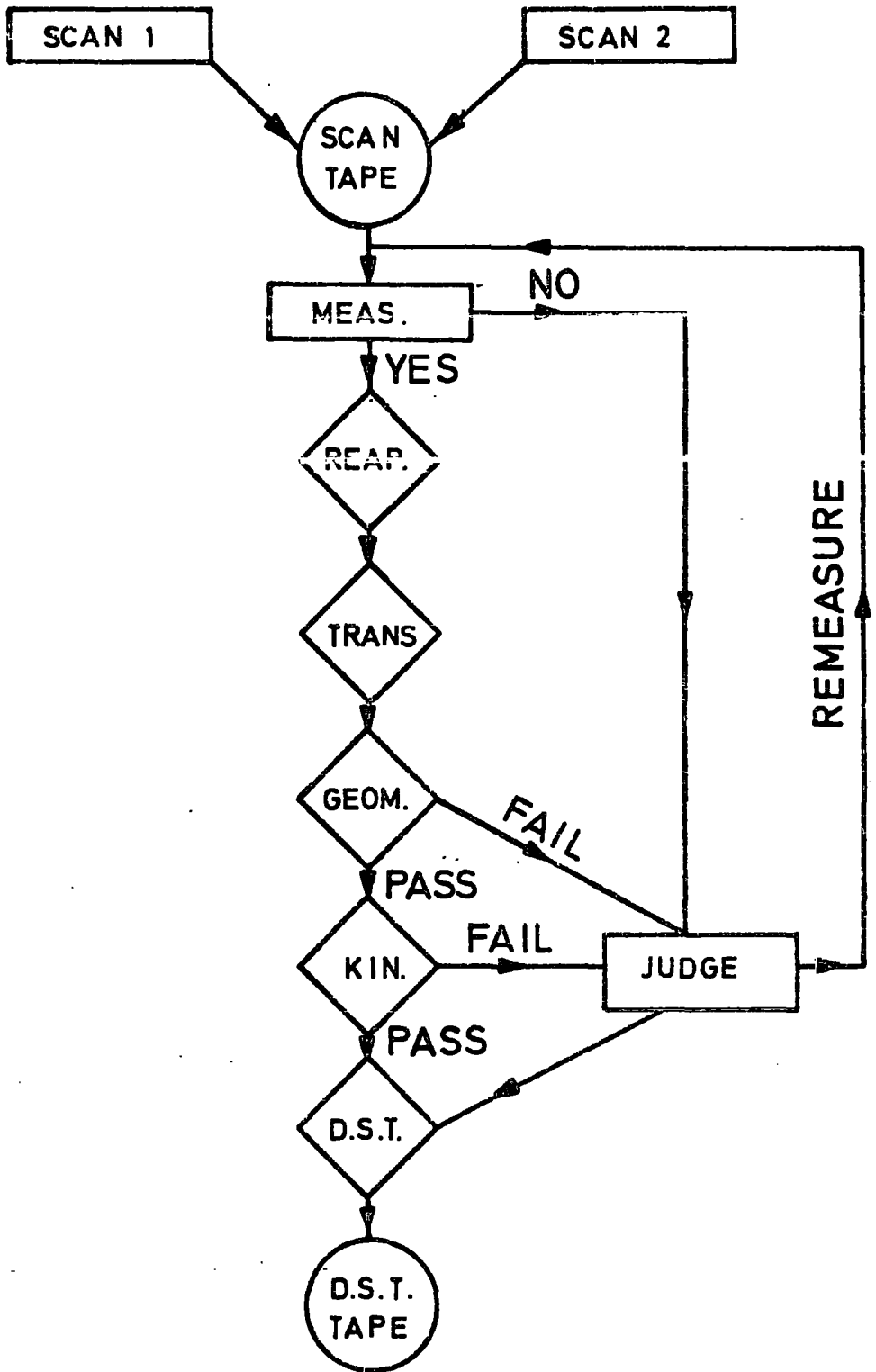


FIG. 3.1 SCHEMATIC FLOW DIAGRAM FOR EVENTS

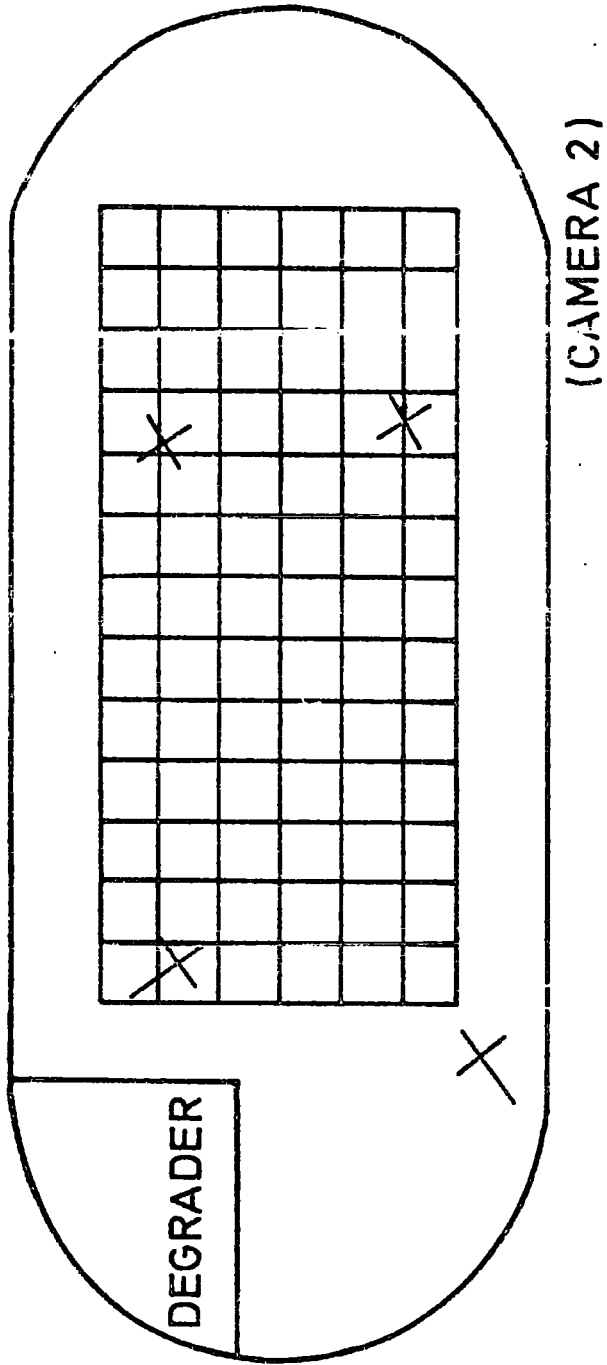
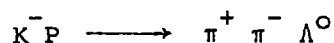


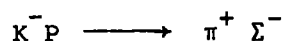
FIG. 3.2 SCANNING FIDUCIAL VOLUME

and appear on the frame as a terminating beam track with no charged secondaries other than those in the associated  $V^0$ . The  $V^0$ -particle, which was the decay of a  $\Lambda^0$  or  $\bar{K}^0$  into two charged particles, was required to be within two gridwidths ( $\sim 20$  cm) from the primary vertex. This limit was introduced to restrict the area for  $V^0$  scanning to make it more accurate. It is justified since, for the dilated lifetimes of these particles, two gridwidths would correspond to the order of 10 lifetimes. When an event was found, the frame was searched for associated gamma rays in all views in both the hydrogen and neon-hydrogen mixture.

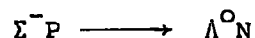
(b) Two-prong events with a neutral  $V^0$  These events were treated in exactly the same way as class (a) events. They consist of two main groups:



where the  $V^0$  is produced at the primary vertex and



followed by



where  $\Lambda^0$  is associated with the secondary vertex.

(c) Two-prong events The following classes of events were scanned for and recorded:

(i) Elastic Scattering  $K^-P \longrightarrow K^-P$  These were identified with the positive track going forward from the production vertex and where both secondaries have ionizations almost as heavy as the incident beam track. These events were unambiguously recognized when the scatter  $K^-$  had produced a secondary interaction. All events preceded by elastic scatterings were also recorded.

(ii) Sigma Production These were events with an obvious decay in either of the positive or negative secondaries. When an event was recognized as the production and decay of a positive sigma to proton, the frame was then searched for gamma rays from the associated  $\pi^0$  decay.

(iii) Negative Sigma Interaction These were events in which the produced negative sigma either interacted in hydrogen and the  $\Lambda^0$  produced was not seen or stopped in perspex.

(iv) Other two prongs Events which could not be classified in one of the above groups were placed into this category. Topologies found in this group included  $\pi^+\pi^-$  events which are due to sigma production in which the sigma had decayed very close to the primary vertex and  $\pi^-p$  events which are due both to  $\Lambda^0$  production with  $\Lambda^0$  decaying very close to the primary vertex and to the production and close decay by the proton mode of the positive sigma.

(d) Three-prong Events All three-prong events were scanned for and recorded under the following event types:

(i) tau-decays There is a small contamination in this group from  $K^-$  - decay to pion accompanied by a Dalitz pair. They were readily identified and excluded by measurement.

(ii) Neon events These were events in which the length of the positive track was less than 1 cm and the track was heavily ionising, that is it could be a proton. These events were produced from the collision of a beam particle on an isolated neon atom in the hydrogen chamber.

(e) Pi-mu-electron decays The film was scanned for any positive pion track decaying into muon followed by an electron so that the muon range

could be used later to monitor the densities of hydrogen and neon-hydrogen mixtures and also to monitor the range-energy relationship at low energy.

In order to evaluate the scanning efficiency, all film used in this work was double-scanned except two-prong events for which double-scanning was carried out on a subset of film only. About 10% of the film was scanned for a third time to check the scanning efficiencies evaluated on the basis of the double-scan. The scan information was punched into computer cards and stored on a magnetic tape (scan tape) to be used later for the following purposes:

1. Production of a measuring list
2. Evaluation of scanning efficiencies
3. Producing information for the various event categories.

### 3.2 Measuring of Events

All events were measured using six conventional measuring machines digitized with Moire fringe systems, on-line to an IBM 1130 computer. Any point could be measured on these machines to an accuracy of 1 fringe ( $\sim 25 \mu\text{m}$ ) in the image plane. Unless the event was only seen in two views, all events were measured on three views (an event could be reconstructed in three dimensional chamber space if it had been measured on any of two views, but measuring three views guaranteed at least two good views). For every event the production vertex, four fiducial crosses (one on the light-side TST window, one on the chamber's back window and two crosses on the inner surface of the camera-side main window. See Figure 3.2), and the beam track were measured. This was followed, depending on the event topology, by measuring decay vertex, tracks associated with decay vertex, tracks associated with production vertex,

vees and gamma conversions respectively in each view. If an event was preceded by an elastic scatter, the scatter vertex, incoming beam and proton track associated with the scatter vertex were measured before measuring the secondary vertex. For each track usually nine points were measured in each view if it was produced only in hydrogen and up to twenty points if the track had passed from hydrogen through the perspex wall into neon-hydrogen mixtures (split tracks). Short tracks could be accepted with at least five points. Split tracks were measured over their entire length, wherever possible, including the last point in hydrogen as well as the first point in neon-hydrogen mixtures. The last point inside hydrogen was doubled by the on-line programme so that the reconstruction programme could recognise the end of the track in hydrogen and its beginning in neon-hydrogen.

For neutral as well as very short tracks only two points were measured in each view. If a track was recognized as a stopping proton it was measured to its full length including its end point and for short stopping tracks only the end point was sufficient to be measured. VeEs and gamma conversions were measured in the same way as were tracks associated with the production vertex. Window gamma conversions in which the vertex had disappeared into perspex walls were also measured.

### 3.2.1 Accuracy of the Measuring System

Prior to this experiment the measuring system had been used largely for rough digitization of films which were subsequently accurately measured on the H.P.D. (Hough-Powell Device) of the Rutherford Laboratory. To handle the T.S.T. by manual measurements only, the accuracy of measurement had to be made high. To this end a series of checks were devised and used continually through the experiment.

(a) Check on Fiducial Measurements The on-line program was instructed to perform a test on four measured fiducial crosses for <sup>the</sup> following purposes:

(i) to identify and position the view correctly

(ii) to check for stretching of the film

(iii) to bring to notice any disturbance in the projection system.

In this test, the real distance between any two of the fiducials were calculated and compared with the corresponding expected distances for the view concerned. If the difference between the two corresponding values was in excess of  $\sim 0.5$  mm (maximum acceptable tolerance) the test failed and measurements were repeated after removing the cause of failure. In practice no stretching of the film was detected.

(b) Acceptable Tolerance on Track Measurements A two dimensional circle fit to the points measured along each track including the vertex was attempted. The fit was considered to be sufficiently good if the standard deviation did not exceed the maximum permitted tolerance given by

$$\text{TOL} = C_1 \left( 1 + \frac{C_2 L^3}{D^2} \right)^{1/2} \quad (3.1)$$

where  $C_1$  and  $C_2$  were set to 4 fringes and  $2 \times 10^{-2}$  (fringes)<sup>-1</sup> respectively for tracks in hydrogen and 4 and  $4 \times 10^{-2}$  for neon tracks (tracks in neon-hydrogen mixtures), L and D (in fringes) are the measured length and diameter of the fitted circle respectively. Here  $C_1$  is the expected error from the measuring system and  $C_2$  derives from Coulomb scattering so that the effective tolerance is increased at low momentum (see Appendix A).

The on-line system also rejected tracks which had turned through an angle greater than  $180^\circ$ . In this case a track was remeasured over a shorter length until it was accepted.

(c) Optical Calibration Although the random errors can be kept small by the fiducial and track checks described above, systematic errors from



distortions in the projection system remain. These distortions are measured by detailed calibration of the image plane of each of the three views.

To calibrate an image-plane digitizer (measuring table), that is to remove distortions due to projection system, fiducial crosses which had known positions on the film-plane were measured. The known and measured positions are related by polynomials of the form:

$$x' = a + bx + cy + Dx^2 + Ey^2 + Fxy + Gy^2x + Hxy^2 + Ix^3 + Jy^3$$

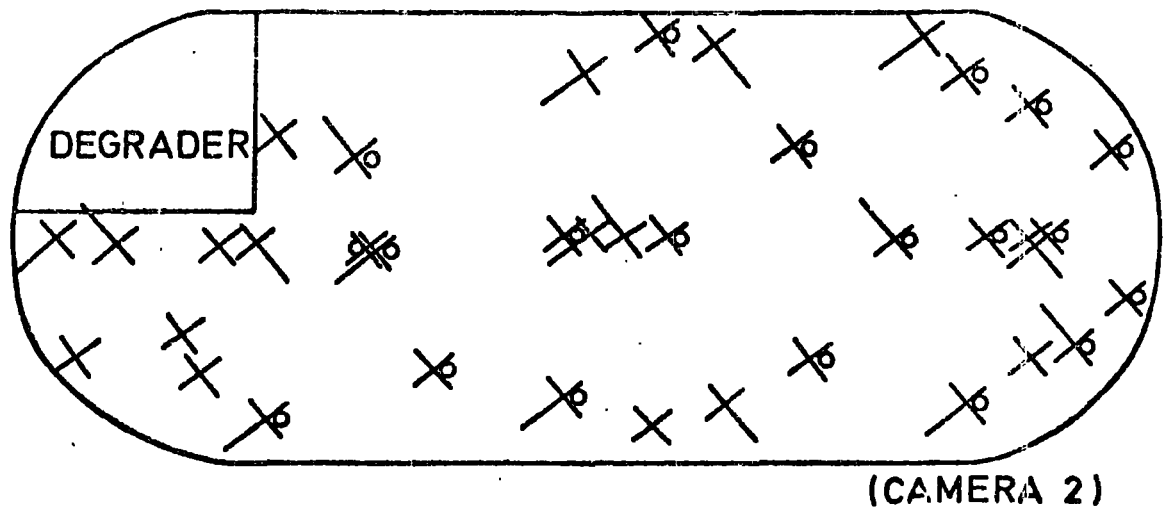
$$y' = a' + b'x + c'y + D'x^2 + E'y^2 + F'x^2y + G'y^2x + H'xy + I'x^3 + J'y^3$$

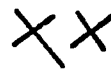



where  $(x',y')$  is the known position and  $(x,y)$  is the measured position of a cross and where  $a,a'$  etc. are coefficients to be determined.

By measuring 20 fiducial crosses on each view (Fig. 3.3), the coefficients in the polynomials were determined using a least square fitting regression programme. After fitting, substitution of the coefficients and measured positions yield  $X',Y'$  to within  $\sim 5 \mu\text{m}$  from the known positions in the film. Coefficients obtained from regression were then used to transform all measured film points into corresponding points on the ideal film plane.

In order to get an estimate of the size of optical distortion, the measured coordinates of some fiducials were compared with their known positions on the film. It was found that measured positions were  $\sim 1.7 \text{ mm}$  different from their known positions for the fiducials located in the extreme ends of the chamber and  $\sim .4 \text{ mm}$  for those close to the optic axes.

(d) Monitoring As a check on the quality of calibration, the difference between the measured and expected distances for any two of the four fiducial crosses measured in each view could be monitored. This difference is expected to peak around zero (Fig. 3.4a), if not (Fig. 3.4b)



- 
 FRONT GLASS / PERSPEX FIDUCIALS
- 
 REAR GLASS FIDUCIALS
- 
 REAR PERSPEX FIDUCIALS
- 
 MEASURED FIDUCIALS

**FIG 3.3 DIAGRAM OF THE FIDUCIAL CROSSES IN THE CHAMBER**

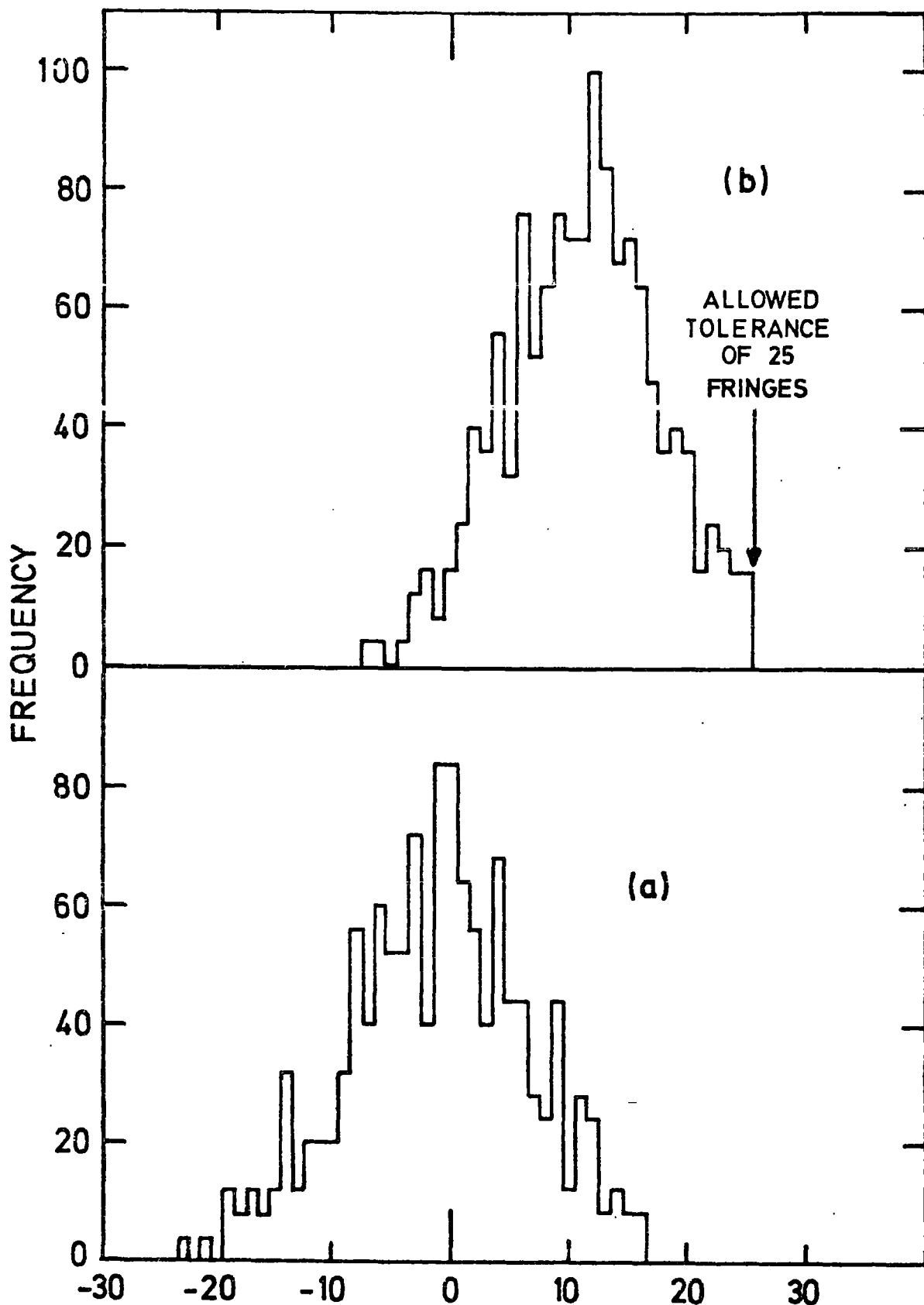


FIG. 3.4 DIFFERENCE BETWEEN MEASURED AND EXPECTED DISTANCES FOR 2 FIDUCIAL CROSSES ON VIEW 2 (FRINGES).

that particular view or views were recalibrated.

A further check introduced into the system was to project a view number, fixed in the film plane on to the image plane. Any mechanical movement of the projectors could be immediately recognized and corrected. By use of these checks, tolerances and monitoring the precision of the system was kept at a high level. The helix fit errors on vertices and fiducial crosses was typically  $8 \mu\text{m}$  (Fig. 3.5a) and on tracks about  $10 \mu\text{m}$  (Fig. 3.5b). Prior to the introduction of these checks, these were typically about  $30 \mu\text{m}$  on tracks. This good precision led to a pass rate in Geometry (see Section 3.5) of about 85%.

### 3.3 Processing of Events

A series of computer programmes have been developed to process the measured events. A brief description follows.

#### 3.3.1 REAP

The raw data coming from all the measuring tables are stored on a disk of an 1130 IBM computer. The disk is subsequently read via another IBM 1130 into the IBM 360/195 at the Rutherford Laboratory. The measurements are translated from the 1130 coding stored on 195 disk in a standard form by programme Reap.

#### 3.3.2 TRANS

The measurement of an event must be presented to the reconstruction programme in a standard format. For this purpose, the programme Trans was used to translate the output from Reap to an input for the geometry programme. In this transformation of the measured co-ordinates to the ideal film plane, labelling window gammas to be identified by the reconstruction programme, determining the sense of curvature of the tracks and adding a vertex at the end of possible stopping tracks were done. It is

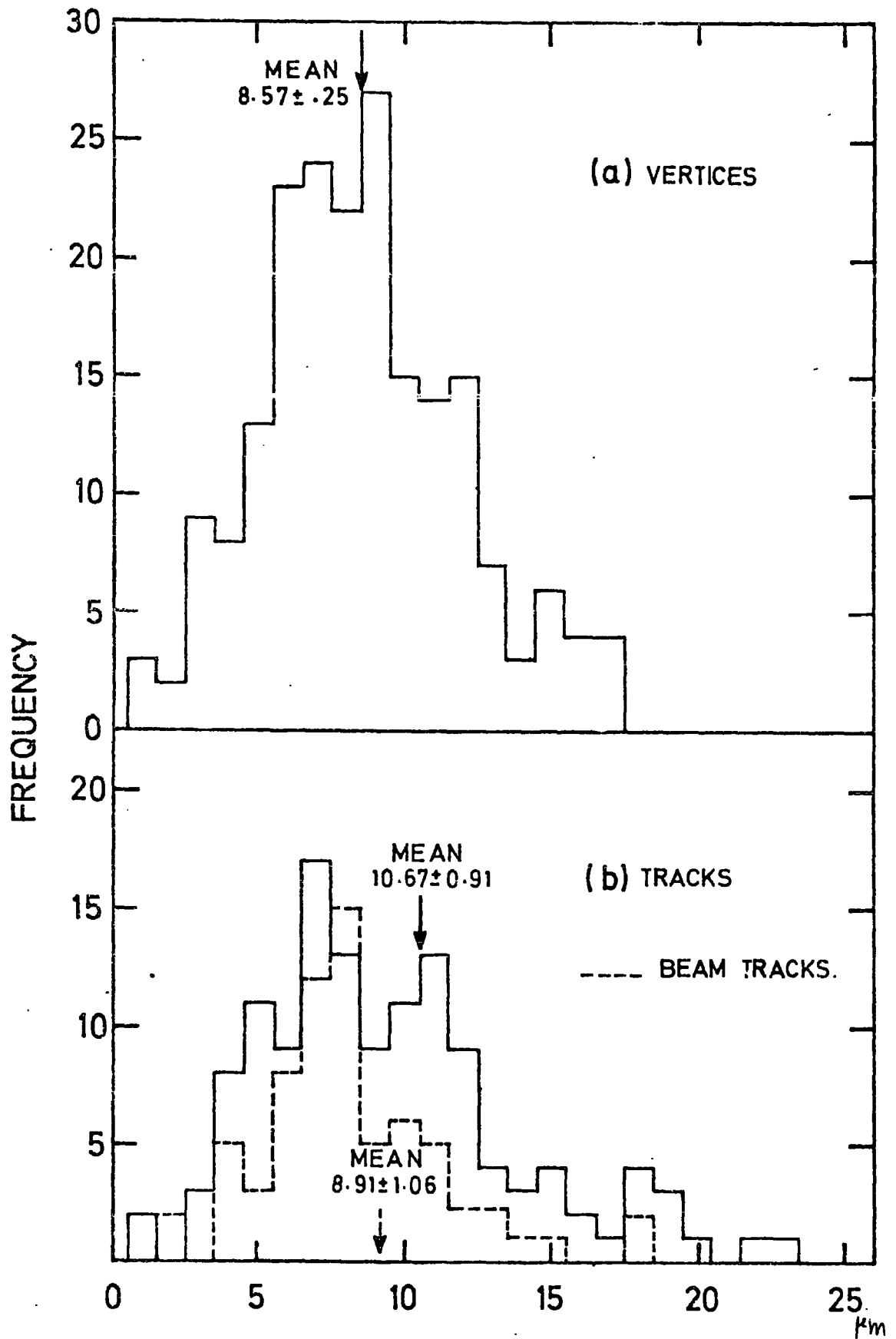


FIG.3.5 ERROR ON VERTICES AND TRACKS.

in this process of translation that the corrections are made for the distortions of the projection systems of the measuring machines.

### 3.3.3 Geometrical Reconstruction

The Rutherford Laboratory geometry programme, HGEOM, was used to reconstruct tracks in the 3-dimensional space of the chamber and to assign the geometry errors to them. The programme was originally written for processing events produced in a conventional bubble chamber (ref. 3.1) and was later modified by Dr. J.G.V. Guy at the Rutherford Laboratory to reconstruct tracks in the TST chamber and named BAGEOM. The modifications made in HGEOM consisted of those which are normal in heavy liquid bubble chambers and are specifically made to deal with electrons and gamma rays and those which allow for the track sensitive target. A brief description of the latter is given below.

In constructing vertices, BAGEOM first transforms all the measured points on the film to rays in the chamber liquid assuming that the chamber is filled with just one liquid. It then corrects the rays for the extra media traversed and the vertices are then reconstructed as corresponding points. During geometrical reconstruction of tracks, BAGEOM checks to see if any track has crossed the TST wall. If so, the track is divided in two parts at the double point which has already been included in the ray co-ordinates for the track (see Section 3.2). It divides the track up by creating a new track with co-ordinates from the second segment of the original track. At this stage a vertex is also generated at the end of the first part of the track. A mass dependent helix fit is then made to each segment of the track in hydrogen or neon-hydrogen using the appropriate constants for that medium (the two sections of a track must be reconstructed separately because firstly the errors are different on the

two sections of the track and secondly a track could have been scattered in the perspex wall, through a fairly large angle without being seen). From the parameters of the fitted helix, the momentum variables of the track with their correlated errors are calculated. These variables are  $\phi$ , the azimuthal angle,  $\tan \lambda$ , where  $\lambda$  is the dip angle and  $1/p$  where  $p$  is the momentum of the track and are all calculated at the centre of the track. Each split track has now two reconstructed segments with their own variables. BAGEOM then creates a new track out of these two parts with a set of mass dependent helices which are constrained by minimum  $\chi^2$ , to be the best fits to the mass dependent helices from the hydrogen and neon-hydrogen mixture. By swimming the variables at the centre of track in neon-hydrogen mixture to the centre of track in hydrogen a weighted average of the hydrogen and neon track variables can be made at the centre of track in hydrogen.

Tracks are checked by BAGEOM to see if they stop in the perspex walls of the T.S.T. If so, the momentum is obtained for the track assuming it has stopped at either side of the perspex and the momentum is then computed as the mean between these momenta. Subsequently this was found to create problems particularly with the proton of  $\Lambda^0$ -decay and this feature of BAGEOM was removed.

In reconstructing electron tracks, the energy loss due to Bremsstrahlung is taken into account using the formulae from the section on the Behr-Mittner method described in ref.3.1. BAGEOM then fits different helices with different energy loss per unit length to electron tracks and selects the best fit to make up the gamma rays. The momentum of gamma rays is taken from the sum of the electron momenta and the angles are taken from the production and conversion vertices. In the case of window gammas, BAGEOM tries to find a point where the electrons would

meet and takes that point as the gamma vertex. The information from geometrical reconstruction was output to be used in the next stage of the data processing.

### 3.3.4 Kinematic fitting

The reconstructed events were passed to the RL Kinematical fitting programme KINEMATICS (ref. 3.2) which tested each event against various hypotheses of particular mass assignments given for that event. Each hypothesis was specified by the scan topology of the event, masses for each track and a fit sequence which determined how the kinematical fitting should be carried out. A list of hypotheses attempted for each topology is given in Table 3.1. The final fit for an event should have satisfied the following 4-constraint equations describing the conservation of energy and momentum:

$$\Sigma P_x = \Sigma P_i \cos \lambda_i \cos \phi_i - P \cos \lambda \cos \phi = 0$$

$$\Sigma P_y = \Sigma P_i \cos \lambda_i \sin \phi_i - P \cos \lambda \sin \phi = 0$$

$$\Sigma P_z = \Sigma P_i \sin \lambda_i - P \sin \lambda = 0$$

$$\Sigma E = \Sigma (P_i^2 + m_i^2)^{1/2} - [(P^2 + m^2)^{1/2} + M] = 0$$

where  $P$ ,  $\lambda$ ,  $\phi$  and  $m$  are the momentum, dip angle, azimuthal angle and mass of the beam particle and  $P_i$ ,  $\lambda_i$ ,  $\phi_i$  and  $m_i$  are the same variable for outgoing tracks.  $M$  is the mass of the target (proton).

During the kinematical fitting for  $V^0$  productions, KINEMATICS first fitted the decay products to a  $V^0$ , constraining it to the production vertex (3-constraint fit). In case of gamma rays, only reconstructed gamma rays were passed to KINEMATICS and not the electrons.



Table 3.1: KINETMATIC FITS ATTEMPTED IN KINEMATICS

Reaction	Fits Attempted	No. of Constraint*
0-prong + VEE	$K^-P \rightarrow \Lambda^0\pi^0$	4 C
	$\rightarrow \bar{K}^0 n$	4 C
0-prong + VEE + 1 $\gamma$	$K^-P \rightarrow \Lambda^0\pi^0$	5 C
	$\rightarrow \Sigma^0\pi^0$	5 C
0-prong + VEE + 2 $\gamma$ 's	$K^-P \rightarrow \Lambda^0\pi^0$	8 C
	$\rightarrow \Sigma^0\pi^0$	6 C
0-prong + VEE + 3 $\gamma$ 's	$K^-P \rightarrow \Sigma^0\pi^0$	9 C
2-prong	$K^-P \rightarrow K^-P$	4 C
	$\rightarrow \pi^+\pi^-$	1 C
	$\rightarrow \pi^-P$	1 C
2-prong + VEE	$K^-P \rightarrow \Lambda^0\pi^+\pi^-$	7 C
2-prong + Kink	$K^-P \rightarrow \Sigma^-\pi^+$	4 C
	$\rightarrow \Sigma^+\pi^-$	4 C
2-prong + Kink + 1 $\gamma$	$K^-P \rightarrow \Sigma^+\pi^-$	5 C
2-prong + Kink + 2 $\gamma$ 's	$K^-P \rightarrow \Sigma^+\pi^-$	8 C
3-prong	$K^- \rightarrow \pi^+\pi^-\pi^-$	4 C

\* No. of constraints = 4 constraints for each vertex +  
No. of measured parameters - no. of parameters for all  
particles of the event.

Since the geometry information for the tracks passed to KINEMATICS were all in hydrogen, the programme did not need to be modified for the T.S.T. events, but it had to be modified to handle "at rest" events. This was done at Durham (ref. 3.3) by increasing the tolerance allowed for the constraint imbalance from  $0.25 \times 10^{-6}$  to  $2.0 \times 10^{-6}$  and also by modifying the swimming routine so that when the production vertex momentum is less than 50 MeV/c, the normally returned vertex slope was multiplied by the function  $\left[1 + \cot\left(\frac{\pi}{2} \times \frac{P}{.05}\right)\right]^{-1/2}$  where P is in GeV/c. This function has a value of unity at  $50 \frac{\text{MeV}}{c}$  and zero at  $P = 0$  and consequently in low momentum fitting the end point momentum is progressively decoupled from the centre of track value.

### 3.3.5 Judge

It has been found experimentally that the number of bubble  $n$  produced per unit length of a track (Ionisation density) is related to the velocity  $\beta$  of the particle concerned by

$$n = n_0 / \beta^2$$

or, replacing  $\beta$  by  $p/\epsilon$  where  $p$  and  $\epsilon$  are momentum and total energy of the particle respectively, we have

$$n = n_0 \left(1 + \frac{m^2}{p^2}\right) \quad (3.2)$$

This shows that as the momentum of the particle becomes larger the ionisation density varies down to the minimum values  $n_0$  or  $n/n_0$  (relative bubble density) approaches unity. This variation is shown in Fig. 3.6 for pions, kaons and protons.

Experimentally, it is possible to distinguish relative bubble densities in excess of 1.4 by eye from the minimum of 1. In other words,

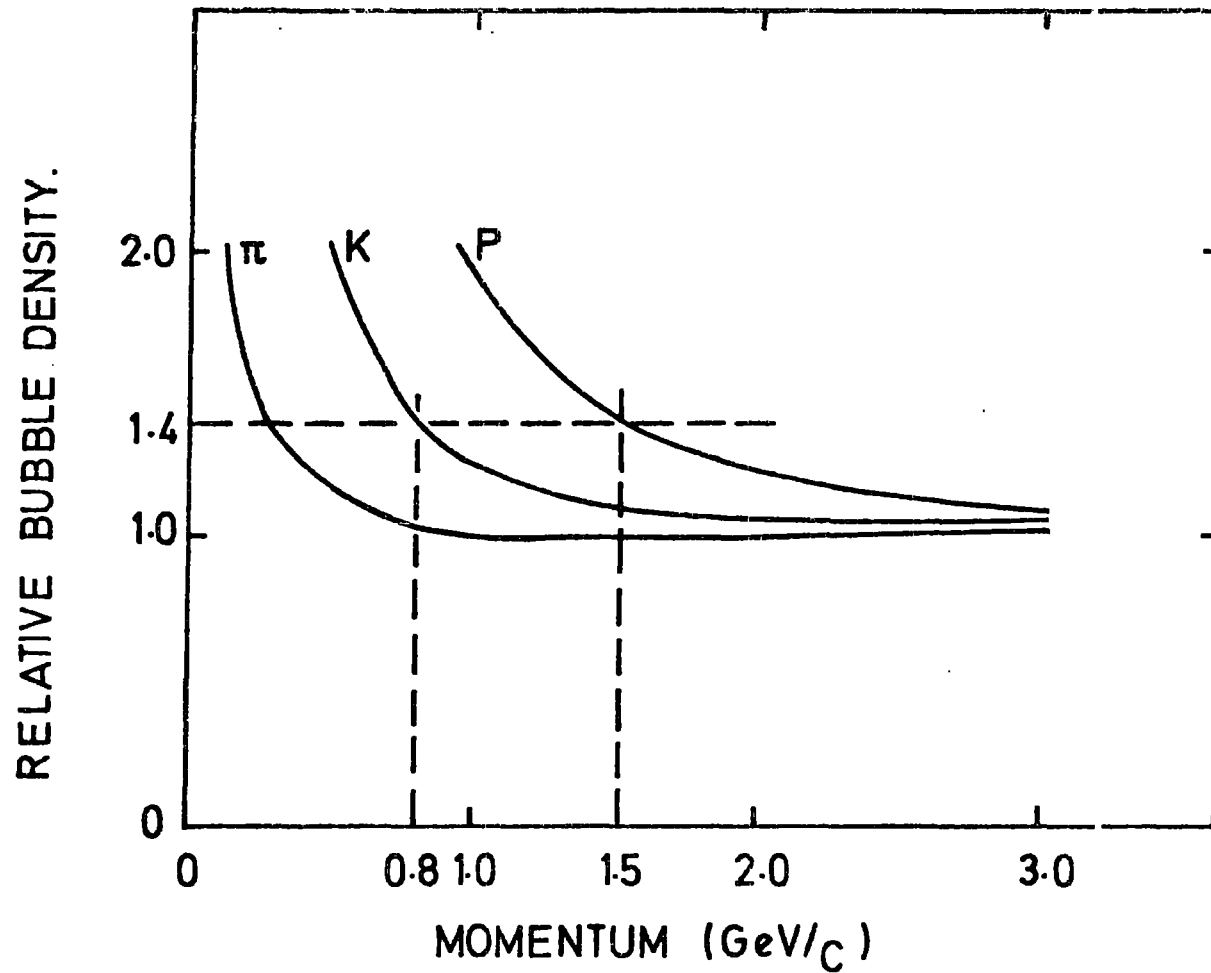


FIG. 3.6

THE RELATIVE BUBBLE DENSITY AS A FUNCTION OF THE PARTICLE MOMENTUM (PION, KAON AND PROTON)

from Fig. 3.6, pions, kaons and protons can be distinguished from each other by eye at low momentum.

By making use of this advantage, we could resolve, in most of the cases, ambiguities between fitted hypotheses by judging the ionisation of tracks by eye. For example,  $\Lambda^0/K^0$  ambiguity was resolved by examining the positive track of the  $V^0$  and the same for  $\Sigma^+$  which could decay either to proton or  $\pi^+$ . However, when  $\pi^+$  from  $\bar{K}^0$  or  $\Sigma^+$  decay were heavily dipped and it did not stop in the hydrogen chamber, it was possible for it to be mistaken for proton.  $\Sigma^-$  decay could be ambiguous with  $K^-$  decay. This ambiguity was also resolved by examining the positive track which is heavily ionising (proton) for K scattering followed by decay and which is lightly ionising for  $\Sigma^-$  production and decay. This requirement made it possible to distinguish  $\Sigma^-$  production from elastic scattering. Three-prong events could be ambiguous between tau decays and one-prong events plus Dalitz pair. All ambiguous three-prong events were selected as tau decays unless the spiral appearance of an electron or positron was shown by one of the prongs. However, if no final decision could be made on an event, the event passed to D.S.T. (see Section 3.8) as ambiguous, together with events which had passed all tests.

At the same time that judging was carried out, the following checks and decisions were also made:

- (i) events which failed in the geometrical reconstruction were checked to see if they were measureable.
- (ii)  $\Lambda^0$  and  $\Sigma^+$  (decaying to proton) events were scanned again for associated gamma rays.
- (iii) events which were declared by measurers to be not measureable at measuring time and those which were declared to be spurious events were checked to make sure that the decisions made by measurers were correct.

(iv) the physical classification of the event was made by the judging physicist.

In practice two Judge passes were made, one after each of the first and second measurements of events. It should be emphasised that the film has:-

- (a) been scanned twice,
- (b) been measured three times,
- (c) been judged twice.

In all three steps the film has been scrutinized for associated gamma rays. Although it is difficult to estimate a scanning efficiency, this emphasis on  $\gamma$ -detection will have lead to a high rate of detection.

### 3.3.6 Data Summary Tape (D.S.T.)

Those events which had fitted one or more physical channels were written on a data summary tape to be analyzed later in terms of physics. The D.S.T. contained, for each event, information such as x, y, z co-ordinates for all vertices, fitted and unfitted momenta, angles and the length for each track.

### 3.3.7 Masterlist

In order to control the processing chain, a system called Masterlist was employed. Each event found in scanning is given a record on a Masterlist file. The record consists of 20 parts giving scan information, a status word which indicates the stage of processing to which the event has reached and the fitted hypotheses. All statistics given in the next chapter were obtained from Masterlist.

## CHAPTER 4

BASIC EXPERIMENTAL DATA

In this chapter some preliminary results extracted from Durham data will be described.

4.1 Scanning

A total of 41 half-rolls of film were scanned and rescanned, the result of which are shown in table 4.1.

Table 4.1: Durham Scanning data

Class of Events	No. Scanned	(Scan Eff.) %	Corrected No. of events
0 Prong + VEE	7571	93.7	8080
2 Prongs	4172	-	-
2 Prongs + VEE	601	89.2	673
Sigma (-)	4013	95.8	4188
Sigma (+)	4799	96.2	4988
3 Prongs	3602	98.1	3671
Pi-mu-e	841	-	-
TOTAL	25599	-	-

4.1.1 Scanning Efficiencies

In order to evaluate scanning efficiencies, all film used in this experiment was double scanned except two prong events for which double scanning was carried out on a subset of film only. About 10% of film was scanned for a third time to check the scanning efficiencies evaluated on the basis of double scan (ref. 4.1). The overall scanning efficiency can be found as follows:

In 2 independent scans a particular event can be seen on the first scan only (missed on second scan), on the second scan only (missed on first scan) or on both scans. Defining the following quantities:

- $N_1$  = number of events seen on first scan only
- $N_2$  = number of events seen on second scan only
- $N_{12}$  = number of events seen on both scans
- $N_T$  = actual number of events on the film
- $\epsilon_1$  = single scan efficiency (first scan)
- $\epsilon_2$  = single scan efficiency (second scan)

then the following expressions can be written:

$$\epsilon_1 = \frac{N_1}{N_T} \quad \text{and} \quad \epsilon_2 = \frac{N_2}{N_T} \quad (4.1)$$

The probability of seeing an event on both scans is  $\epsilon_1 \cdot \epsilon_2$  and therefore ,

$$N_{12} = \epsilon_1 \cdot \epsilon_2 \cdot N_T \quad (4.2)$$

From equations (4.1) and (4.2), the following expressions can be derived ,

$$\epsilon_1 = \frac{N_{12}}{N_2} \quad , \quad \epsilon_2 = \frac{N_{12}}{N_1}$$

and

$$N_T = \frac{N_1 \cdot N_2}{N_{12}}$$

To determine the overall scanning efficiency from the two scans combined ( $\epsilon_C$ ), we define q as the probability of seeing an event on neither of the two scans which in terms of  $\epsilon_1$  and  $\epsilon_2$  can be written as ,

$$q = (1 - \epsilon_1)(1 - \epsilon_2) \quad (4.3)$$

and since  $\epsilon_C = 1 - q$ , then

$$\epsilon_C = \epsilon_1 + \epsilon_2 - \epsilon_1 \cdot \epsilon_2 \quad (4.4)$$

The scan efficiencies were used to calculate the weighted number of events for cross-section determination.

#### 4.2 Measurement

In Table 4.2 the number of events measured in each channel as well as the number of immeasurable events, are shown.

Table 4.2: Measurement of Durham events

Class of Events	No. Measured	Immeasurable
0 Prong + VEE	7388	183
2 Prongs	4086	86
2 Prongs + VEE	554	47
Sigma (-)	3739	262
Sigma (+)	4469	330
3 Prongs	3519	83
Pi-mu-e	841	-
TOTAL	24596	991

In the stage of JUDGE some 3265 events were eliminated because the interaction had occurred inside the perspex walls & ~ 94% of these were zero prong events. Also 254 events were identified as being neon events (see Section 3.1(d)) and therefore were excluded from the data. The final statistics together with the Geometry and Kinematics pass rates are shown in Table 4.3.

#### 4.3 Gamma Rays Detection Efficiency

The gamma rays produced in this experiment have originated from the



Table 4.3: Details of the data available at the present time

Class of Events	No. Scanned	No. Measured	Passed Geometry	Geom. Pass Rate %	Passed Kinematics	Kin. Pass Rate %	Overall Pass Rate %
0 Prong + VEE	4520	4336	4072	93.9	3819	93.8	88.1
2 Prongs	4121	4029	3958	98.2	3814	96.3	94.5
2 Prongs + VEE	579	501	451	90.0	377	83.4	75.1
Sigma (-)	3977	3692	3560	96.4	3197	89.8	86.6
Sigma (+)	4748	4409	4221	95.7	3866	91.6	87.6
3 Prongs	3548	3269	3212	98.2	3141	97.7	95.9
Pi-mu-e	841	841	-	-	-	-	-
TOTAL	22314	21077	19474	-	18214	-	-

decay of  $\Sigma^0$ 's and  $\pi^0$ 's. These gamma rays would convert into electron-positron pairs or produce Compton electrons in the neon-hydrogen mixture in which case they could be detected. A Monte-Carlo analysis using the programme, FAKE, revealed that the contribution from Compton scattering in this experiment was negligible compared to that of pair productions.

In order to estimate the number of gamma rays lost in this experiment due to the geometry of the chamber, some few thousands of events of the type  $K^-P \rightarrow \Sigma^0\pi^0$  were simulated by FAKE and the decay products from  $\Sigma^0 \rightarrow \Lambda^0\gamma$ ,  $\pi^0 \rightarrow \gamma\gamma$  and  $\Lambda^0 \rightarrow P\pi^-$  were generated isotropically in the rest frame of the parent particle (the programme, FAKE, which randomly generates events in the centre of mass system for two body final states had to be modified according to the T.S.T. chamber arrangement. The author has been responsible for modifying it in two main respects. Firstly the programme has been modified to allow for the new complex geometry of the double chamber system. Secondly the programme has been modified to allow for the variation with energy of the cross-sections for interaction. The author has also carried out an initial survey of the feasibility of using the chamber system to search for the rare  $\Lambda P$  interaction. The programme has also been modified to handle gamma rays (converting through pair production or through the Compton process.) The result of this simulation showed that about 75% of all gamma rays did not convert into  $e^+e^-$  pairs, i.e. the conversion efficiency is about 25%.

Apart from the geometrical loss, there are also losses due to the gamma ray measuring inefficiencies. These losses are caused mainly by: (i) low-energy gamma rays, (ii) dipping gamma rays, and (iii) by those gamma rays in which one of the electrons has a relatively small share of the gamma ray energy.

When these losses are taken into account the effective gamma ray

conversion efficiency tends to drop to  $\sim 15\%$ . This can be compared with the value derived from measured  $\Sigma^+ \pi^-$  events in which  $\Sigma^+ \rightarrow p\pi^0$ ,  $\pi^0 \rightarrow \gamma\gamma$ .

In these events if the probability of seeing one of the two gamma rays is  $p$ , then from the binomial expansion, the number of  $\Sigma_p^+$  associated with one or two gamma rays are

$$\begin{aligned} N_{\Sigma} + 1\gamma &= 2p(1-p)N \\ N_{\Sigma} + 2\gamma &= p^2N \end{aligned} \tag{4.5}$$

where  $N$  is the total number of  $\Sigma_p^+$  events. The number of  $\Sigma^+$  events with one or two gammas were known (from MASTERLIST) to be 363 and 31 respectively. Hence, solving equations (4.5) leads to  $p = 14.6\%$  in good agreement with the FAKED value.

#### 4.4 Gamma Conversion Length

In order to determine the average conversion length for a gamma ray in our neon-hydrogen mixture the following method has been used.

Assuming that the number of gamma rays entering the mixture is  $N_0$ , and  $N(L)$  of them have survived materialisation after travelling a distance  $L$ , then from the law for a random process ,

$$N(L) = N_0 e^{-L/L_C} \tag{4.6}$$

where  $L_C$  is the gamma conversion length. Differentiating this will lead to

$$dN(L) = -\frac{N_0}{L_C} e^{-L/L_C} dL$$

and therefore the average gamma length is

$$\bar{L} = \frac{\int_{L_{\min}}^{L_{\max}} L dN(L)}{\int_{L_{\min}}^{L_{\max}} dN(L)} \tag{4.7}$$

Setting  $L_{\min}$  to 0 and  $L_{\max}$  to the potential length, PL, for a gamma ray defined as the distance from the entrance to the neon-hydrogen chamber to the end of the fiducial volume along the gamma ray direction, we have

$$\bar{L} = \frac{L_C - L_C e^{-PL/L_C} - PL e^{-PL/L_C}}{1 - e^{-PL/L_C}} \quad (4.8)$$

In Fig. 4.1  $\bar{L}$  is plotted against PL for different values of  $L_C$ .

To evaluate  $L_C$ , for every gamma ray that converted into  $e^+e^-$  pairs in the chamber, the potential length and the length of the gamma ray itself was computed (the lengths were measured from the entrance to neon-hydrogen mixture. This excluded all gamma rays materialised in hydrogen which amounted to about 3% of all gamma rays). Then all gamma rays were grouped into gamma rays with potential length of  $P_L, P_L + \Delta L$  where  $\Delta L = 5$  cm. and the average potential length and gamma decay length for each group were calculated ( $\overline{PL}_O, \bar{L}_O$ ). The result of this is shown in Fig. 4.2. The value of  $L_C$  was determined by minimizing the function.

$$F(L_C) = \sum \left[ \frac{(\bar{L}_O - \bar{L})}{\sigma} \right]_{\text{over all bins}}^2$$

where  $\bar{L}$  is calculated from equation (4.8) for  $\overline{PL}_O$  and  $\sigma = \frac{\bar{L}}{\sqrt{N}}$  where N is the total number of gamma rays in each bin.

This gave a value of  $36_{-10}^{+20}$  cm for the conversion length  $L_C$ . From this the associated radiation length should be  $28_{-7}^{+15}$  cm which is roughly consistent with the expected value of about 45 cm.

#### 4.5 Calibration of The Magnetic Field

The correction factor for the magnetic field was calculated by comparing the computed Q-values for  $V^0$  events with their nominal values (37.75 MeV for  $\Lambda^0$  and 218.56 MeV for  $\bar{K}^0$ ).

A sample of 178  $\Lambda^0$ 's and a sample of 126  $\bar{K}^0$ 's were selected from

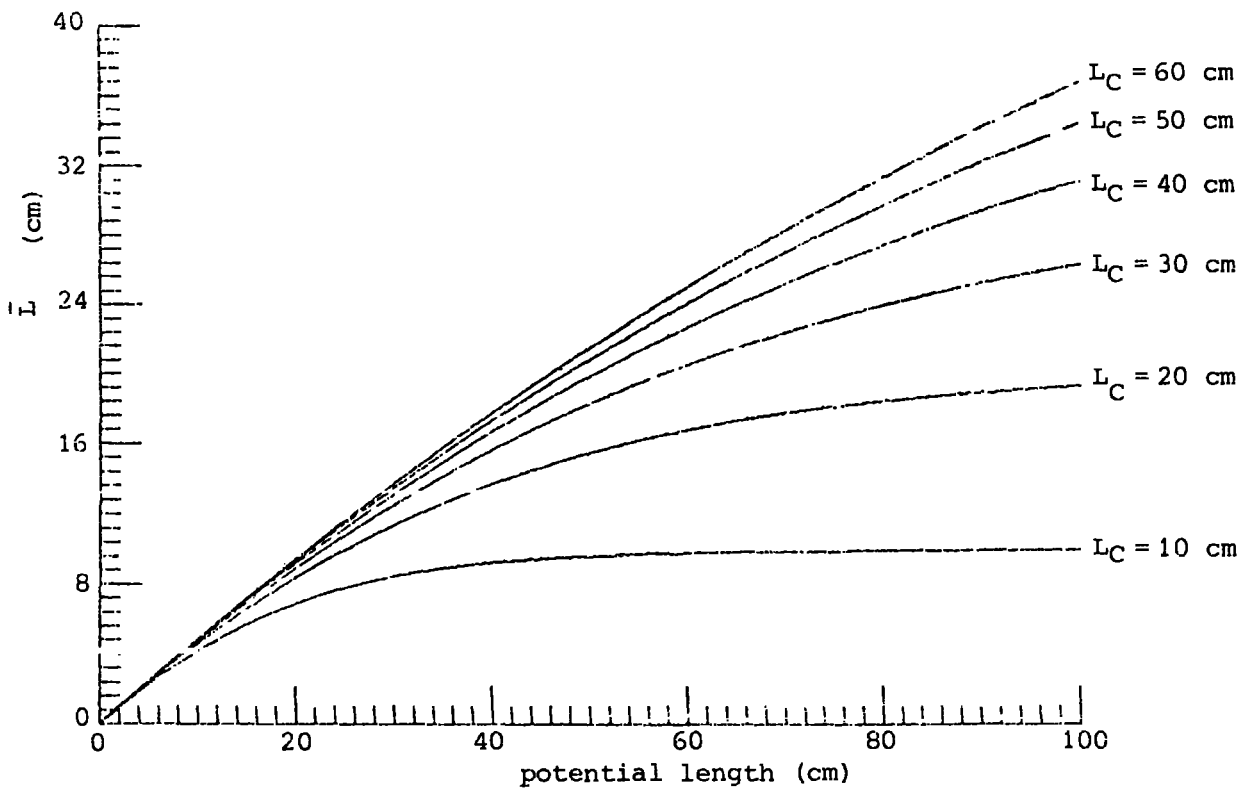


Figure 4.1: Calculated gamma ray length as a function of potential length for different values of conversion length.

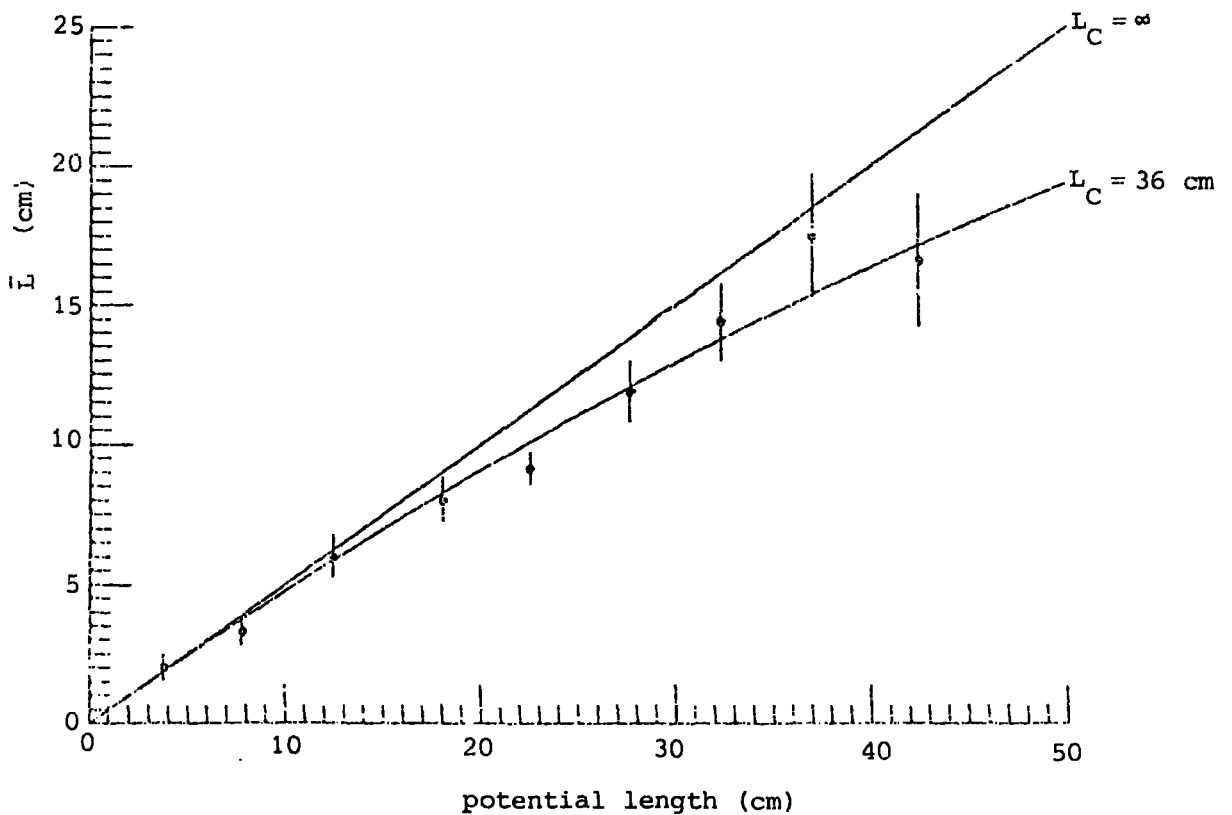


Figure 4.2: Experimental determination of  $L_C$

the Durham data that satisfied the following criteria:

- (1) The  $Z$ -coordinates of the primary vertex lay between 19.8 and 26.8 cm.
- (2) The error on measuring  $(1/p)$  was less than 10%.
- (3) The track length of the decay particles ( $\Lambda^0 \rightarrow \pi^- p$ ,  $\bar{K}^0 \rightarrow \pi^+ \pi^-$ ) was at least 5 cm. in hydrogen.

If the magnetic field that has been used in KINEMATICS ( $H$ ) is related to its true value ( $H_0$ ) by the relation  $H = H_0 (1 + e)$ , then the apparent and true  $Q$  values are related as

$$Q^2 - Q_0^2 = 2e \left[ M_0^2 - m_1^2 (1 + E_2/E_1) - m_2^2 (1 + E_1/E_2) \right] - 2(m_1 + m_2)(M - M_0)$$

where  $Q, M \equiv$  computed  $Q$ -value and invariant mass for the decaying particle using measured values of  $P, \phi$  and  $\tan \lambda$

$Q_0, M_0 \equiv$  The known values

$E_1, E_2 \equiv$  Computed energy of the decay particles

$m_1, m_2 \equiv$  Masses of the decay particles .

In deriving the above equation the following approximations were used:

$$E \approx (E_0^2 + 2e P_0^2)^{1/2} \approx E_0 (1 + e P_0^2 / E_0^2)$$

where  $E_0$  and  $P_0$  are the true values of energy and momentum.

$$\frac{E_{i0}}{E_{j0}} \approx \frac{E_i - e P_{i0}^2 / E_{i0}}{E_j - e P_{j0}^2 / E_{j0}} \approx \frac{E_i}{E_j}$$

The  $Q$ -value distributions for  $\Lambda^0$  and  $\bar{K}^0$  are shown in Figs. 4.3 and 4.4 respectively. The mean and standard error on the mean for  $Q$ -values and  $e$  are as follows:

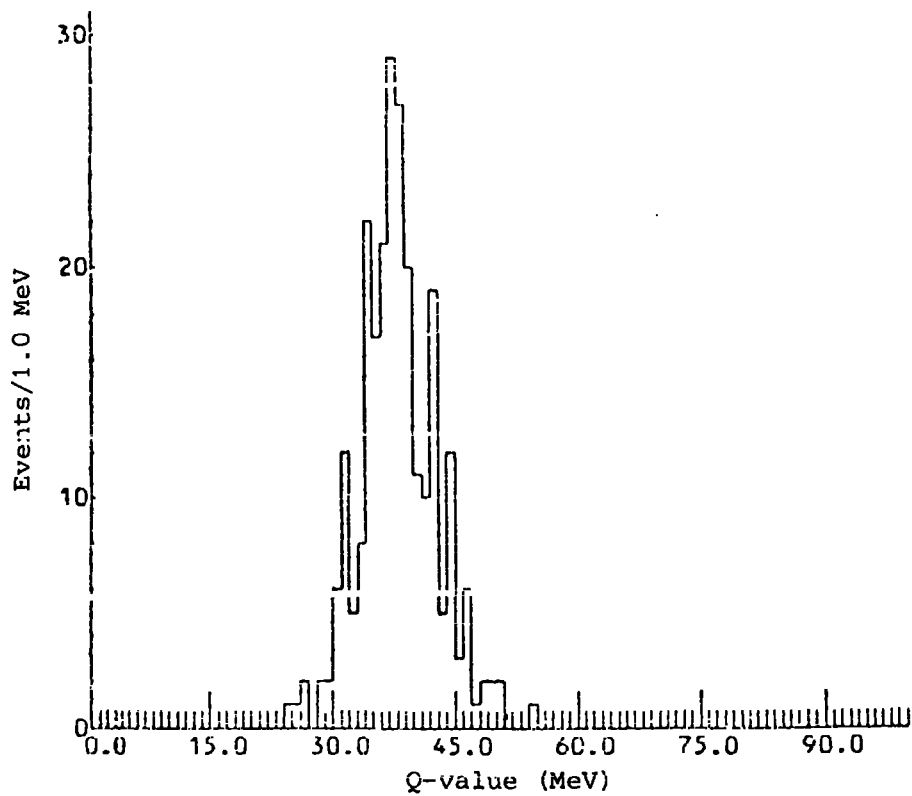


Figure 4.3: Q-value distribution for  $\Lambda^0$ -hyperons

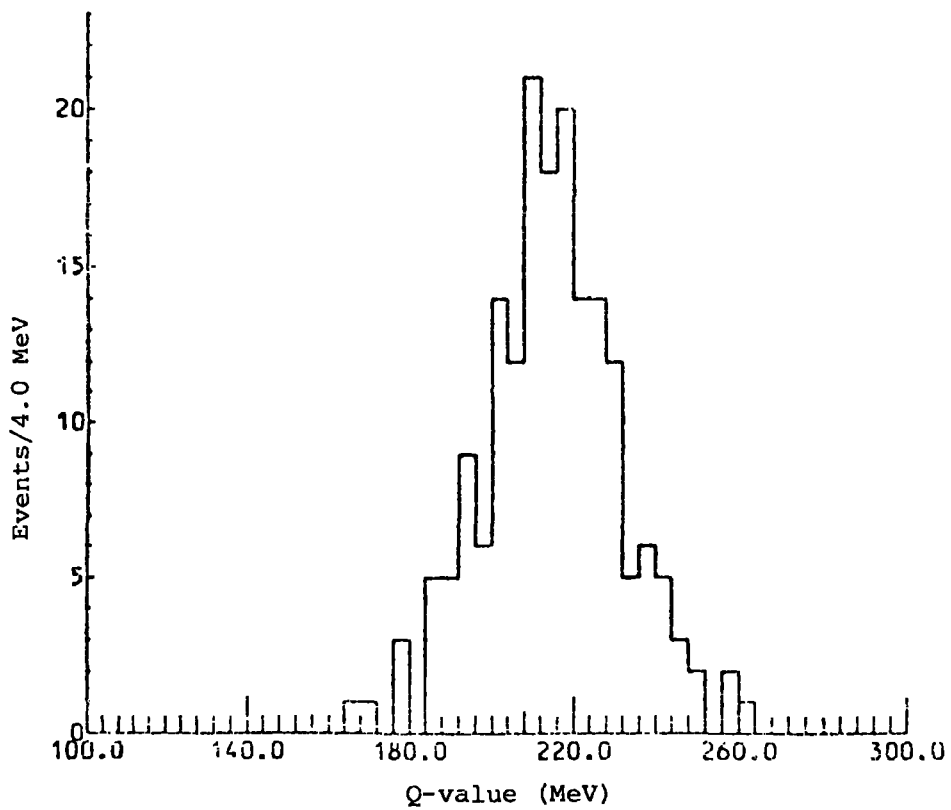


Figure 4.4: Q-value distribution for  $\bar{K}^0$ -mesons

For  $\Lambda^0$

$$\bar{Q} = .03779 \pm .00036$$

$$\bar{e} = .00239 \pm .00570$$

which led to

$$h = \frac{H_o}{H} = \frac{1}{1 + \bar{e}} = .998 \pm .006$$

For  $\bar{K}^0$

$$\bar{Q} = .21608 \pm .00139$$

$$\bar{e} = -.00663 \pm .00421$$

which led to

$$h = 1.007 \pm .004$$

and the overall correction factor which must be applied to the magnetic field were calculated to be  $1.003 \pm .003$ . This shows that not only the magnetic field used in this experiment was accurate enough, but the measuring system in Durham was very satisfactory too.

#### 4.6 Reconstruction Accuracy in the T.S.T.

##### Stretch Distribution of tau-mesons

The stretch distributions of  $\phi$ ,  $\tan \lambda$  and  $1/p$  for the primary and for the pion secondary particles are shown in Figs. 4.5 to 4.10 respectively where the stretch on a quantity  $Q$  is defined as

$$S = \frac{Q_f - Q_u}{(\sigma_u^2 - \sigma_f^2)^{1/2}} \quad (4.9)$$

where the  $\sigma$ 's are errors and u and f refer to unfitted and fitted quantities at the mid-point of a track. The mean values, standard deviations and kurtosis of the distributions are given in Table 4.4. The expected values for these quantities for gaussian distributions are



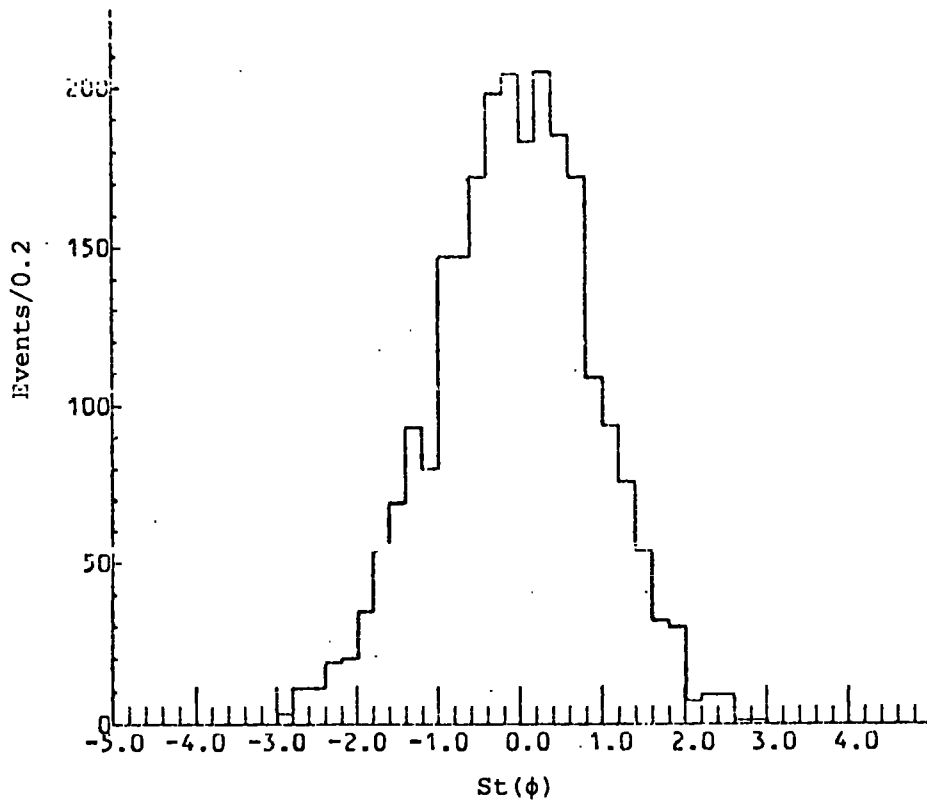


Figure 4.5: Stretch distribution of  $\phi$ -angle  
for the beam

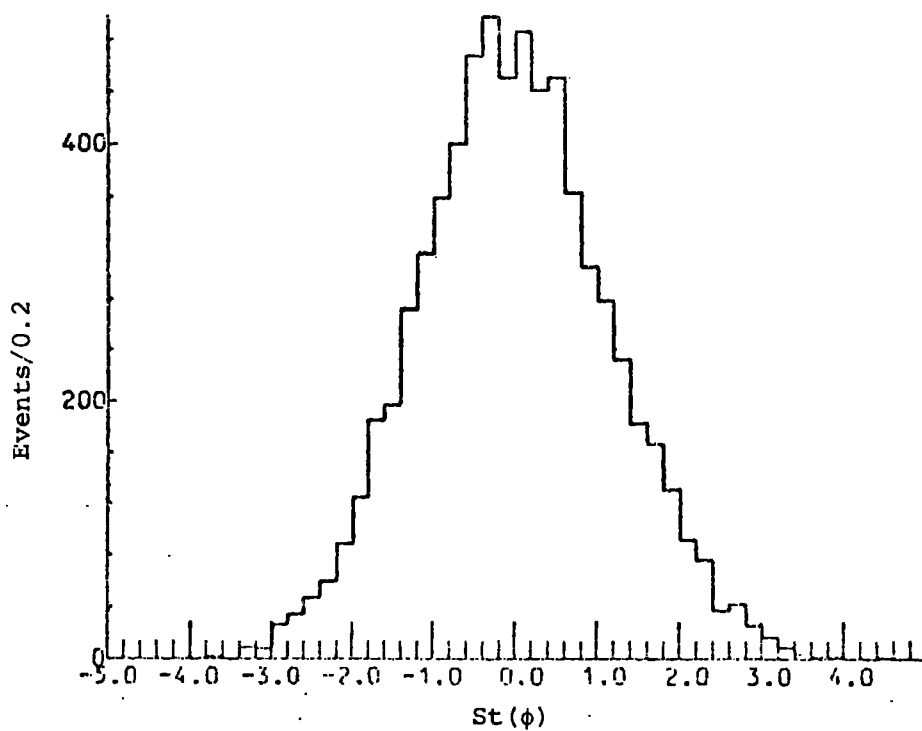


Figure 4.6: Stretch distribution of  $\phi$ -angle  
for the outgoing pions

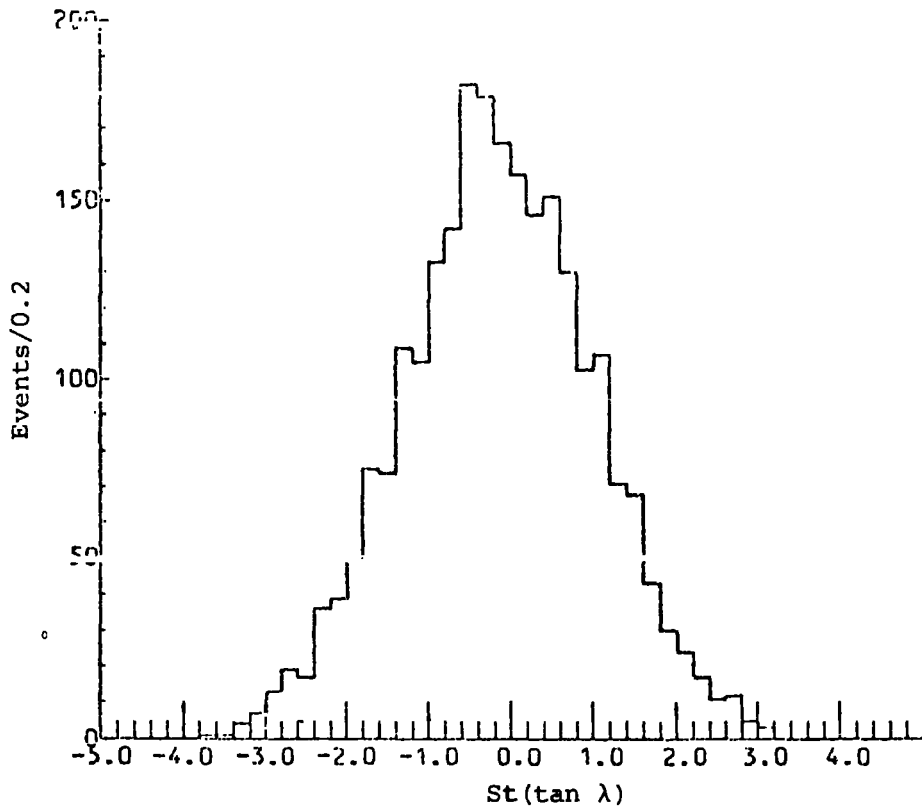


Figure 4.7: Stretch distribution of  $\tan \lambda$  for the beam

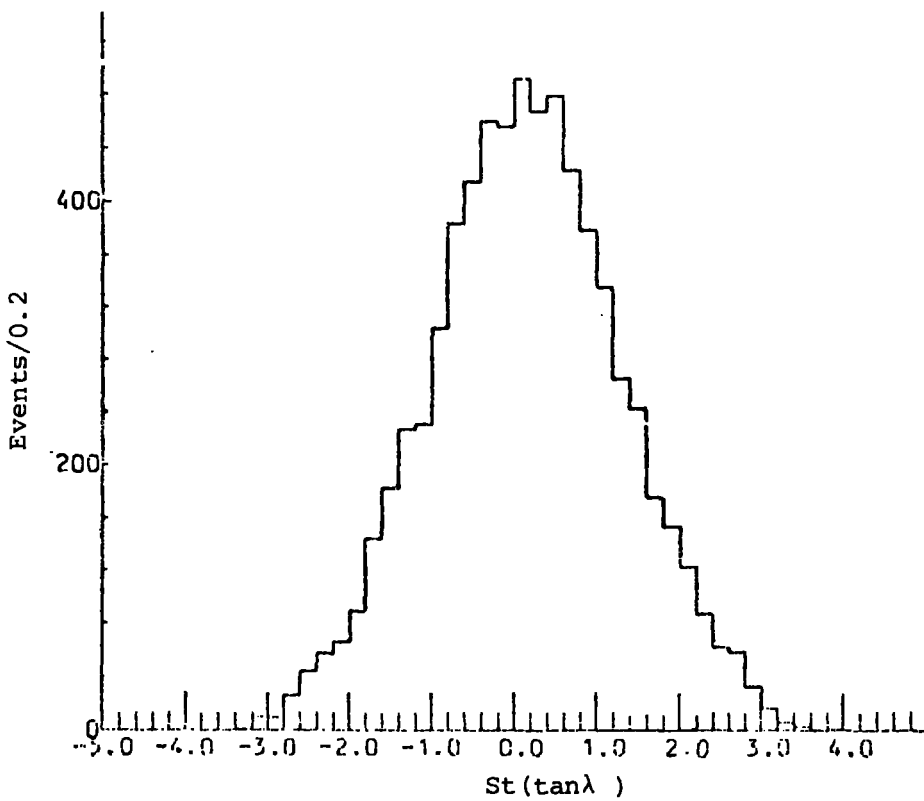


Figure 4.8: Stretch distribution of  $\tan \lambda$  for the outgoing pions

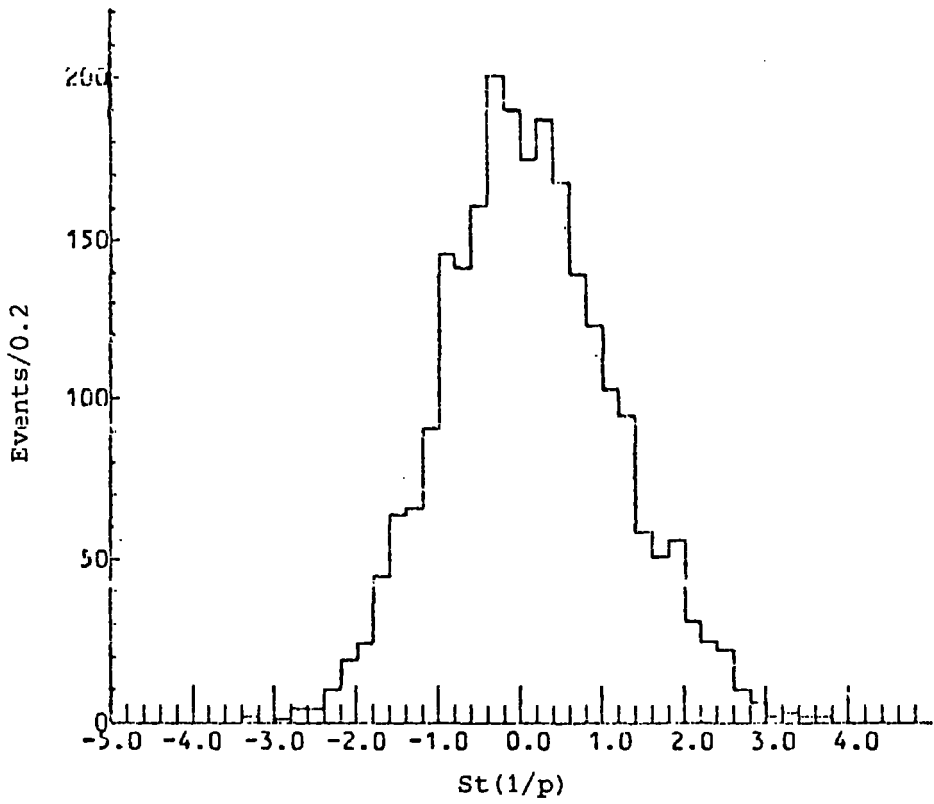


Figure 4.9: Stretch distribution of  $1/p$  for the beam

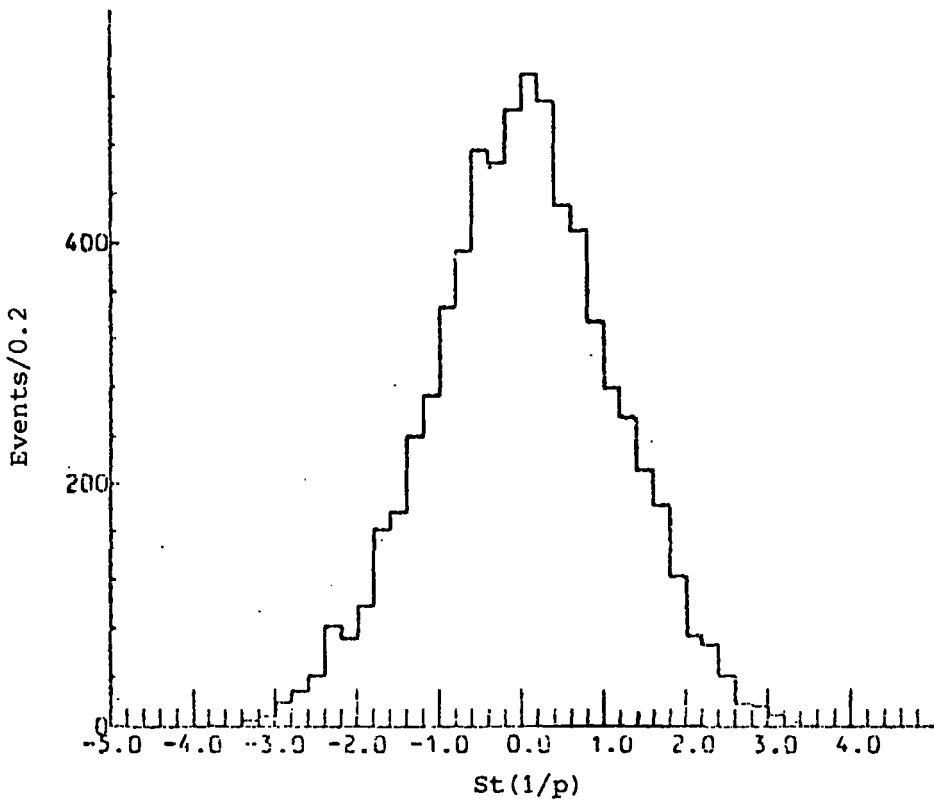


Figure 4.10: Stretch distribution of  $1/p$  for the outgoing pions

0, 1 and 3 respectively. It is clear from the table that whereas the kurtosis and standard deviation of the distributions are consistent with standard Gaussian distributions, the mean values, particularly for stretches on  $\tan \lambda$ , are not zero. The rest of this section is an investigation into the possible causes of this discrepancy and a consideration of its importance.

Table 4.4

Quantity	P R I M A R Y			S E C O N D A R I E S		
	Mean	S.D.	Kurtosis	Mean	S.D.	Kurtosis
$\phi$	$-.072 \pm .019$	0.961	2.924	$.011 \pm .013$	1.096	2.929
$\tan \lambda$	$-.153 \pm .023$	1.140	2.842	$.145 \pm .013$	1.136	2.809
$1/p$	$.102 \pm .021$	1.044	2.989	$-.020 \pm .014$	1.153	2.939

Mean, standard deviation and Kurtosis of stretch distributions of tau-mesons.

4.6.1 Importance, if any, of non-zero stretch

In Fig. 4.11 the  $\chi^2$  probability of the tau-mesons fit is shown. On the whole this is well behaved apart from a peak at low probabilities. This peak in distributions for other physical channels is usually interpreted as arising from events being spuriously fitted to the channel, e.g. a 4C event being unambiguously fitted as a 1C event. It must be pointed out that in the present case there is no other physical channel which can be spuriously fitted as a tau-meson. (For example  $\bar{K} \rightarrow \pi^- e^+ e^- \gamma$  is removed entirely at the judging stage since the  $e^+ e^-$  pair is readily recognized). The low probability peak implies a basic problem in the fitting routines and that some genuine tau-mesons are fitted with very

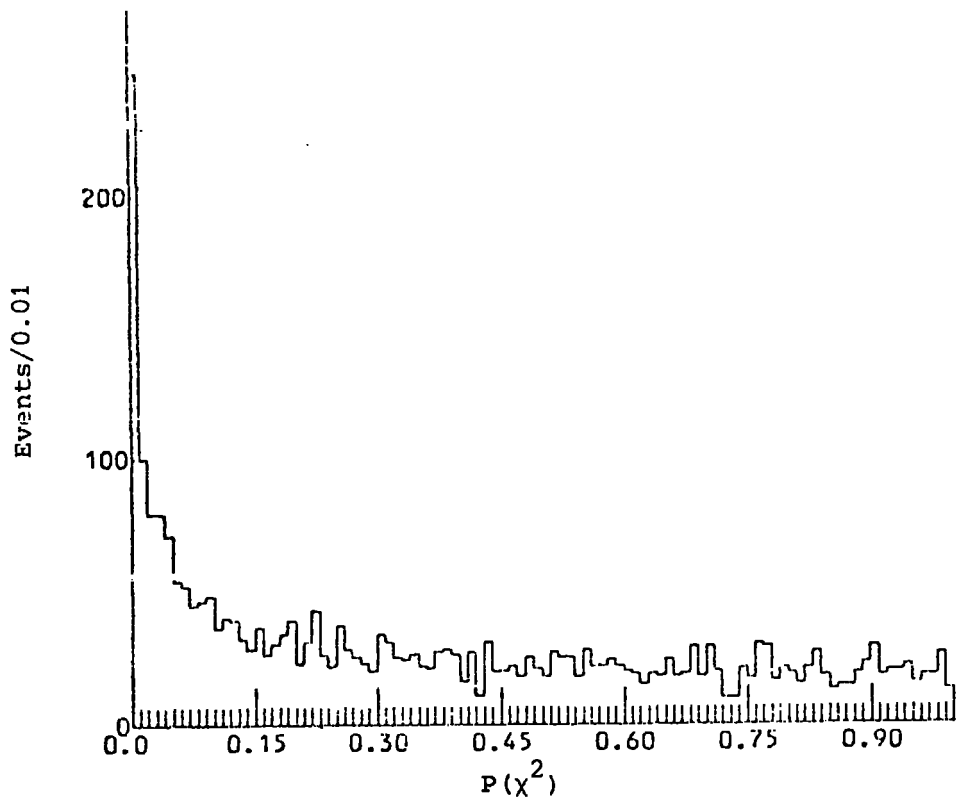


Figure 4.11:  $\chi^2$  - probability distribution for  $\tau$ -mesons

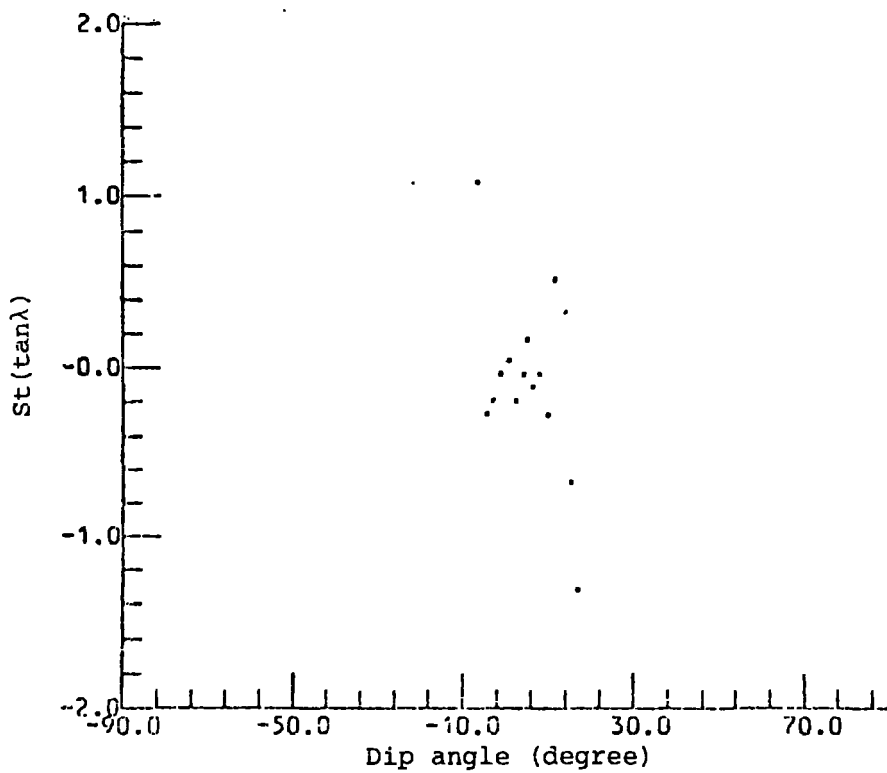


Figure 4.12 Variation of  $St(\tan\lambda)$  for the beam with dip angle

low probability.

Apart from these events the flat probability distribution would imply that on the whole the reconstruction of events is correctly handled and that the non-zero stretch on  $\tan \lambda$  may not have any great significance.

#### 4.6.2 Causes of non-zero stretch on $\tan \lambda$

A variety of checks have been made and no clear cause of the non-zero stretch has been found. Some of the checks are described below.

##### (a) Low probability events

The average dip-stretch of these events is exactly the same as for the higher probability events so there is no correlation here.

##### (b) Variation of stretch with dip angle

An example of this is shown in Figs. 4.12 and 4.13 for primary and secondaries. It is clear that the average stretch is independent of dip angle. The fluctuation at large values of dip angle arise from the average stretch coming from single events. The stretch distributions of the primaries to neutral hyperon production events and sigma events show exactly the same features.

##### (c) Variation of fitted errors

It is conceivable that the fitted errors going into the stretch expression disturb the distribution in an asymmetric way. This is difficult to check, but what has been demonstrated in Fig. 4.14 is that for all events  $\sigma_f < \sigma_u$ .

The average unfitted errors have been plotted as a function of dip angle. These are shown in Figs. 4.15 and 4.16, together with the average track lengths measured. The shapes and sizes of the curves agree exactly with their expected values from measurements dominated by Coulomb scattering. It is concluded that error treatments are correct.

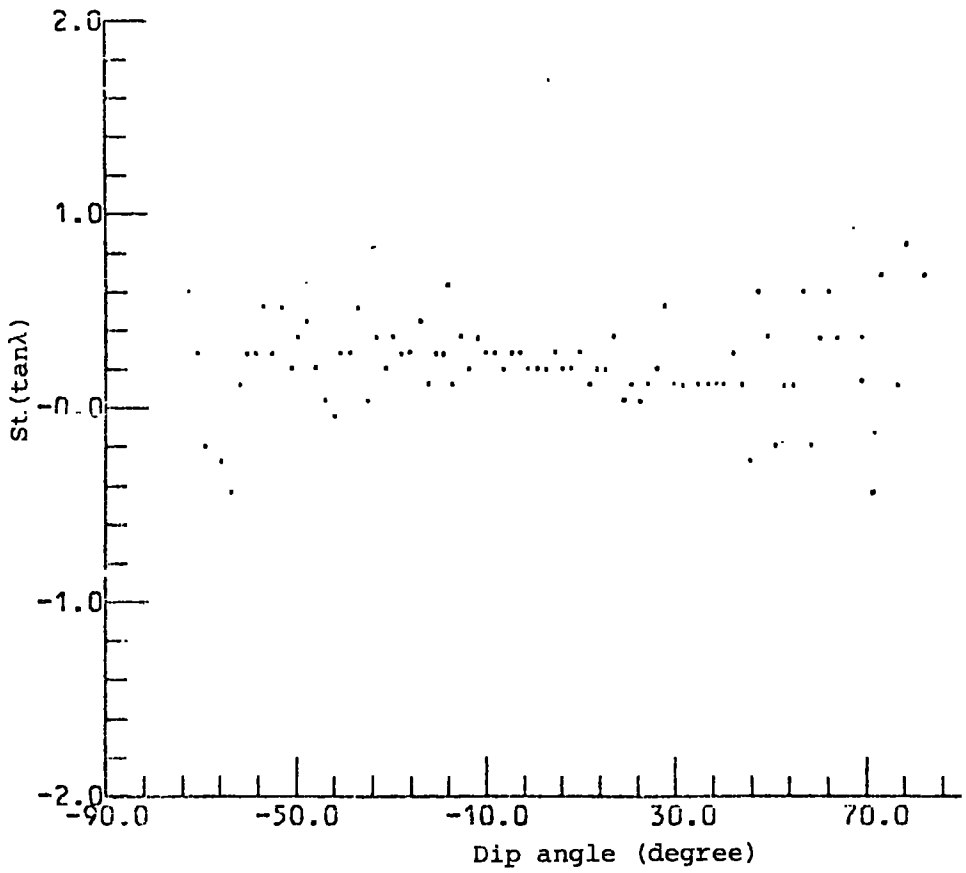


Figure 4.13: Variation of  $St(\tan\lambda)$  for the outgoing pions with dip angle

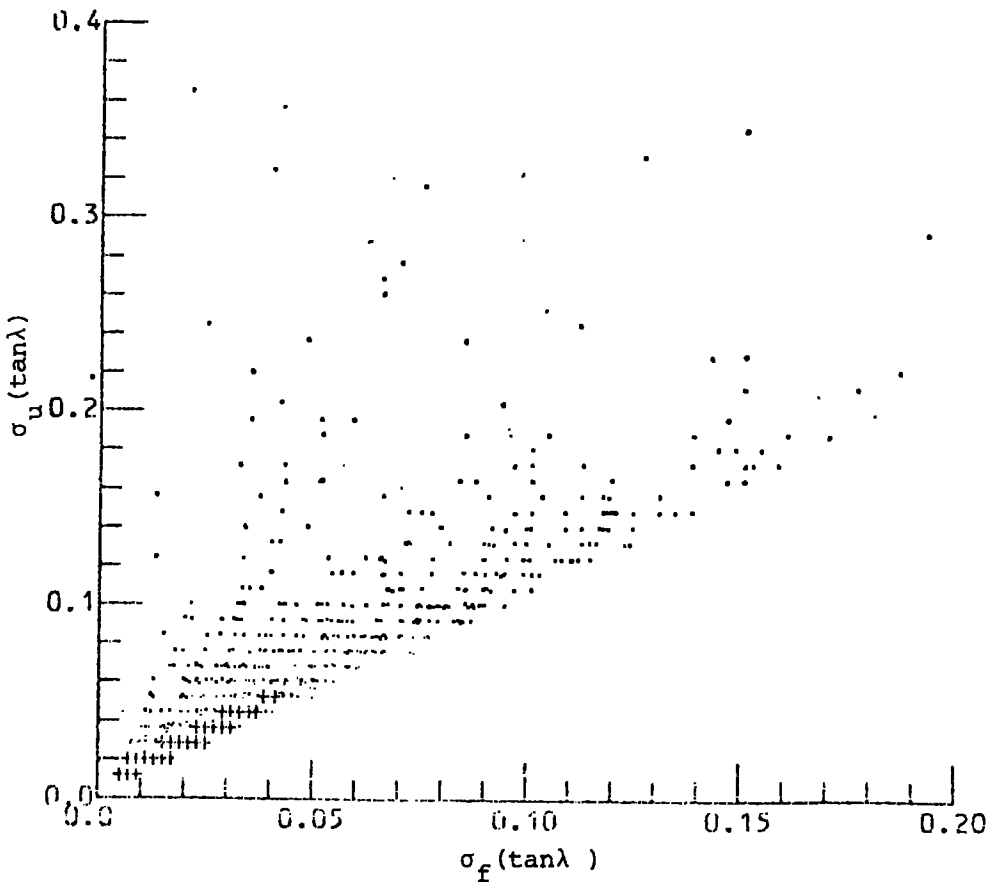


Figure 4.14: Unfitted error on  $\tan\lambda$  versus the fitted error for all tracks

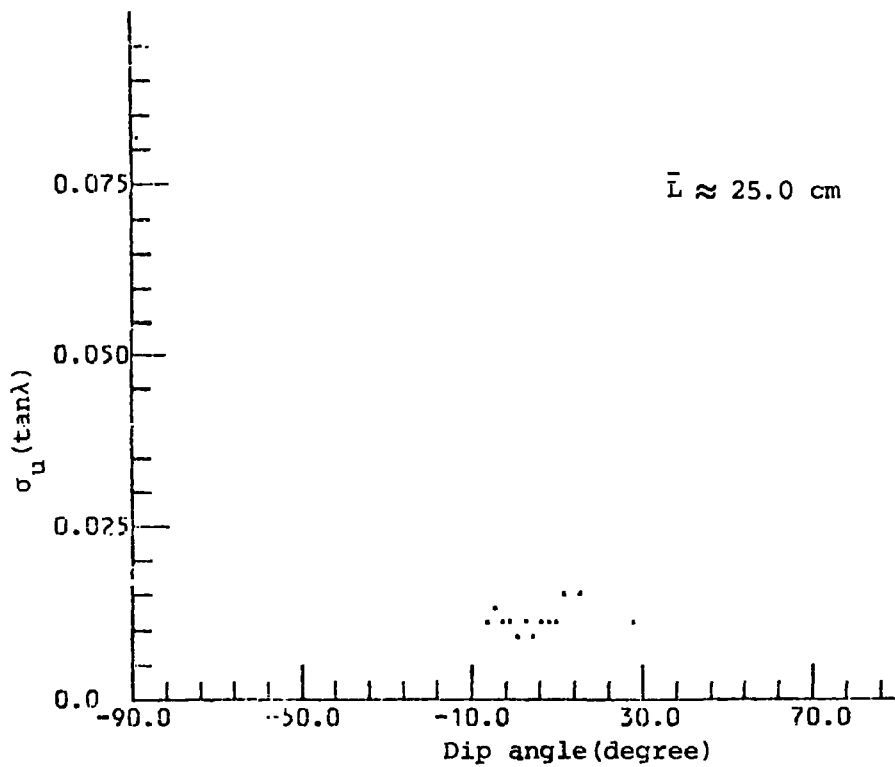


Figure 4.15: The average unfitted errors on  $\tan\lambda$  as a function of dip angle for the beam

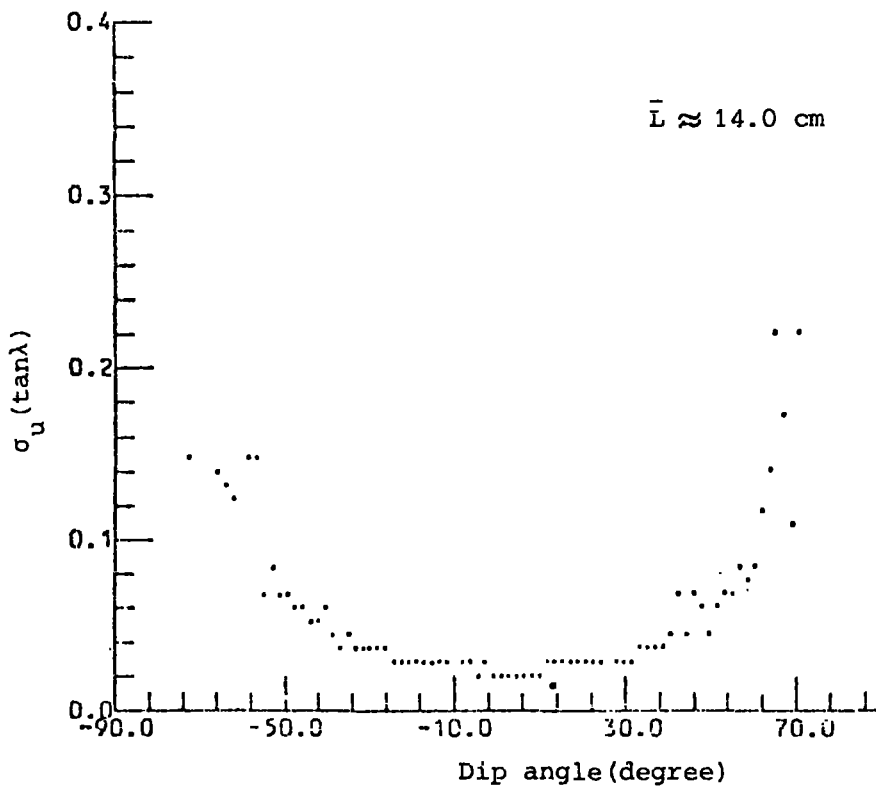


Figure 4.16: The average unfitted errors on  $\tan\lambda$  as a function of dip angle for the outgoing pions



(d) Fitted and unfitted dip angles

Both  $\tan \lambda$  and  $\lambda$  itself have been examined. The average value of  $(\lambda_f - \lambda_u)$  is  $-.0004$  radians for the primary tau-mesons and  $.0013$  radians for the pion secondaries. The equality, but differing signs of the shift in dip angles implies that the event is rotated by  $\sim 2^\circ$  in the fitting process. The source of this rotation is not clear. What has emerged in discussions, which may be related, is that the Mongoose value of the depth of the T.S.T. is  $7.84$  cm. (and this is confirmed by our Z-distributions of primary and secondary vertices of all events), whereas the workshop design value was  $7.5$  cm. Allowing for the contraction from cooling and the thickness of a highly compressed O-ring seal, the true depth is probably a little less than  $7.5$  cm. This means that Z-coordinates are all over-estimated by about  $5\%$ . The difference cannot be explained in terms of the flexing of the T.S.T. during expansion. An attempt to check if there is over-estimation of Z has been made using the range of the isotropically distributed muons from  $\pi \mu e$  decay. This is shown in Fig. 4.17 where the average range is plotted against the dip angle. There is no detectable variation, but at the level of  $5\%$  the sought for variation may be lost in the noise. However an over-estimation of Z cannot account for the average  $2^\circ$  rotation since rotation of events directed downwards would cancel rotation of events directed upwards. However for a track of  $25$  cm. length passing through the whole of the T.S.T. from top to bottom a  $5\%$  variation on Z would give about  $1^\circ$  rotation of the track.

A final check was performed by measuring approximately two hundred beam tracks in the following way:

A point which could be recognized in all three views as a corresponding point was found on the beam track. Then each beam track was measured before and after this point and the variables  $(\phi, \tan \lambda, 1/p)$

at the mid point of each part of the track were determined from the measurements.

A comparison was made of the 3 variables determined before and after the corresponding point after they had been swum to the corresponding point. Obviously they should be equal, but in the presence of measuring error their difference will be non-zero. However they should distribute about a mean value of zero with a standard deviation typical of the measuring precision provided that the swimming process is free of error and provided that reconstruction accuracy does not vary along the chamber.

The distributions are as expected and this shows that swimming and reconstruction are not the sources of the systematic shift seen in the stretches.

#### 4.7 Conclusion

Although it has not been possible to find the cause of the non-zero stretch in  $\tan \lambda$ , since tau-mesons and other fitted channels give good  $P(\chi^2)$  distributions it is felt that this value of stretch is not important and can be tolerated.

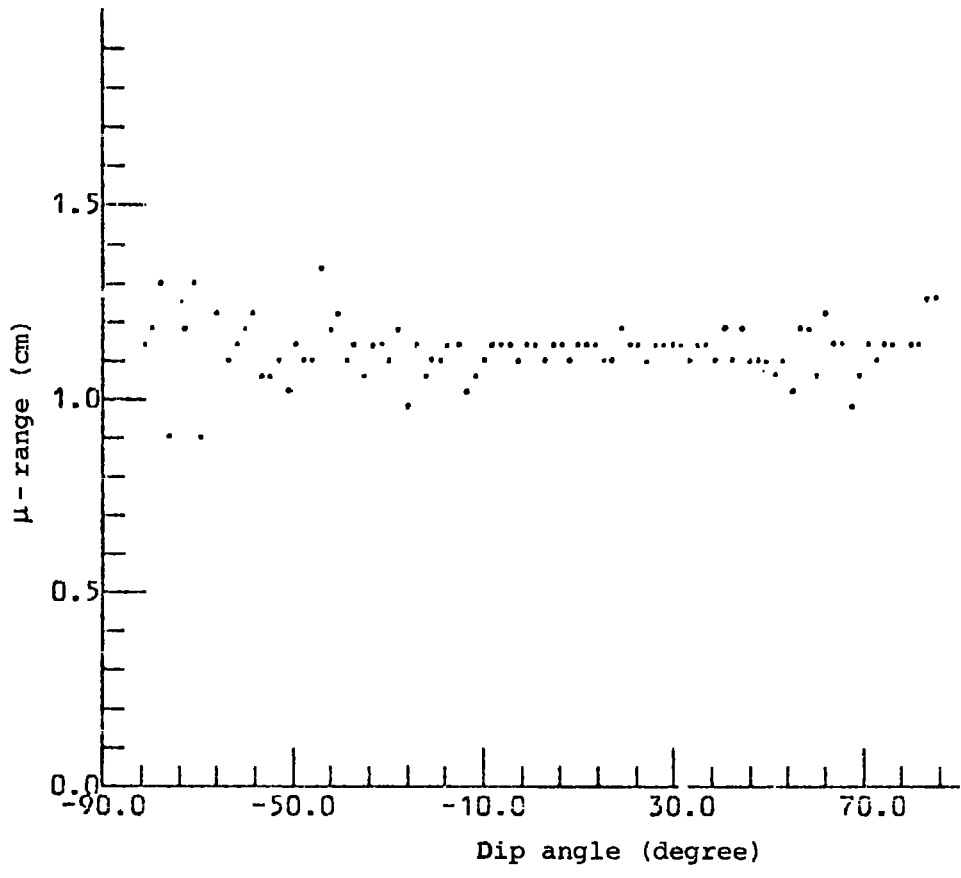


Figure 4.17:      Variation of muon range with  
dip angle

## CHAPTER 5

### EVENT SELECTION AND ABSOLUTE CROSS-SECTION

The overall aims of this experiment have been already described in chapter one. The specific aim of the work described in this thesis is the determination of the cross-section and differential cross-sections of kaons leading to neutral channels. In particular the following neutral channels have been examined.

$$\begin{aligned} (1) \quad & \bar{K}^0 \rightarrow \Lambda^0 \pi^0 \\ (2) \quad & \rightarrow \Sigma^0 \pi^0 \\ (3) \quad & \rightarrow \bar{K}^0 n \end{aligned} \tag{5.1}$$

Apart from some small contribution from the  $\Lambda^0 \pi^0 \pi^0$  channel these are the only channels. In this chapter the determination of the cross-sections is described. The details of the determination are complex and to help in the understanding of the process it is necessary to define the following terms which will be used frequently later.

(a) Point  $\Lambda^0/\bar{K}^0$  - fit This is a 3-constraint fit to 0-prong events with an associated  $V^0$ . In this fit two sets of information are used, one is the measured quantities of the charged decay tracks of the neutral particle and the other is the direction of the vee from the decay vertex to the interaction vertex.

(b)  $\Lambda^0$  - Channels These are 0-prong + vee reactions (with or without associated gamma rays) which have made atleast a 'point  $\Lambda^0$ -fit.' These events are dominated by  $\Lambda^0 \pi^0$  and  $\Sigma^0 \pi^0$  production.

(c) 3-body  $\Lambda^0$  Channels This is  $\Lambda^0 \pi^0 \pi^0$  production which makes a relatively small contribution to the  $\Lambda^0$ -channels.

$\bar{K}^0$  - Channels Events located in this category are those 0-prong + vee events which make a successful 4-constraint fit to the hypothesis  $K^- P \rightarrow \bar{K}^0 n$ .

### 5.1 Kinematical Fitting

For each event the Kinematic fits shown in Table 5.1 were attempted (see Table 3.1 for multi-vertex fits). The sequence followed is to make first a 'point  $\Lambda^0/\bar{K}^0$  - fit' for the decay process and then using the information obtained for  $\Lambda^0/\bar{K}^0$  from this first fit, make a fit to one of the two body processes  $\Lambda^0 \pi^0$ ,  $\Lambda^0 \gamma$  or  $\bar{K}^0 n$ . In the second fit three kinematic quantities for one of the final state particles  $\pi^0$ ,  $\gamma$  or the neutron are missing which makes the second fit a 1-constraint fit.

If the event fitted above had associated gamma rays, fits were tried with hypotheses including gamma rays. For example, if an event was recorded at scanning as  $\Lambda^0 + 1 \gamma$ , the following hypotheses were tried,

$$\begin{array}{lll}
 K^- P \rightarrow \Lambda^0 \gamma & , & \Lambda^0 \rightarrow \pi^- P & , & \gamma \rightarrow e^+ e^- \\
 \rightarrow \Lambda^0 \pi^0 & , & \Lambda^0 \rightarrow \pi^- P & , & \pi^0 \rightarrow \gamma (\rightarrow e^+ e^-) + \gamma (\text{unseen}) \\
 \rightarrow \Sigma^0 \pi^0 & , & \Sigma^0 \rightarrow \Lambda^0 \gamma (\rightarrow e^+ e^-) & , & \Lambda^0 \rightarrow \pi^- P \\
 \rightarrow \Lambda^0 \pi^0 & , & \Lambda^0 \rightarrow \pi^- P & , & \\
 \rightarrow \Lambda^0 \gamma (\text{unseen}) & , & \Lambda^0 \rightarrow \pi^- P & & 
 \end{array}$$

As it is shown in the above example, KINEMATICS attempted all the possible fits for each event using all the combination of the gamma rays and the lambda. It also tried appropriate fits using a missing gamma ray or a missing  $\pi^0$ . Because of these, ambiguity of fits can occur, most of which cannot be resolved at JUDGING.

Table 5.1: Kinematic fits attempted to  $\Lambda^0/\bar{K}^0$ -channels

Reaction	Description of Fit	No. of Constraints
1. $\Lambda^0 \rightarrow p \pi^-$	The origin of $\Lambda^0$ not assumed	1
2. $\bar{K}^0 \rightarrow \pi^+ \pi^-$	The origin of $\bar{K}^0$ not assumed	1
3. $\Lambda^0 \rightarrow p \pi^-$	$\Lambda^0$ was constrained to the $\bar{K}^-$ -vertex	3
4. $\bar{K}^0 \rightarrow \pi^+ \pi^-$	$\bar{K}^0$ was constrained to the $\bar{K}^-$ -vertex	3
5. $\bar{K}P \rightarrow \Lambda^0 \pi^0$	Input to this fit was the $\Lambda^0$ -momentum from fit 3	1
6. $\bar{K}P \rightarrow \Lambda^0 \gamma$ ( $\gamma$ is unseen)	Input to this fit was the $\Lambda^0$ -momentum from fit 3	1
7. $\bar{K}P \rightarrow \bar{K}^0 n$	Input to this fit was the $\bar{K}^0$ -momentum from fit 4	1

For the neutral channels without associated gamma rays, the only possible physical fitting channels are  $\Lambda^0\pi^0$ ,  $\Lambda^0\gamma$  and  $\bar{K}^0n$ . Almost all events giving  $\Lambda^0\pi^0$  fit also give  $\Lambda^0\gamma$  fit and about 28% give a  $\bar{K}^0n$  fit. The  $\Lambda^0/\bar{K}^0$  ambiguity was efficiently resolved at JUDGING and the final sample of events left  $\Lambda^0/\bar{K}^0$  ambiguous was less than 1% of the total.

## 5.2 Data Selection

In this section the arguments for imposing selection criteria in the data are presented.

(a) Z - Co-ordinate As described in Chapter 2, the first problem encountered with 0-prong events in this experiment was that a large number of them arose from beam tracks that had stopped in the perspex walls of the T.S.T. rather than the hydrogen of the chamber. For most of these spurious events the associated  $V^0$  did not give a 'point  $\Lambda^0/\bar{K}^0$  - fit' and the events were excluded from the data in JUDGING. However the distribution of the Z - co-ordinate of the production vertex of fitted events (Fig. 5.1) shows clearly that there are still some spurious events of this kind in the data summary tape (D.S.T.). These events are accumulated in the two spikes shown in Figure 5.1 at either end of the distribution. Therefore, to avoid contamination from these events a selection has to be made on the Z - co-ordinate. The selection made is:

$$19.4 \leq Z \leq 27.0 \text{ cms.}$$

Of the original number of events giving the fits to  $\Lambda^0/\bar{K}^0$  - channels (see Table 4.3), about 10% were removed from the data due to this selection.

(b) Primary momentum In Figure 5.2 the momentum distribution of the  $K^-$  - beam tracks at the production vertex for  $\Lambda^0$  - channels is shown. It can be seen there is a large spike at zero momentum and a peak at about

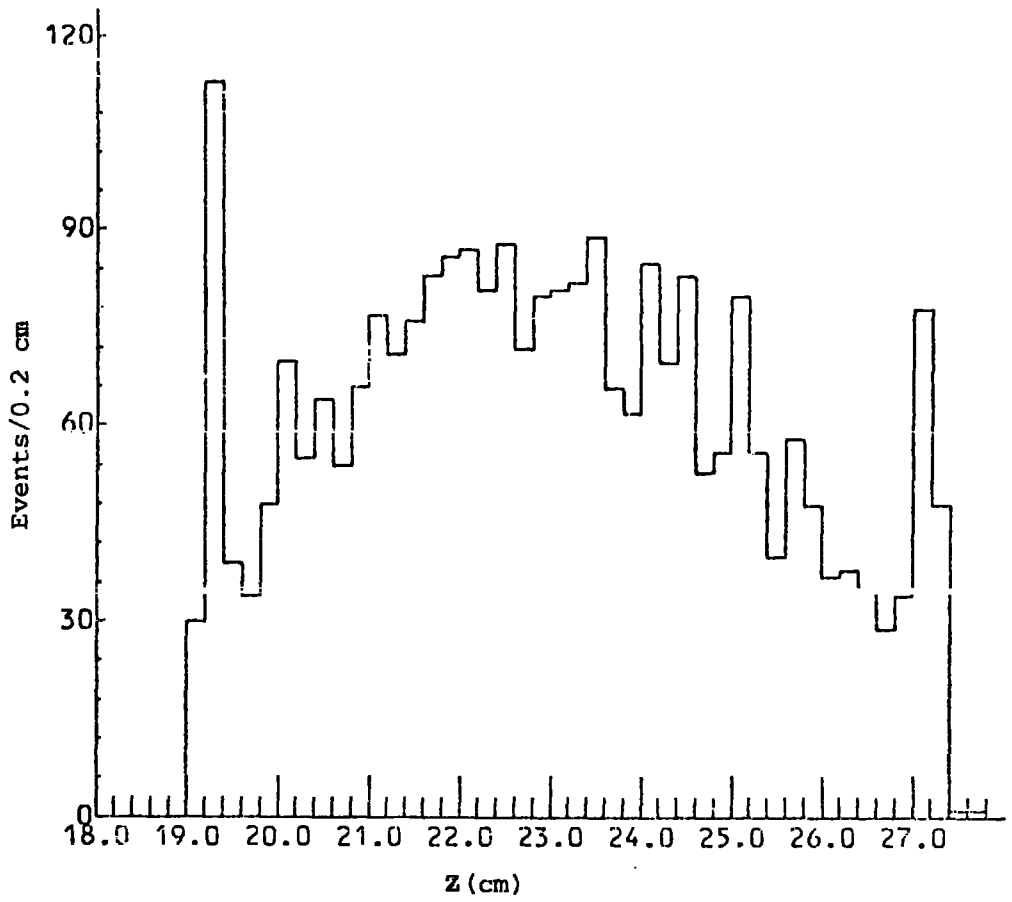


**Figure 5.1:** Z-coordinate distribution of primary vertex for  $\Lambda^0$ -events

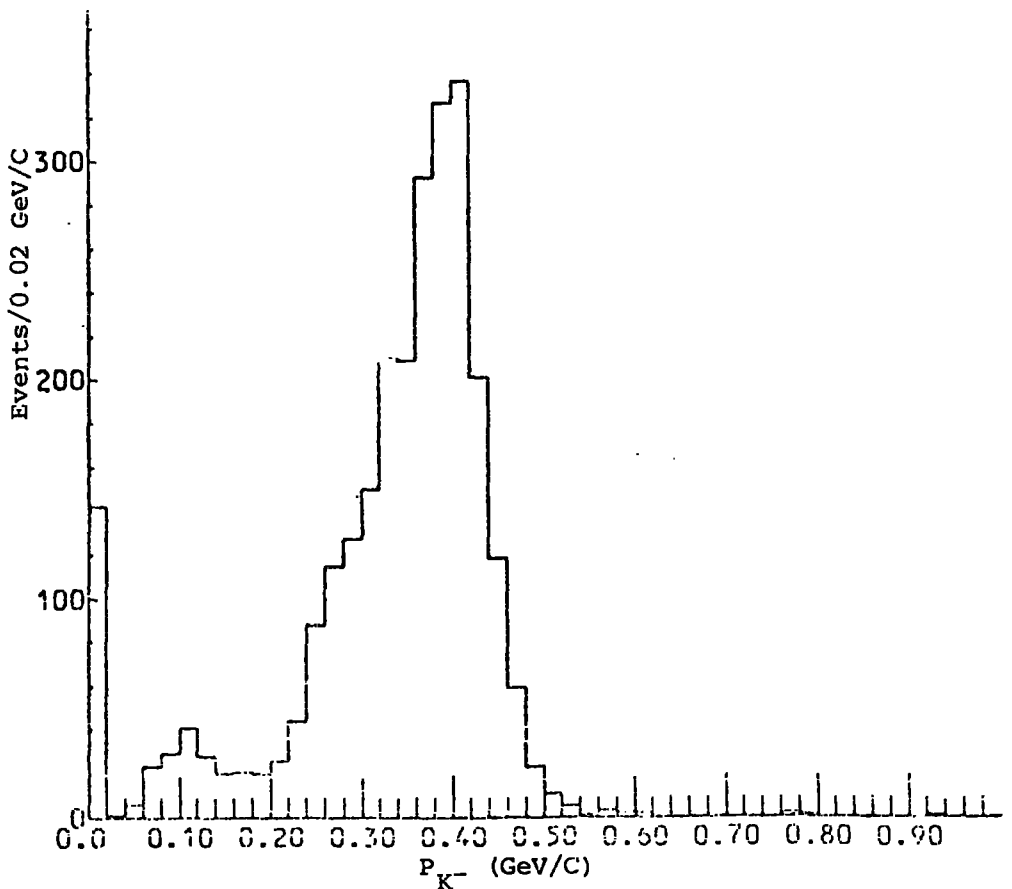


**Figure 5.2:** Primary momentum distribution for  $\Lambda^0$ -events



100 MeV/c. These events were predominantly due to interactions of  $K^-$  - mesons at rest. This is substantiated in Figure 5.3 where the distribution of primary momenta for events known to stop are shown. These momenta are for stopping events where a co-linear  $\Sigma$ -hyperon and pion are produced. Only the unfitted momentum is shown since this will correspond to the momentum of a  $\Lambda^0$  event. Because of errors of measurement it is impossible on an individual basis to distinguish between interactions at rest and in-flight below 120 MeV/c. Moreover, below 200 MeV/c, the number of events is small and hence for the  $\Lambda^0$ -channels, cross-sections have been evaluated for the momentum intervals above 200 MeV/c to the maximum momentum of about 500 MeV/c available in the experiment.

For the  $\bar{K}^0$  - channels although the threshold is 90 MeV/c, the number of events below 200 MeV/c  $K^-$  - momentum is however small. In Table 5.2 the number of events lost due to this selection is shown.

Table 5.2: Selection criteria imposed in the Durham data

Criterion	No. of Events Lost (%)		Remaining Events	
	$\Lambda^0$	$\bar{K}^0$	$\Lambda^0$	$\bar{K}^0$
Z - co-ordinate	10	10	2661	777
Primary Momentum	13.5	1.5	2302	765

(c)  $\chi^2$  - Probabilities The distribution of chi-square fit probability,  $P(\chi^2)$ , for 'point  $\Lambda^0$ -fit' for  $\Lambda^0$ -channels is shown in Figure 5.4 (the one for  $\bar{K}^0$  - channels is similar). This distribution is flat as expected apart from a large spike at very low probability. Comparing the distributions of various quantities (e.g.  $K^-$  or  $\Lambda^0$  momentum, etc.)

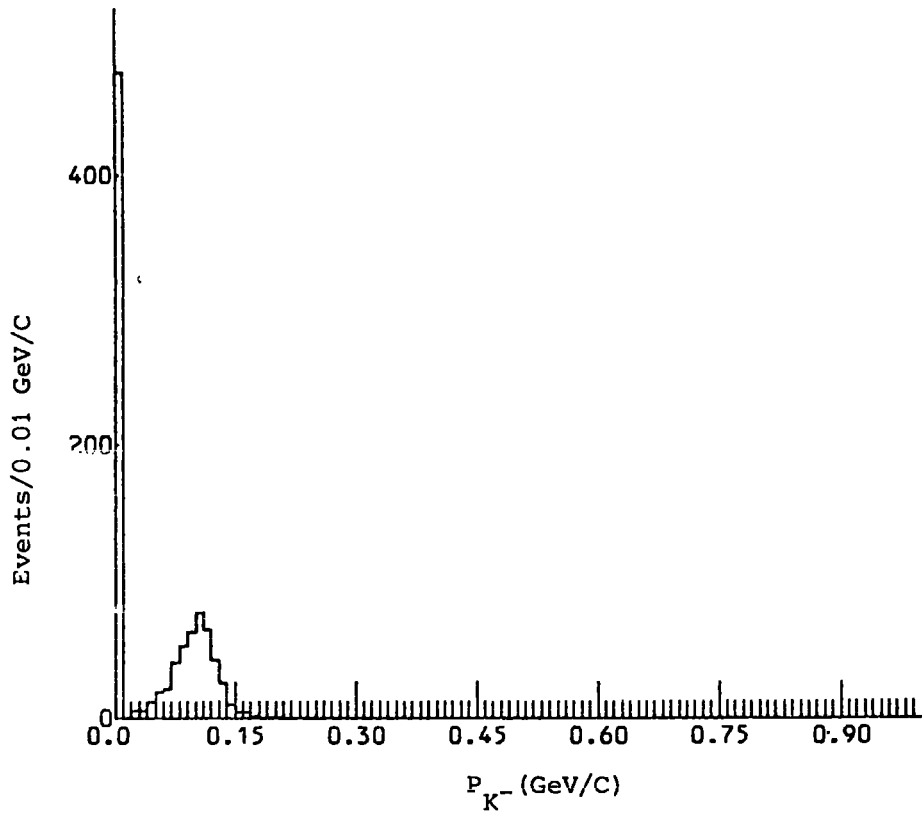


Figure 5.3: Primary momentum distribution for events at rest.

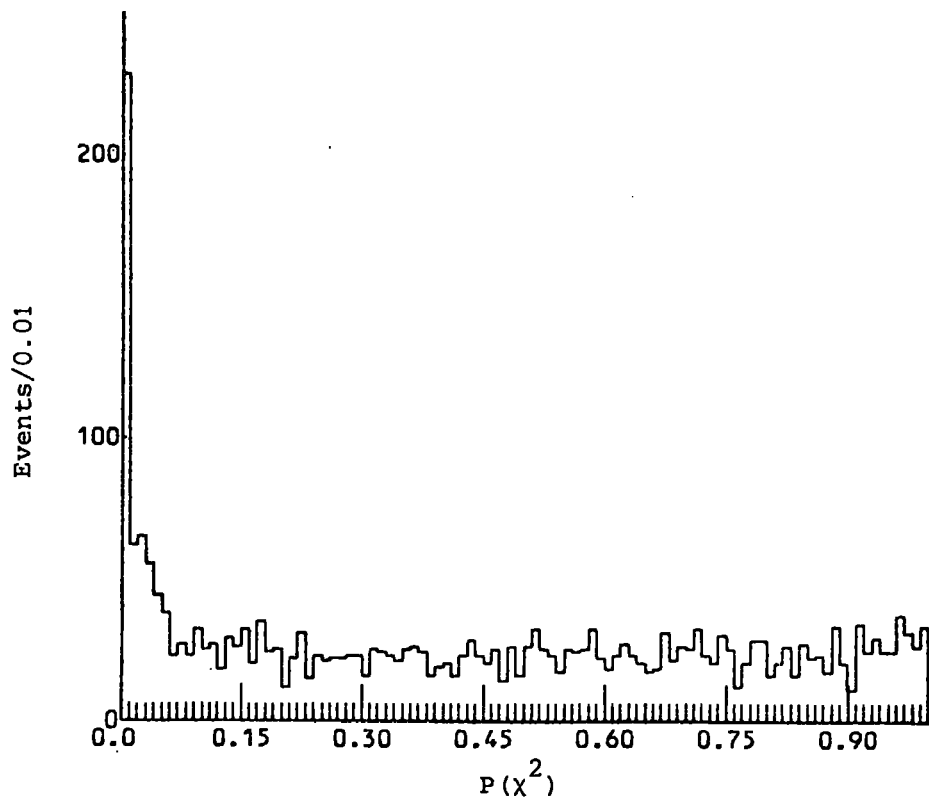


Figure 5.4:  $\chi^2$ -probability distribution for  $\Lambda^0$ -events

for these events with  $\chi^2$ -probability less than 0.01 with those having  $\chi^2$ -probability greater than 0.01 showed no significant differences. Bearing in mind that a low probability chance association of the  $\Lambda^0$  is the only alternative to accepting the 'point  $\Lambda^0$ -fit', no  $\chi^2$ -cut was imposed on the data, (see Section 5.5).

After the application of the selection criteria, the number of  $\Lambda^0$ 's used for the following analysis was 2302 with at least a 'point  $\Lambda^0$ -fit' and that of  $\bar{K}^0$ 's was 765 with a 4 G multi-vertex fit. For analyses that did not have to be normalized to give absolute cross-sections, the data available from the Birmingham sample was included to increase statistics. Before any such mixing of data it was checked that the two samples were compatible.

### 5.3 Determination of Tracklength from Tau-Mesons

In order to evaluate the cross-section as a function of momentum it is necessary to have the number of events corrected for any losses in each channel and the amount of beam track available per momentum interval. The determination of the latter is described first.

At the entrance to the fiducial volume there is a spectrum of  $\bar{K}$ -mesons with momentum P whose potential pathlength L is determined by the geometry of the fiducial volume. The number of  $\bar{K}$ -mesons with momentum P and potential length L in the ranges dP and dL is given by

$$N(L,P) dL dP$$

As the kaons pass down the chamber they are deflected in the magnetic field, lose energy through ionising collisions and:

(a) pass out of the fiducial volume which is the fate of most particles, or

(b) undergo decay and are recorded at scanning time, only if the decay is in the tau-mode, or

(c) undergo strong interaction which is also recorded at scanning time.

If the initial distribution  $N(L,P)$  is known then the momentum at any point on the subsequent tracks can be calculated by allowing for energy loss through range-energy tables. Consequently for given momentum bins, say in 20 MeV/c intervals, the amount of pathlength, which is traversed by the kaons in each momentum interval can be calculated. Finally, if the lifetime for decay and the cross-sections for strong interaction are known the number of decays and the number of strong interactions at each momentum can be determined. Conversely, in the practical case, if the number of strong interactions in each momentum interval is measured then the cross-sections for strong interaction as a function of momentum can be determined.

The problem is to find the initial distribution  $N(L,P)$ . Although the momentum spectrum is approximately known from the beam optics and energy loss in the degrader of aluminium, the distribution of potential pathlengths is diffused by the degrader and is virtually unknown initially.

### 5.3.1 Determination of $N(L,P)$

#### (a) Direct measurement of $N(L,P)$

Since the  $\bar{K}$ -mesons are clearly distinguished from the contaminating pions, muons and electrons then  $N(L,P)$  can be determined by direct measurement. This would involve measuring every  $\bar{K}$ -track in a large sample of frames covering the complete exposure. Presumably as many  $\bar{K}$ -tracks would need to be measured as there are strong interactions ( $\sim 30,000$ ) to balance the statistical accuracies. The arguments against this procedure are:-

(i) that 30,000 measurements would take up a considerable part of the measuring resources, and

(ii) that short tracks just after the entrance to the fiducial volume will be difficult to see and in all probability would fail in the measurement because of their short lengths and steepness. This might bias the distribution. Consequently it is not proposed that direct measurement should be employed.

(b) Determination of N(L,P) from tau-decays

All the  $\tau$ -mesons found during scanning have been measured. The measurement returns a momentum at the mid point of the track. By allowing for energy loss the potential path L of that decaying tau and its momentum P at the entrance to the fiducial volume can be found. When this is done for all the tau-decays the spectrum of lengths and momentum at the entrance is found to be

$$T(L,P) \, dL \, dP .$$

This distribution is related to N(L,P) through the probability of decay. If the momentum of the kaon at the point of decay is p, then its decay length at that point is

$$\lambda_d = \gamma \beta c \tau = p \frac{c \tau}{m}$$

where  $\tau$  and  $m$  are the lifetime and mass of the kaon and  $\beta c$  and  $\gamma$  are the velocity and dilation factor of the kaon. The probability of the Kaon decaying anywhere (at length  $\ell$ ) along its potential path L is

$$\int_0^L \frac{d\ell}{\lambda_d} = \int_0^L \frac{m d\ell}{c \tau p} \tag{5.2}$$

That this decay is by the tau-mode is given by the branching ratio B ( $\sim 5\%$ ). Consequently when a kaon is seen to decay by the tau-mode the

inverse probability, or weighting factor, gives the initial number of kaons which have yielded this seen tau-decay. Hence

$$N(L,P) dL dP = W(L,P) T(L,P) dL dP$$

where the weight

$$W(L,P) = 1 / \left( B \int_0^L \frac{m d\ell}{c\tau p} \right) \quad (5.3)$$

Strictly speaking this weight should include the strong interactions. Although in our calculation this has been taken into account (see Appendix B), the cross-sections are not well known. In any case the neglect of the strong interactions will make a difference of about 2-3% to the total distribution which is well within the error of the experiment. In practice the weight is evaluated numerically using range-momentum tables to relate  $p$  and  $\ell$ . However, to illustrate the size of  $W$  the expression can be evaluated analytically assuming that range is related to momentum as

$$R = a p^b$$

where  $b = 3.6$  and  $a$  is mass dependent. Then

$$N(L,P) = T(L,P) \frac{c\tau}{Bm} \left[ 1 - \left[ \frac{R-L}{R} \right]^{\frac{b-1}{b}} \right]^{-1} \frac{b-1}{ab} p^{1-b} \quad (5.4)$$

The weighting factors for a variety of entrance momenta and potential lengths are shown in Table 5.3; the weights are quite large.

The drawback of this method is the lack of statistics implied by the low value of the branching ratio  $B$  into tau-decay. This is highlighted in a comparison of decay and interaction lengths. The total strong interaction cross-section behaves approximately as  $1/p$  and gives an interaction length (in cm.) of

$$\lambda_i \sim 780 p \quad (p \text{ in GeV}/c)$$

Table 5.3: Some Weighting factors for tau-mesons

$P_{K^-} \left( \frac{\text{MeV}}{c} \right)$	Average $K^-$ -Potential length (cm.)*	B x Weight
210	45.02	4.11
230	46.68	4.28
250	45.43	4.76
270	44.39	5.39
290	46.44	5.36
310	46.80	6.12
320	47.36	6.49
350	48.93	7.29
370	51.71	6.48
390	52.64	7.45
410	54.39	6.77
430	55.79	7.12
450	51.17	8.77
470	53.74	10.02
490	60.46	6.71

\* These are the observed average potential lengths for tau-mesons in the experiment.

The decay length is given precisely by

$$\lambda_d = 751 p$$

So to good approximation the total numbers of kaon decays and strong interactions will be equal. However only 5% of the decays will be by the tau-mode and even after allowing for unseen modes of strong interactions the number of tau-decays will be less than 1/10 of the strong interactions. Allowing for unseen modes of strong interaction, then for individual partial cross-sections the number of tau-decays will be approximately equal to the number of strong interactions, in statistical balance. Consequently the precision of the experiment relies quite heavily on the number of  $\tau$ -decays.

Each tau-decay has been measured and from the momentum at the decay vertex the initial momentum  $P$  has been calculated together with the potential pathlength  $L$ . The latter has been determined by projecting the kaon trajectory backwards to the entrance to the fiducial volume and producing it forwards to the exit from the volume. The momentum distribution of the beam tracks at the entrance to the fiducial volume is shown in Figure 5.5. At any point  $x, y, z$  along the path the length is changed by  $\Delta x$  (typically 1 mm) and from the momentum at that point  $\Delta y, \Delta z, \Delta p, \Delta \phi$  and  $\Delta L$  are calculated to give the new space coordinate, momentum, azimuth angle and length of the kaon track. The process is continued until one of  $x, y$  or  $z$  is found to be outside the fiducial volume.

This is followed by numeric integration to give the weighting factor for the tau-meson. Although the considerations above have been made in terms of  $N(L,P)$ , in fact this distribution is never formally established. Instead the final part of the calculation is entered and the weighted tau-decay is distributed into momentum bins of, usually 20 MeV/c wide starting from zero momentum to build the final result, that is, the available pathlength as a function of momentum.



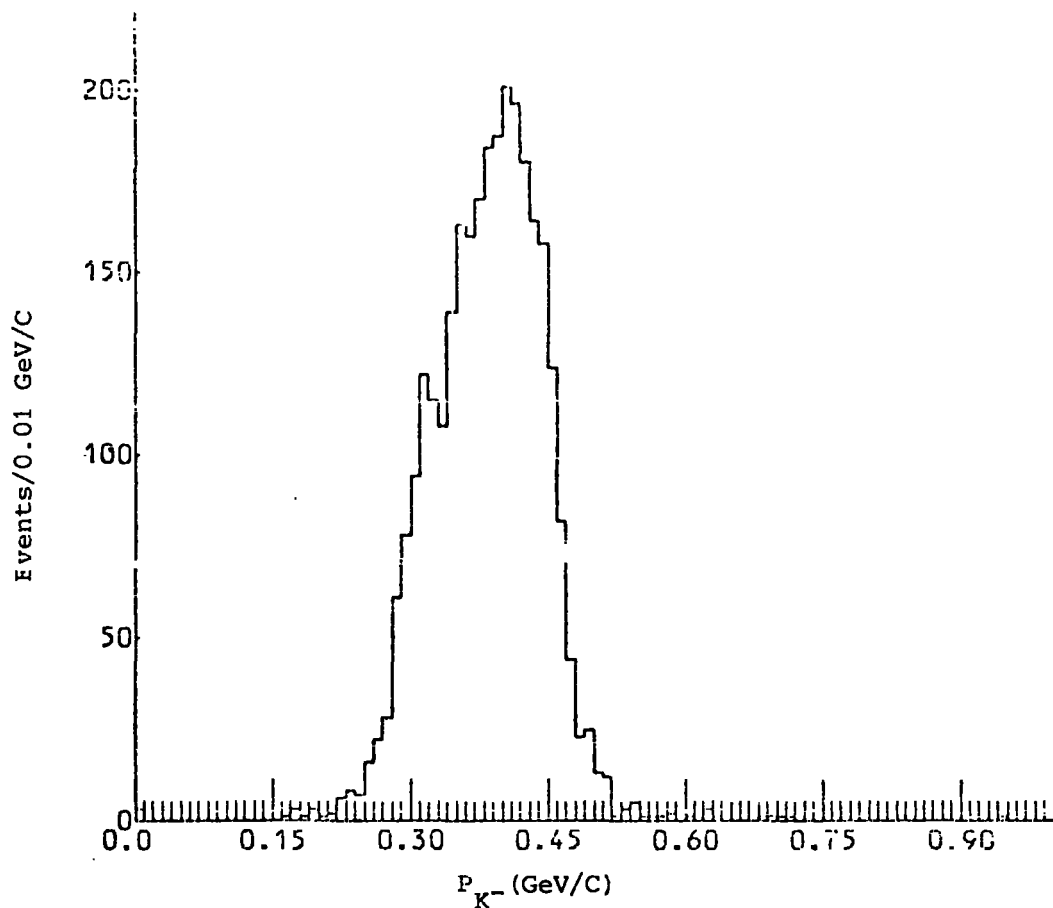


Figure 5.5: Primary momentum distribution at entrance to the fiducial volume

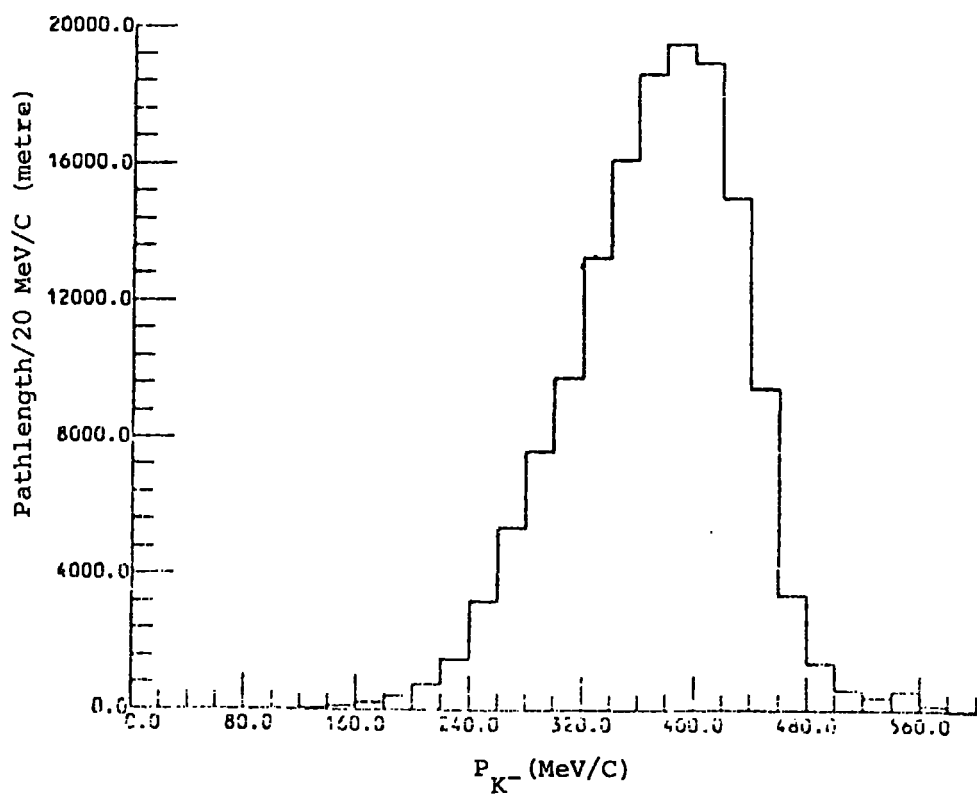


Figure 5.6: Pathlength distribution as a function of incident momentum.

This is achieved by comparing the track in the fiducial volume with its full range. Beginning from the end of the range, the track is divided into lengths corresponding to 20 MeV/c intervals, as shown in Figure 5.7.

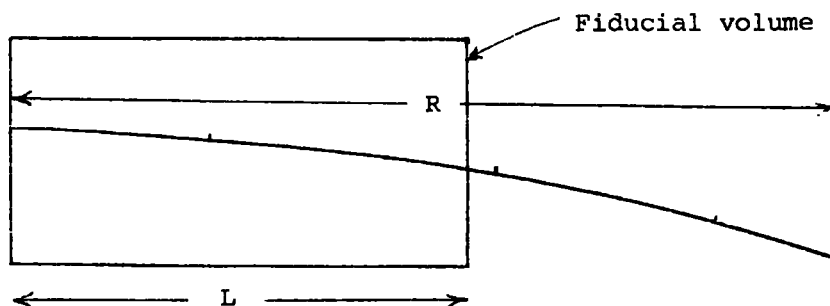


Figure 5.7

For those intervals lying completely in the fiducial volume the full weight of the tau-decay is added into the track-length distribution. For those intervals lying across the entrance and exit to the fiducial volume the appropriate proportion of the weighted tau-decay is added. Attenuation of the beam along its path has been allowed for (see Appendix B). In this way the pathlength available for interaction as a function of momentum interval is determined experimentally (Fig. 5.6). The distribution needs to be examined for losses. The overall efficiency after two scans for tau-decays is quite high at 98% and the distribution above should be scaled appropriately for scanning losses (corrections for losses arising from events which could not be measured or failed measurement  $\sim 5\%$  can also be made by simple scaling). However this approach may be too simplified since,

- (a) scanning losses may be highest at the entrance region of the fiducial volume where there is a concentration of tracks emerging from the degrader, and
- (b) the measurement of the tau-decay may not be possible or may fail because of lack of visibility in this same region.

In principle this is easily checked by examining the variation in frequency of occurrence of decay as a function of tracklength in the chamber. From above there would be a loss of short length primaries to tau-decays. Unfortunately any such variation is completely masked by the distribution of potential lengths. (The distribution from the above analysis which may be suffering from the losses we are trying to estimate is shown in Figure 5.8). Instead an analysis has been devised to remove the masking effects of the distribution of pathlengths. It can be shown that the tau-decays for kaons defined by P and L will be distributed as a function of  $\ell (< L)$  as (see Appendix C)

$$v(\ell) = B \left[ \Sigma(vW) \right] \exp \left[ -K R^{1-1/b} \right] K'(R-\ell)^{-1/b} \exp \left[ K(R-\ell)^{1-1/b} \right] \quad (5.5)$$

where  $R = ap^b$ ,  $K = \frac{mb}{ct(b-1)}$  and  $K' = (1-1/b)K$ . Consequently a useful test is to check

$$\log \left[ \frac{v(R-\ell)^{1/b}}{\Sigma(vW)} \right] = \text{constant} + K(R-\ell)^{1-1/b}$$

for each group of potential length L, L + ΔL. Numbers are low and instead all values of L for a given p need to be used. Then

$$\frac{1}{N} \Sigma_L \log \left[ \frac{v(R-\ell)^{1/b}}{\Sigma(vW)} \right] = \text{constant} + K(R-\ell)^{1-1/b} \quad (5.6)$$

where N is the number of contributing L bins. The data should fall on a straight line of slope K (which is the lifetime essentially) and losses, if any, should also show by discrepancies at small values of  $\ell$ .

A check has been carried out for p in the range of 380 - 400 MeV/c where statistics are at a maximum and the result is shown in Figure 5.9

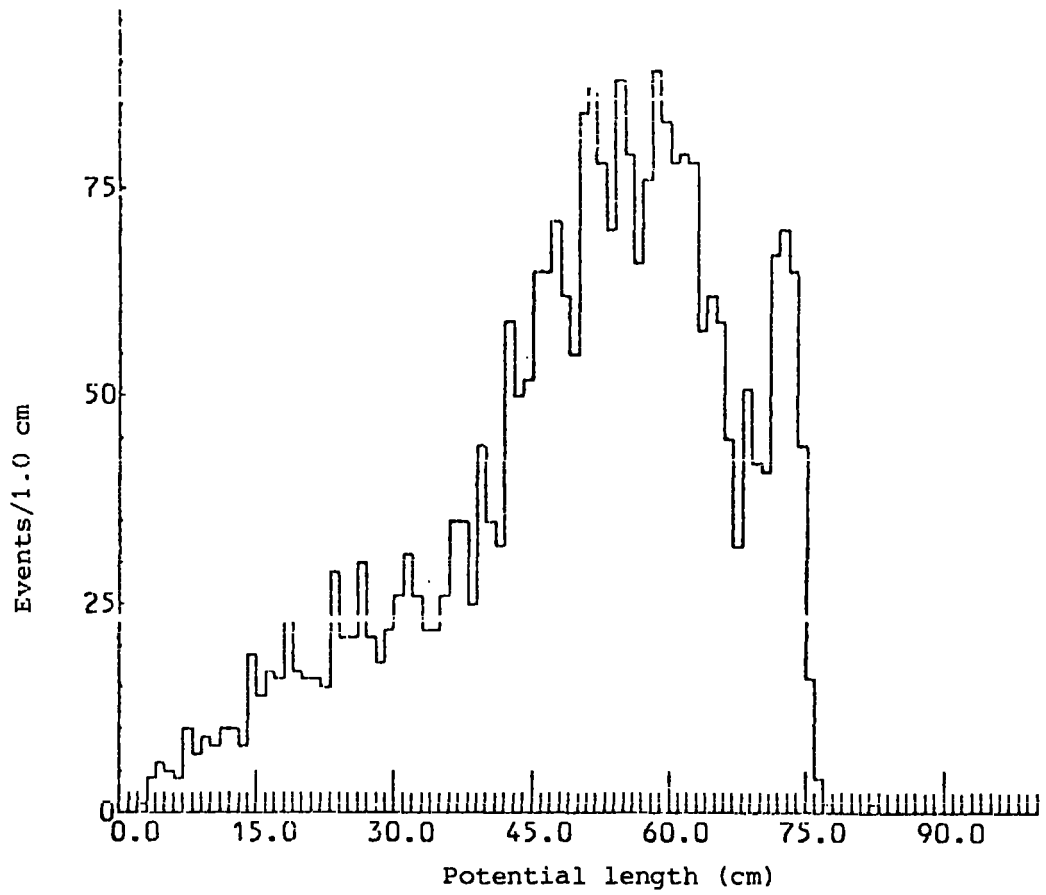


Figure 5.8: Potential length distribution of the beam

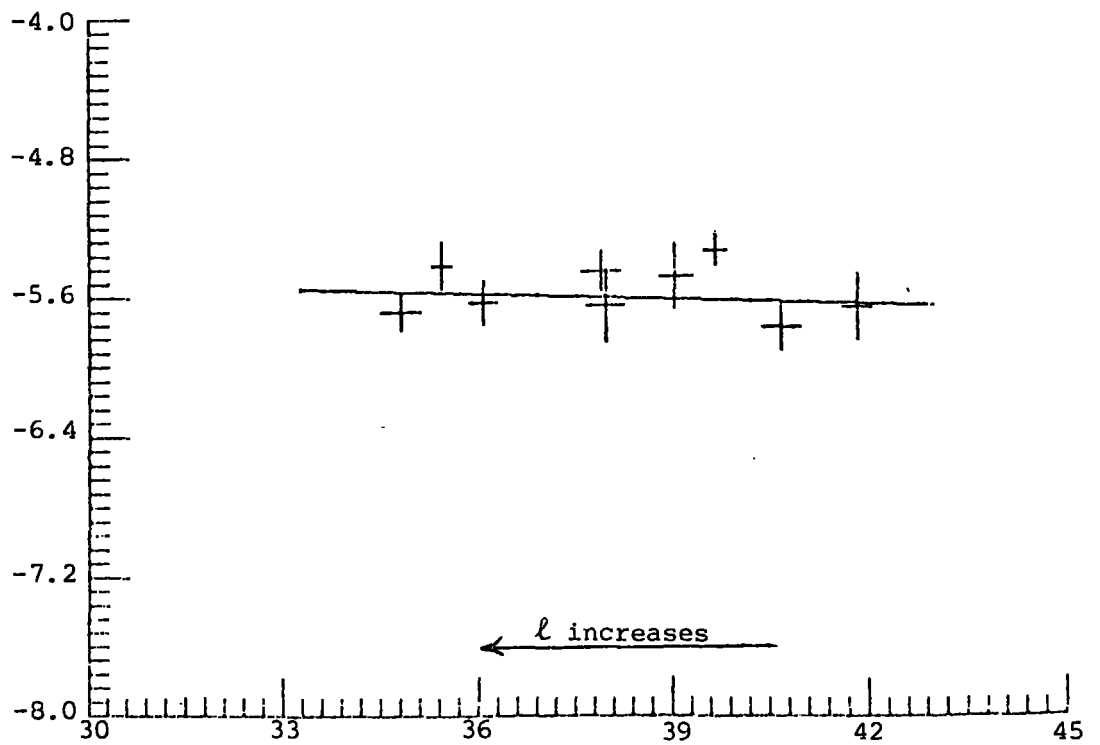


Figure 5.9: Check for losses of  $\tau$ -mesons. Definition of axes are given in equation 5.6.

The slope of the line is that expected from the lifetime for tau-decay. There is no significant loss at small values of  $\ell$ , consequently it may be concluded that corrections for scanning losses and 'not measurable' tau-decays may be made uniformly to the whole distribution.

#### 5.4 Unbiased Acceptance of Events

It is important to define an acceptance of events such that the fraction of the total production selected is known, hence enabling corrections to be made for biases in the observations. This is a significant operation in the present experiment since the shallow depth of the hydrogen target introduces substantial biases. Events may be lost because:

- (a) the neutral particle decays outside the T.S.T. chamber.
- (b) the neutral particle decays close to the production vertex and transforms the event into a 2-prong category.
- (c) the tracks comprising the  $V^0$  appear to be superimposed on the scanning table since the decay plane is nearly vertical.
- (d)  $V^0$ 's produced with small or large opening angles appear to be single tracks and are not recognized.
- (e) the proton or pion from the decay is too short to be seen.

To make sure that these losses are compensated for, geometric selections were made so that the events that remained showed no evidence of bias.

Since the characteristics of  $\bar{K}^0$ 's and  $\Lambda^0$ 's are different, firstly because the  $\bar{K}^0$ 's lifetime is almost  $1/3$  of that of  $\Lambda^0$ 's, and secondly because the decay products of a  $\bar{K}^0$  make almost always a large angle (opening angle), the  $\Lambda^0$ -channels and  $\bar{K}^0$ -channels are studied separately.

### 5.5 Selection of Unbiased $\Lambda^0$ 's Sample

For this purpose, all  $\Lambda^0$ -channels with a confidence level for the fit greater than  $10^{-3}$  were selected and the following cuts applied:

Length Cuts When a  $\Lambda^0$  decays near the vicinity of the production vertex so that the gap between the production and the decay vertices cannot be seen at scanning, it simulates a two-prong event. In such a case it is very difficult to distinguish the event from one produced in the reaction  $K^-P \rightarrow \pi^- \Sigma^+$  followed by  $\Sigma^+ \rightarrow \pi^0 P$  in which the decaying  $\Sigma^+$  is too short to be seen. A selection on minimum length or an equivalently minimum proper time will obviously remove this problem. The distribution of proper times for the  $\Lambda^0$  is shown in Figure 5.10. Here the proper time  $t$  is related to the observed length  $\ell$  as

$$\ell = \beta c \gamma t = \frac{P_{\Lambda^0}}{M_{\Lambda^0}} t c \quad (5.7)$$

The line drawn to the distribution corresponds to the known lifetime for  $\Lambda^0$ 's ( $\tau_{\Lambda^0} = 2.578 \times 10^{-10}$  sec.).

It is obvious from the distribution that there is a loss below  $t = 0.1 \times 10^{-10}$  second and therefore the minimum proper time,  $t_{\min}$ , was set to  $0.1 \times 10^{-10}$  second.

Angle Cuts Events lost through angular effects are mainly those in which the angle between the decay products of the  $\Lambda^0$  is small and the plane of decay is near normal to the front glass of the chamber. In order to estimate the loss in this case, an examination is made of the distribution of an azimuthal angle  $\phi$  around the direction of the  $\Lambda^0$  which is defined as follows:

$$\cos \phi = \left| \frac{(\hat{U} \times \hat{N}) \cdot (\hat{N} \times \hat{D})}{|\hat{U} \times \hat{N}| |\hat{N} \times \hat{D}|} \right| \quad (5.8)$$

where  $\hat{U}$  is the unit vector normal to the front glass,  $\hat{N}$  the direction of

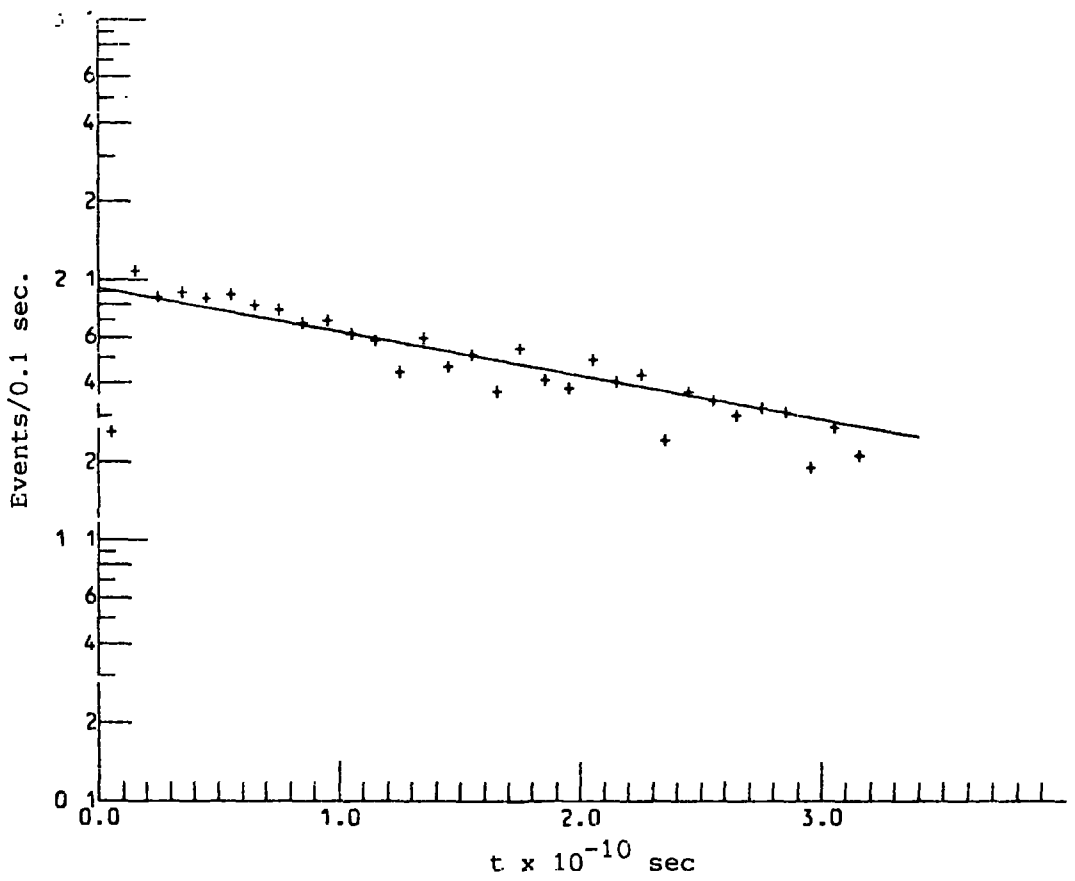


Figure 5.10: Distribution of  $\Lambda^0$ -lifetimes

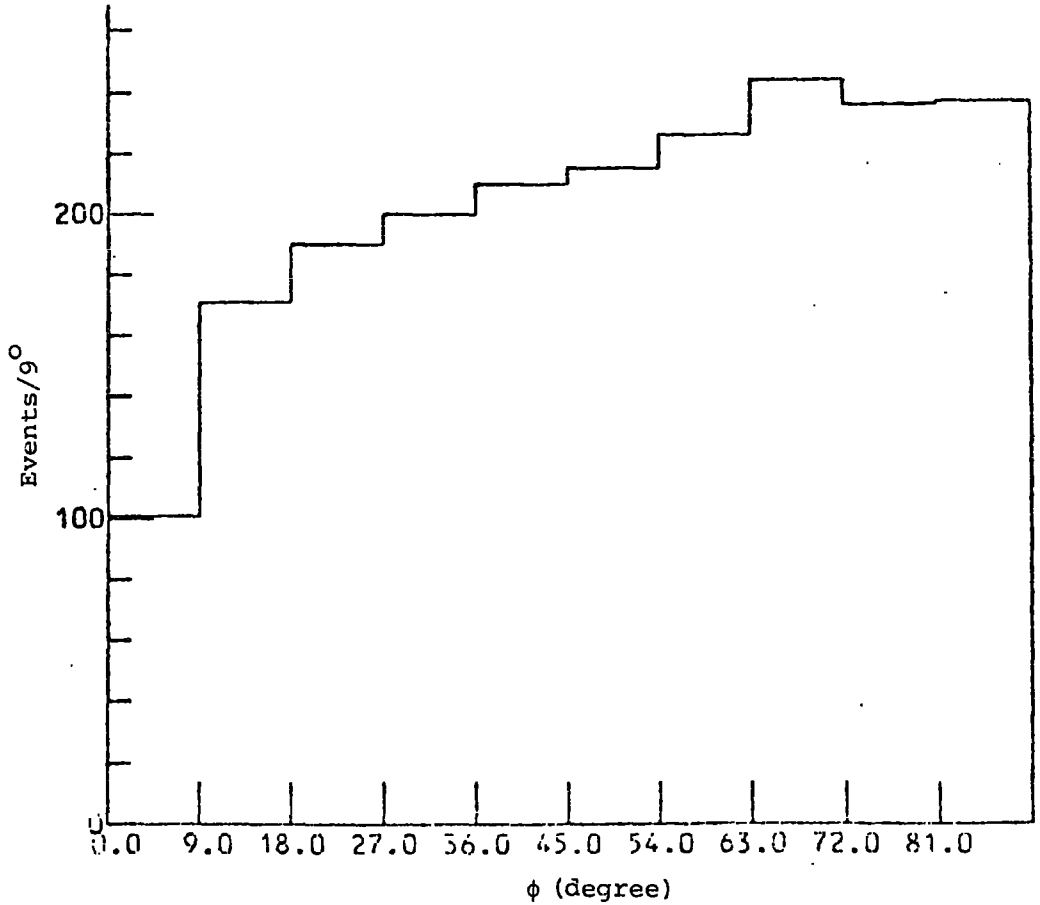


Figure 5.11:  $\phi$ -distribution for  $\Lambda^0$ -events

the  $\Lambda^0$  and  $\hat{D}$  the direction of the decay proton. This is the angle between the normal to the decay plane of the  $\Lambda^0$  and an arbitrary direction in the  $xy$  plane of the chamber. Since there is no correlation whatsoever between the decay normal of the physical event and the geometry of the coordinate system this distribution of  $\phi$  should be isotropic. It is shown in Figure 5.11 isotropy is present at large values of  $\phi$  but losses are clear at smaller values. It should be noted that  $\phi = 0^\circ$  corresponds to the decay plane of the  $\Lambda^0$  being vertical in the chamber and it is obvious that this type of event will be difficult to detect.

Bearing in mind that the T.S.T. is a shallow target ( $\sim 8$  cm. depth), it is expected that  $\Lambda^0$ 's decay outside the walls of the T.S.T. Hence the cone of production of the  $\Lambda^0$  will be distorted. Following this a means was devised to select  $\Lambda^0$ 's which were produced in a full cone inside the T.S.T. It is described below.

The kinematics of production of the two body process  $K^-_p \rightarrow \Lambda^0 \pi^0$  shown in Figures 5.12(a to c) for two different  $K^-$ -momenta (200 and 500 MeV/C) will illuminate the problem concerned with the shallow target. Let us first define the quantities involved in these figures.

(i)  $(\hat{K} \cdot \hat{\Lambda})_{LCM}$  is the cosine of the angle between the primary beam direction and the  $\Lambda^0$  direction both evaluated in the overall centre of mass system.

(ii)  $(\hat{K} \cdot \hat{\Lambda})_{LAB}$  is the cosine of the angle between the  $K^-$  and the  $\Lambda^0$  direction in the *laboratory* frame of reference.

(iii)  $(P_\Lambda)_{LAB}$  is the momentum of the lambda in the *laboratory* frame of reference.

(iv)  $D_0$  is the distance the production vertex had to be from the perspex walls of the T.S.T. in order to allow for the decay of the lambda particle



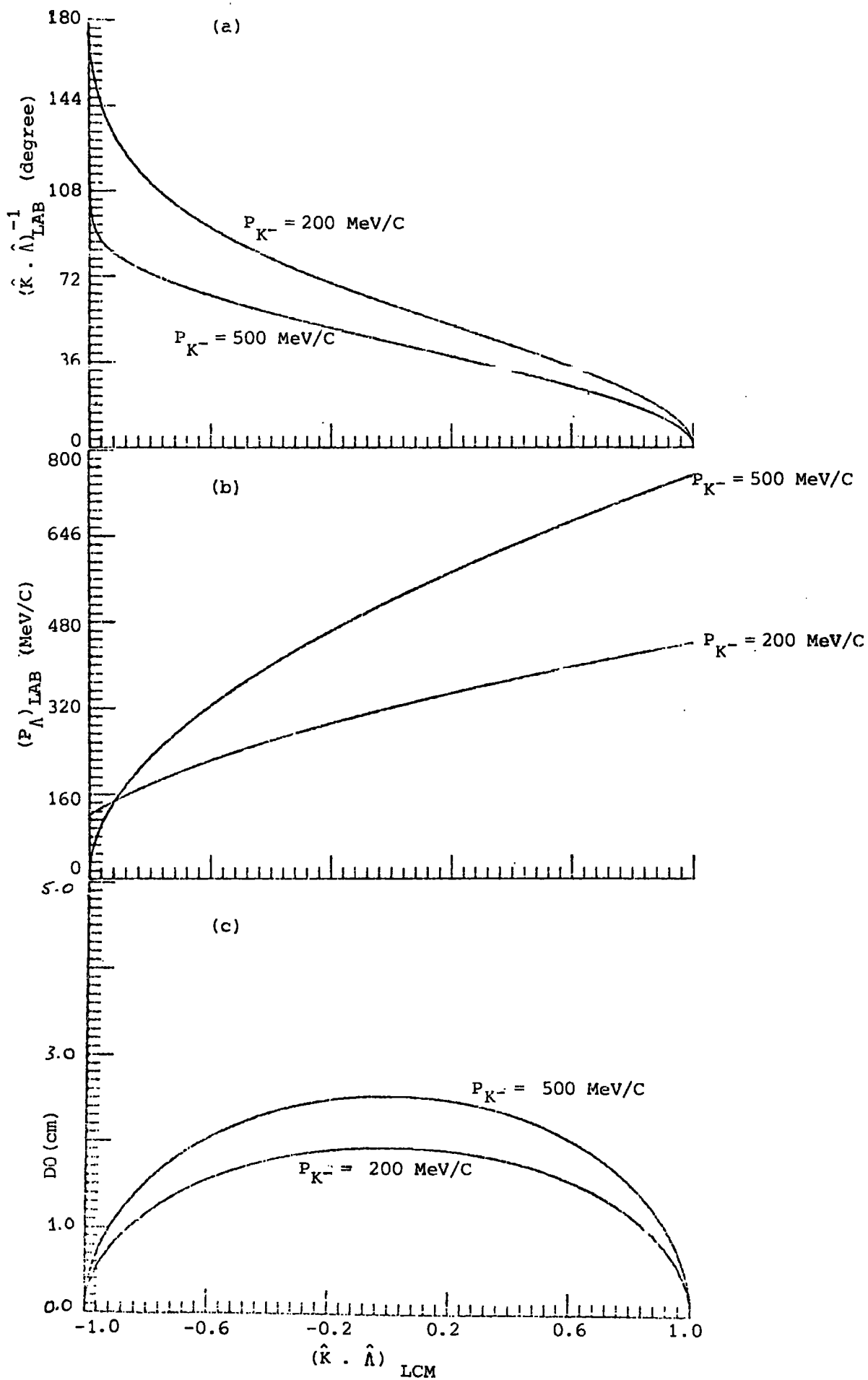


Figure 5.12: Kinematics of  $\Lambda^0 \pi^0$  production.

within one lifetime.

It must be pointed out that for the  $\Sigma^0$  hyperons which are also present in the data, the mass difference between  $\Sigma^0$  and  $\Lambda^0$  is small so that the  $\Lambda^0$  nearly follows the  $\Sigma^0$  direction (maximum angle of  $\Lambda^0$  from  $\Sigma^0$  is  $\sim 10^\circ$ ) and hence Figures 5.12 are adequate as a guide.

As it can be seen from Figure 5.12c, the maximum value of  $D_0$  varies from 2.56 cm at 500 MeV/c to 1.96 cm at 200 MeV/c  $\bar{K}$ -momentum. This means that the acceptance of the target in order to have a full cone of production for the  $\Lambda$ -hyperon depends on both the cosine of the production angle of the  $\Lambda$ -hyperon and the  $\bar{K}$ -momentum. So, the  $\Lambda$  particles were divided into four groups with  $\bar{K}$ -momenta of 200-320, 320-370, 370-410 and 410-500 MeV/c. These intervals were chosen such that each consisted of an adequate number of events and also one of the intervals had the known  $\Lambda$  (1520) resonance centred in it. Obviously one would like to collect data in narrower bins (e.g. 20 MeV/c), but with the present data available for this analysis it was not possible.

In order to have a high acceptance which is known without distorting angular distributions, the limiting value of  $D_0$  for the upper end of one of the momentum intervals was used to divide the depth of the T.S.T. into six regions as shown in Table 5.4. In the same table the lifetime intervals for the full cone of production are also shown.

For the first and last of the six depth regions the half cone of production can be accepted by taking  $\Lambda$ -hyperons produced upwards or downwards in the target. For example, events produced in region 1 can be accepted only if the  $\Lambda^0$  hyperon is directed downwards (a half cone of production) and this is true for all lifetime intervals. To events produced in region 3 the full cone of production is available for those with 0 to one lifetime for all  $\Lambda^0$  directions, but for those decaying within on

Table 5.4: The details of selected  $\Lambda^0$ 's

Region	Depth (cm.)	0 - .5 $\tau$	.5 - 1 $\tau$	1 $\tau$ - $t_{lim}$
1	.5 D0	62 H	30 H	20 H
2	.5 D0	157 $\bar{F}$	54 $\bar{H}$	28 $\bar{H}$
3	*3.8 - D0	220 F	158 F	55 H
4	3.8 - D0	225 F	166 F	58 H
5	.5 D0	194 F	57 H	37 H
6	.5 D0	79 H	41 H	34 H

\* The full depth of the fiducial volume is 7.6 cm.

F  $\equiv$  Full Cone

H  $\equiv$  Half Cone

lifetime to  $t_{lim}$  only a half cone of production to those directed downwards is available.  $t_{lim}$  is the limiting lifetime up to which a  $\Lambda^0$ -hyperon can be produced in a half cone of production. In calculating  $t_{lim}$  for each momentum interval the upper end of that momentum interval was used and it was assumed that the maximum length available to a  $\Lambda^0$ -decay was 3.8 cm. (half of the T.S.T. depth). The number of selected events in each region for a particular lifetime interval is shown in Table 5.4.

Although about 27% of the events are lost by using the above acceptance geometry for the target we can be confident that the remaining events (selected events) were unbiased as far as the shallowness of the target was concerned. Of course this loss was corrected for finally by doubling the number of events produced in a half cone of production.

The  $\phi$ -distribution for the selected events is shown in Figure 5.13. As can be seen it is now flatter than the one plotted for unselected events in Figure 5.11.

Looking at Figure 5.12b makes it clear that  $\Lambda^0$ -hyperons produced backwards in the overall centre of mass system by higher momentum beam particles can have very low momenta ( $\sim 100$  MeV/c) in the laboratory frame of reference. From Figure 5.12a these  $\Lambda^0$ -hyperons can be produced in the laboratory system at angles close to  $180^\circ$ . As might be expected these events are the most difficult ones to measure and fit kinematically. In other words, it is very unlikely to find these events on the D.S.T. Further, as was mentioned earlier in this chapter, the  $\Lambda^0$ -hyperons with very low momentum will have such a short pathlength to decay that they will simulate 2-prong events. Therefore, there must be a correction for loss of low momenta.

In order to find at what momentum the loss becomes significant, a scatter plot of the  $\Lambda^0$ -momentum versus the  $\phi$ -angle was obtained which is

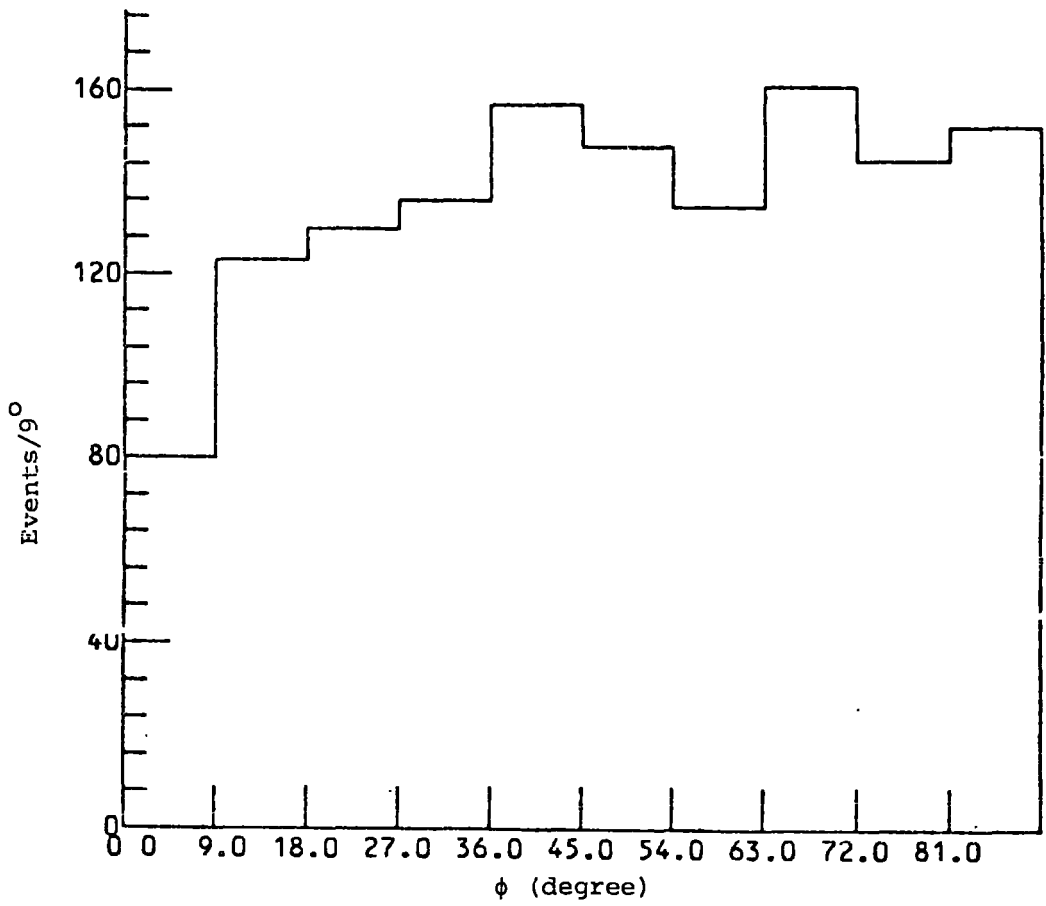


Figure 5.13:  $\phi$ -distribution for selected  $\Lambda^0$ -events.

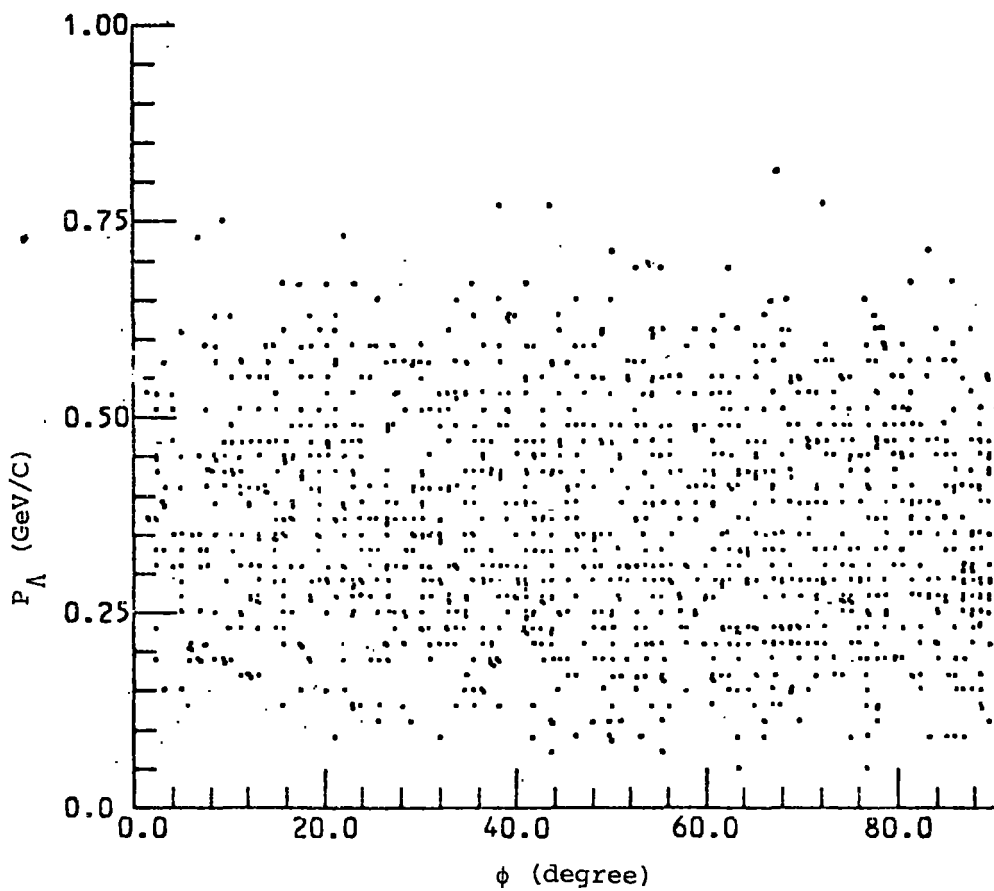


Figure 5.14:  $\Lambda^0$ -momentum versus  $\phi$ -angle

shown in Figure 5.14. From this plot the ratio of the number of events with  $\phi > 45^\circ$  to those with  $\phi < 45^\circ$  was calculated for each 20 MeV/c lambda momentum interval. It was found that this ratio was constant for  $\Lambda^0$ -hyperon with momentum greater than 160 MeV/c.

A further loss of  $\Lambda^0$ -hyperons is expected due to those with wide opening angles. To check this a plot of the  $\Lambda^0$  decay angular distribution for  $\Lambda^0$ - hyperons with  $\phi > 9^\circ$  and  $(P_\Lambda)_{LAB} > 160$  MeV/c was obtained. In this plot (Fig. 5.15),  $(\hat{P} \cdot \hat{\Lambda})_{CM}$  is the cosine of the angle between the proton and  $\Lambda^0$  line of flight in the rest frame of  $\Lambda^0$ . There is some loss at large decay angles. To eliminate this loss all events with  $(\hat{P} \cdot \hat{\Lambda})_{CM} > 0.8$  were removed from the data.

The  $\phi$ -distribution for all the events which had passed all the above selections with  $(P_\Lambda)_{LAB} > 160$  MeV/c is shown in Figure 5.16. As can be seen it is now reasonably flat for  $\phi > 9^\circ$ .

As a check on the purity of the sample remaining for determination of the cross-section, the lifetime distribution of the remaining events were plotted on a logarithmic scale and a straight line was fitted to the points (Fig. 5.17). The slope of this line determined the mean lifetime for  $\Lambda^0$ 's to be  $2.475 \pm 0.169$  which is consistent within the error with the world average.

## 5.6 Correction factors

With well defined selections as above it is then straightforward to make corrections to the events surviving the selection to determine the total number of produced events. The corrections made and the correction factors by which the remaining events were scaled are as follows:

- (1) for the neutral mode of decay,  $\Lambda^0 \rightarrow n \pi^0$  which has a branching ratio of  $\sim 35.8 \pm .5\%$ , the correction factor is 1.557.

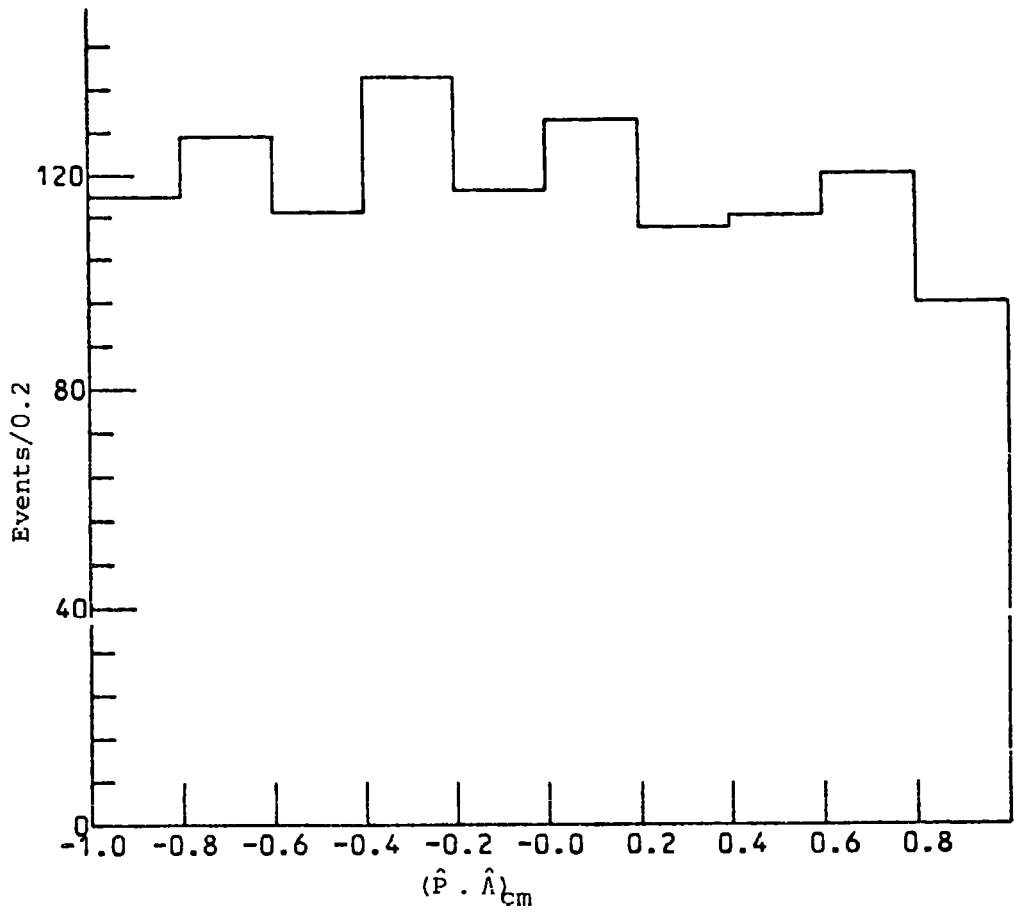


Figure 5.15: Decay angular distribution of  $\Lambda^0$ -events

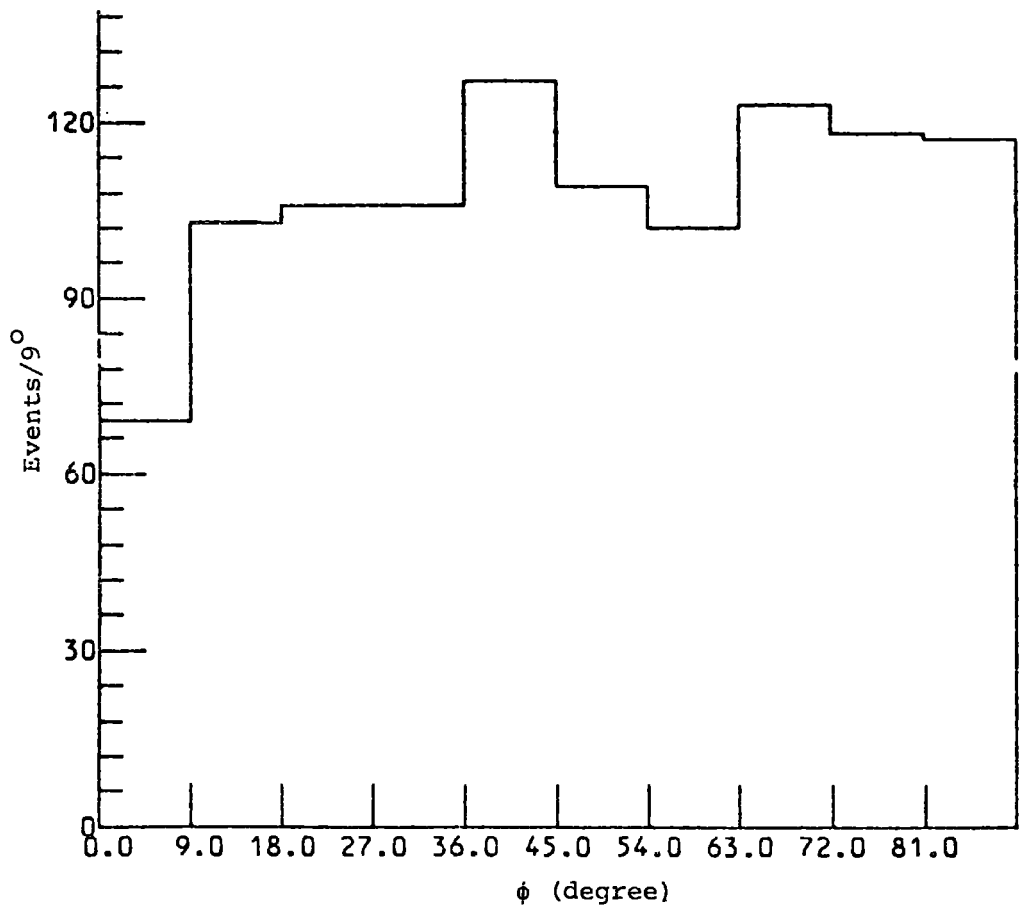


Figure 5.16:  $\phi$ -distribution for unbiased  $\Lambda^0$ -events

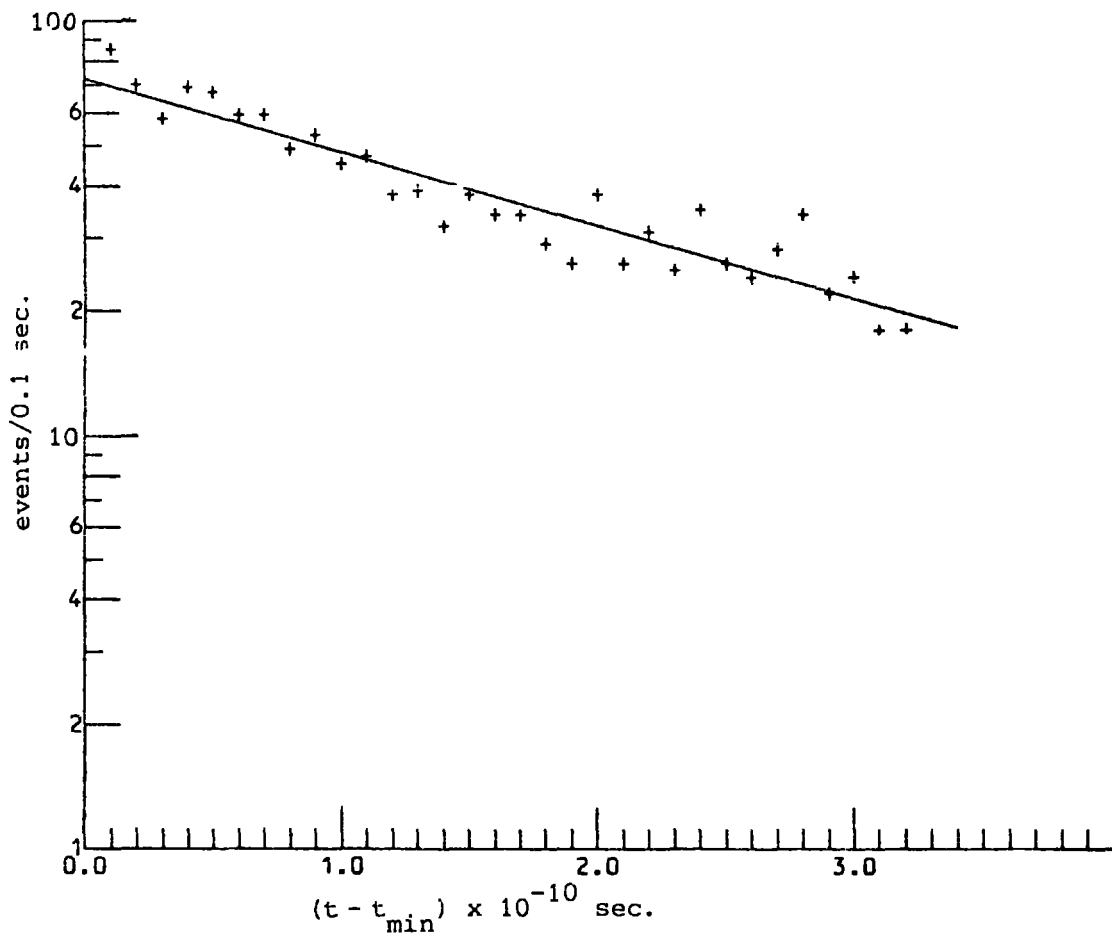


Figure 5.17: Lifetime-distribution for unbiased  $\Lambda^0$ -events.  
 $t_{\min}$  is set to  $0.1 \times 10^{-10}$  sec.



(2) the  $\Lambda^{\circ}$ -hyperons were required to have a minimum proper time of flight of  $t_{\min} = 0.1 \times 10^{-10}$  second and, depending on the incident  $\bar{K}$ -momentum, to have a maximum proper time of  $t_{\lim}$ . The correction factor is computed from the relation

$$CF = \frac{1}{e^{-t_{\min}/\tau} - e^{-t_{\lim}/\tau}} \quad (5.9)$$

where  $\tau$  is the lifetime of the  $\Lambda^{\circ}$  and  $t_{\lim}$  has been defined previously. The correction factor is 1.279, 1.361, 1.447 and 1.565 respectively for the four intervals of  $\bar{K}$ -momentum described in the previous section.

(3)  $\Lambda^{\circ}$ -hyperons produced in a half cone of production were doubled to compensate for the other half of the production cone.

(4) as described in the previous section, events with  $\phi < 9^{\circ}$  and those for which  $(\hat{P} \cdot \hat{\Lambda})_{CM} > 0.8$  were removed from the data. The remaining  $\Lambda^{\circ}$ 's were scaled respectively by a factor of  $\frac{90}{90-9}$  in the first and by a factor of  $\frac{10}{10-1}$  in the second case.

(5) for events with  $(P_{\Lambda})_{LAB} < 160$  MeV/c the  $\phi$ -distribution as well as the time of flight distribution for  $\Lambda^{\circ}$ 's showed a loss below  $45^{\circ}$ .

From the two distributions, a correction factor was calculated to accommodate these losses. This correction factor was also computed by fitting a Legendre polynomial of the form

$$\frac{dN}{dX} = \sum_{n=0}^{\ell} A_n P_n(X) \quad (5.10)$$

to the production angular distribution above  $(\hat{K} \cdot \hat{\Lambda})_{LCM} = -0.8$ . In the above relation  $A_n$  are constant coefficients and  $\ell$  was 3. The fitted angular distributions were then extrapolated to  $(\hat{K} \cdot \hat{\Lambda})_{LCM} = -1$ . To give the

expected number of  $\Lambda^0$ 's below  $(\hat{K} \cdot \hat{\Lambda})_{\text{LCM}} = -0.8$ . These  $\Lambda^0$ -hyperons have momentum less than 160 MeV/c (see figure 5.11b). Both methods gave almost the same correction factor which is of the order of 1.33.

(6) finally an estimate of loss due to scanning inefficiency and unmeasurable events was made and a correction factor of 1.281 was introduced to account for these losses. It must be pointed out that the decision whether an event is unmeasurable was made by a physicist.

All the above correction factors and where they have been applied are shown in Table 5.5.

Table 5.5 Corrections applied to  $\Lambda^0$ -channels

Origin of the Loss	Where the Corrections are Applied	Correction Factor	
Unseen mode of decay	All $\Lambda^0$ 's	1.557	
Proper time cut-off	$\Lambda^0$ 's with	$P_{K^-} = 200 - 320$	1.279
		$= 320 - 370$	1.361
		$= 370 - 410$	1.447
		$= 410 - 500$	1.565
	MeV/c		
Geometry selection	$\Lambda^0$ 's produced in a half cone of production	2	
Scanning ineff. and unmeasurable events	All $\Lambda^0$ 's	1.281	

### 5.7 Selection of unbiased $\bar{K}^0$ events

The reaction studied was  $\bar{K}P \rightarrow \bar{K}^0 n$  with the  $\bar{K}^0$  undergoing  $\pi^+ \pi^-$  decay ( $\bar{K}^0$ -channels) for which the level of confidence for the fit

was greater than  $10^{-3}$ . The following selections were applied to these events.

Length cuts When a  $\bar{K}^0$  decays very close to the production vertex, the event can be mistaken with one produced in the reaction  $K^-P \rightarrow \pi^\pm \Sigma^\mp$  followed by  $\Sigma^\pm \rightarrow n \pi^\pm$  in which the decaying  $\Sigma$ -hyperon is too short to be seen or alternatively in the 3-body final states  $\pi^+ \pi^- \Lambda^0$  where the  $\Lambda^0$ -hyperon is not seen to decay. A similar selection to that applied to  $\Lambda^0$ -channels was made here. From the distribution of time of flight for  $\bar{K}^0$ 's,  $t_{\min}$  was set to  $0.1 \times 10^{-10}$  second.  $t_{\lim}$  for  $\bar{K}^0$ 's were set to the time at which the  $\bar{K}^0$  leaves the fiducial volume.

Angle cuts The distribution of the angle  $\phi$  defined in equation 5.8 was obtained for  $\bar{K}^0$ 's (Fig. 5.18) and showed clear losses at small values of  $\phi$ .

Since  $\bar{K}^0$ 's have short lifetime relative to that of  $\Lambda^0$ 's, the selection of events by dividing the target into several regions did not improve the  $\phi$ -distribution significantly. It was checked to see if the loss in  $\phi$  is related, by any means, to the opening angle of the  $\bar{K}^0$  decay which is always wide and larger than  $\sim 80^\circ$  at our momentum. No relation could be found. Finally the decay angular distribution for  $\bar{K}^0$ 's was obtained which is shown in Figure 5.19. This distribution does not show a significant loss either. Therefore all the events with  $\phi < 45^\circ$  were scaled by a factor to bring them to the average of those with  $\phi \geq 45^\circ$ .

The correction factors for  $\bar{K}^0$ -channels are shown in Table 5.6.

## 5.8 Cross-section Evaluation

Having calculated the correction factors and the tracklength per  $20 \frac{\text{MeV}}{c}$  incident  $K^-$ -momentum interval, the absolute cross-sections were then evaluated for  $\Lambda^0$ + neutrals and  $\bar{K}^0$ n channels. For this purpose,

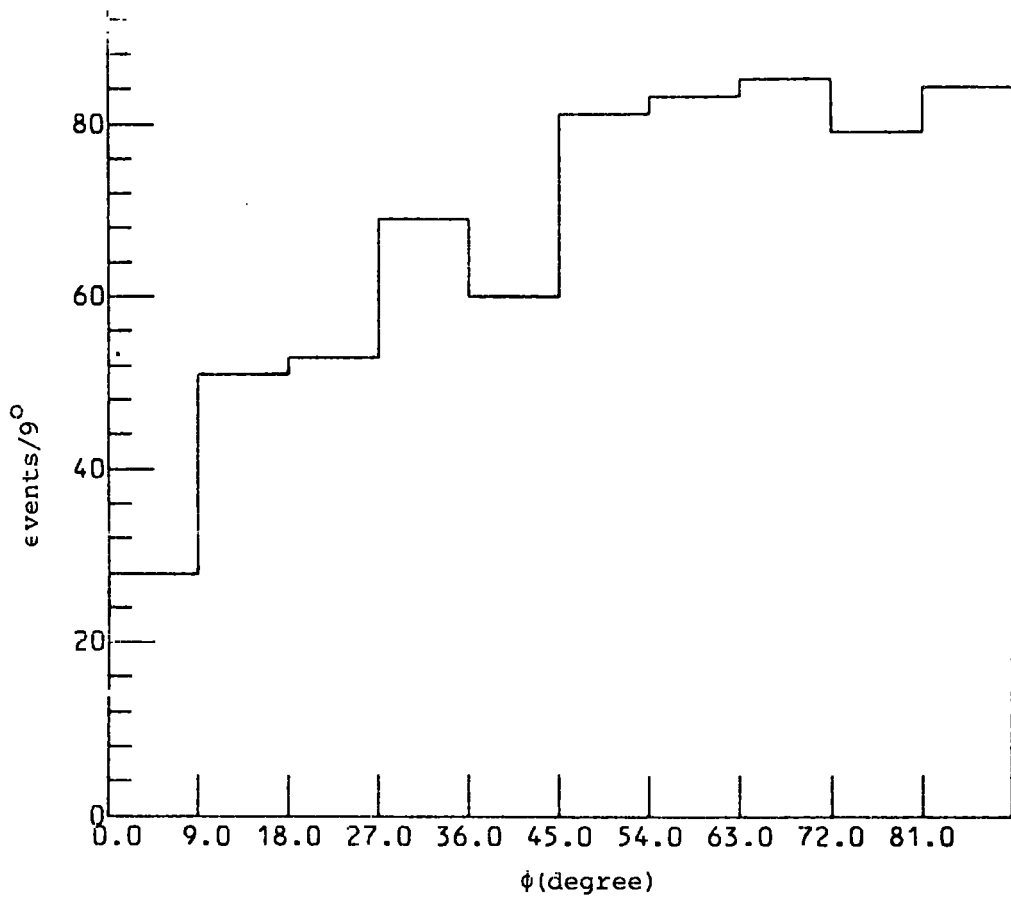


Figure 5.18:  $\phi$ -distribution for  $\bar{K}^0$ -events

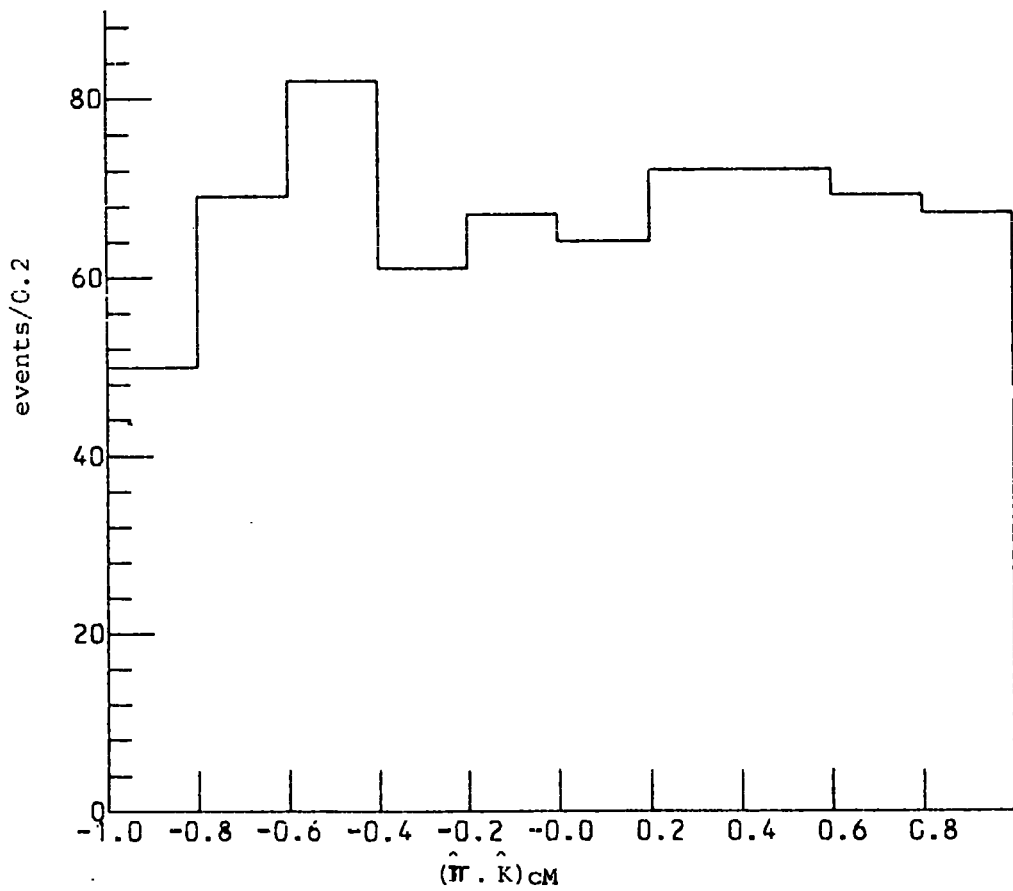


Figure 5.19: Decay angular distribution for  $\bar{K}^0$ -events.

Table 5.6: Corrections applied to  $\bar{K}^0$ -channels

Origin of the loss	Where the Corrections were applied	Correction factor
Unseen mode of decay	All $\bar{K}^0$ 's	1.454
$\bar{K}_L^0$ 's	All $\bar{K}^0$ 's	2
Proper time cut-off	All $\bar{K}^0$ 's	Eq. 5.10
Scanning ineff. and unmeasurable events	All $\bar{K}^0$ 's	1.265

Durham data only were used. Average cross-section per momentum interval can be calculated from the relation ,

$$\sigma(\text{mb}) = \frac{N}{N_0 \rho L}$$

where N = total number of events per momentum interval

$L^\dagger$  = pathlength per momentum interval (cm.)

$\rho^*$  = density of liquid hydrogen (0.055 g/cm<sup>3</sup>)

$N_0$  = Avogadro's number (6.022 x 10<sup>23</sup> mole<sup>-1</sup>).

In Tables 5.7 and 5.8 the cross-sections for  $\Lambda^0 +$  neutrals and  $\bar{K}^0 n$  reactions as a function of momentum are shown respectively. These cross-sections together with the corresponding data of Mast et al (ref. 5.1) are also shown in Figure 5.20. Although the peak from  $\Lambda(1520)$  is not as evident as in ref. (5.1), it is quite pronounced. Obviously one of the sources of error in the value of cross-section is the measurement of the incident  $\bar{K}^-$ -momentum of individual primaries. As well as the individual event measurements, an average momentum  $\bar{P}_K$  expected as a function of position in the chamber can be found from the measurements on tau-decays discussed in Section 5.3. (In reference (5.1) the momentum from the position in chamber is more accurate than the individual measurement of primary momentum). The value of  $\bar{P}_K$  is not exactly equal to the average obtained for tau-decays at that position, since the lifetime for tau-decays in laboratory frame of reference is momentum dependent, so that different

---

\* The refractive index which is necessary for spatial reconstruction of particle trajectories is worked out by the program MONGOOSE to be 1.0873. This is found to be equivalent to a density of 0.055 g/cm<sup>3</sup> in the operating condition of the T.S.T. Range-momentum table and the range of muons in hydrogen was consistent with this value for density.

† Geometry values were used in calculating L from  $\tau$ -meson.

Table 5.7: Total cross sections and errors for  
 $\bar{K}P \rightarrow \Lambda^0 + \text{missing neutrals.}$

Momentum ( $\frac{\text{MeV}}{c}$ )	Corrected number of events	Cross Section (mb)
215	40	$17.88 \pm 6.03$
235	81	$18.40 \pm 6.59$
255	211	$22.65 \pm 3.95$
275	198	$12.47 \pm 2.07$
295	325	$14.51 \pm 2.01$
315	318	$10.92 \pm 1.49$
335	400	$10.15 \pm 1.18$
355	501	$10.52 \pm 1.19$
375	616	$11.02 \pm 1.09$
395	774	$13.28 \pm 1.19$
415	651	$11.44 \pm 1.13$
435	391	$8.78 \pm 1.10$
455	181	$6.31 \pm 1.16$
475	108	$10.38 \pm 2.59$
495	27	$5.48 \pm 2.30$

Table 5.8: Partial cross sections for  $\bar{K}^- p \rightarrow \bar{K}^0 n$

Momentum ( $\frac{\text{MeV}}{c}$ )	Corrected number of events	Cross-section (mb)
215	32	$15.09 \pm 5.68$
235	37	$8.74 \pm 3.64$
255	95	$10.72 \pm 4.80$
275	178	$11.76 \pm 4.50$
295	198	$9.26 \pm 3.44$
315	112	$5.03 \pm 2.14$
335	252	$6.77 \pm 2.35$
355	281	$6.23 \pm 2.11$
375	404	$7.64 \pm 2.36$
395	537	$9.76 \pm 2.82$
415	398	$7.39 \pm 2.29$
435	287	$6.82 \pm 2.30$
455	110	$4.06 \pm 1.75$
475	54	$5.43 \pm 2.84$



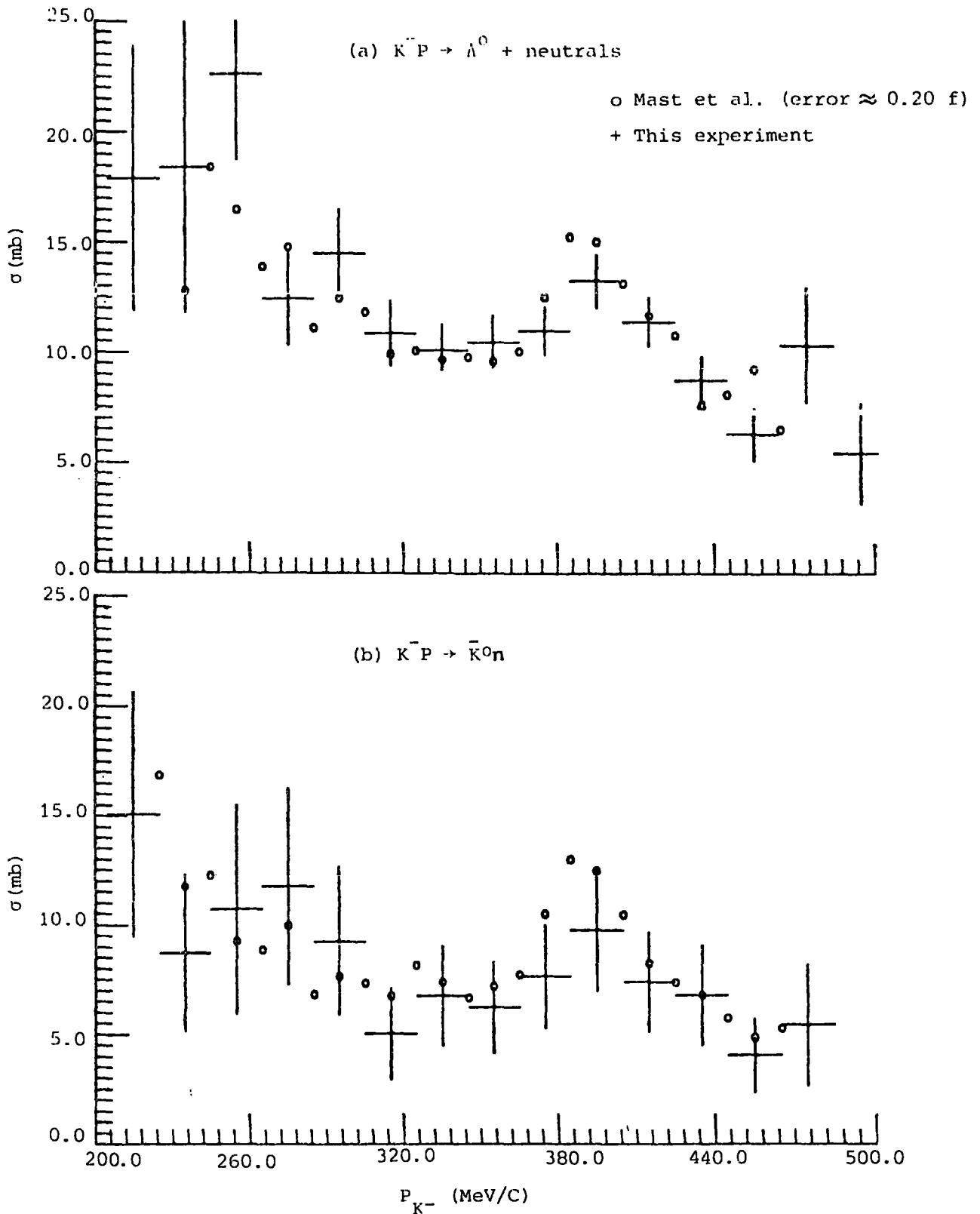


Figure 5.20: (a) cross-section for the reaction  $K^- P \rightarrow \Lambda^0 + \text{neutrals}$  as a function of incident momentum.  
 (b) Cross-section for the reaction  $K^- P \rightarrow \bar{K}^0 n$ .  
 f represents a typical error in this experiment.  
 The momentum bin width is shown by horizontal bars.

fractions of the total beam decay at different momenta. Weighting the averages from the tau-decays to take this effect into account, values of  $\bar{P}_K$  and the variance  $\langle \Delta P_K^2 \rangle$  of the mean were found for different positions in the chamber (see Table 5.9). This information could then be averaged with the direct measurement of primary momentum  $(P_{K\Lambda})$  for each  $\Lambda^0$ -event to give

$$\bar{(P_{K\Lambda})} = \frac{\bar{P}_K / \langle \Delta P_K^2 \rangle + (P_{K\Lambda}) / \langle \Delta (P_{K\Lambda})^2 \rangle}{1 / \langle \Delta P_K^2 \rangle + 1 / \langle \Delta (P_{K\Lambda})^2 \rangle}$$

where  $\langle \Delta (P_{K\Lambda})^2 \rangle$  is the variance on the direct measurement. As can be seen from Table 5.9, the uncertainty of  $\bar{P}_K$  is of the order of 5% which is the same as the direct measurement. Therefore in this experiment the beam-averaging procedure does not yield a better estimate for beam momentum. This implies that the less pronounced peak for the  $\Lambda$  (1520) in this experiment compared to that of ref. (5.1) is due to the poorer momentum resolution which arises from the degrading of the beam from  $\sim 700 \frac{\text{MeV}}{c}$  momentum. This effect also causes other rapidly varying quantities such as Legendre polynomials for the angular distribution to be less pronounced at  $390 \frac{\text{MeV}}{c} \bar{K}^-$ -momentum.

Table 5.9: Mean and variance of primary momentum of tau-decays in different positions in the Chamber.

Block	$L$ (cm)	$\bar{P}_{K^-}$ ( $\frac{\text{meV}}{C}$ )	$\langle \Delta P_K^2 \rangle$ ( $\frac{\text{MeV}}{C}$ ) <sup>2</sup>
3	2	366.34	324.38
	10	354.38	558.18
	18	353.71	311.94
	26	344.76	433.27
	34	343.57	406.59
4	2	397.14	544.57
	10	399.11	621.68
	18	393.54	489.34
	26	392.01	465.21
	34	344.46	446.38

\* See Table 2.1

\*\* L is measured from the entrance to the fiducial volume.

## CHAPTER 6

### DIFFERENTIAL CROSS-SECTIONS AND

### POLARISATIONS IN THE NEUTRAL CHANNELS

In this chapter the Legendre expansion coefficients for the differential cross-sections and polarisations of the reactions listed in (5.1) are determined and compared with the results of ref. 6.1 to 6.3 . Although this determination is straightforward for the charge-exchange channel, because of a partial kinematic overlap, it is rather difficult to determine the coefficients for the separate  $\Lambda^0\pi^0$  and  $\Sigma^0\pi^0$  channels. Much of the difficulty arises from the fact that in both reactions the hyperon is seen only through the decay products of the  $\Lambda^0$ -hyperon in the final state and unless a large number of gamma rays is detected, it is not possible to make the kinematic fit to each channel separately and hence resolve the ambiguity. As described in chapter one, with a T.S.T. chamber there is a chance of detecting gamma rays through their conversions to  $e^+e^-$  pairs but unfortunately at the time of this analysis the number of  $\Lambda^0$ -events with fitted gamma rays was not enough to be used for the detailed analysis. Nevertheless, in section 6.4 the available sample of events, constrained to fit  $\Lambda^0\pi^0$  and  $\Sigma^0\pi^0$ , will be looked at and the results extracted will be compared with the corresponding ones obtained in this chapter. The data analysed in this chapter, therefore, contains all  $\Lambda^0$ -channels and  $\bar{K}^0$ -channels (see the introduction to Chapter 5 for the definition of  $\Lambda^0$  and  $\bar{K}^0$ -channels) and the main problem to be considered is obviously the separation of the  $\Lambda^0\pi^0$  and  $\Sigma^0\pi^0$  final states.

#### 6.1 Separating $\Lambda^0\pi^0$ and $\Sigma^0\pi^0$ Channels

In reference 6.2 an event by event maximum likelihood analysis

has been made to extract simultaneously the channel fractions and Legendre polynomial expansion coefficients for  $\Lambda^0\pi^0$  and  $\Sigma^0\pi^0$  final states. This uses the measured missing mass squared ( $MM^2$ ), its angle of production and the  $\Lambda^0$ -decay angle. The value of  $MM^2$  is given by

$$MM^2 = m_K^2 + m_p^2 + m_\Lambda^2 + 2E_K m_p - 2(E_K + m_p) E_\Lambda + 2\vec{P}_\Lambda \cdot \vec{P}_K \quad (6.1)$$

where  $m$  is mass and  $E$  and  $\vec{P}$  denote total energy and momentum respectively as measured in the laboratory system. The subscripts to the symbols refer to the respective particles. In Figure 6.1, the  $MM^2$  distribution is shown for all  $\Lambda^0$ -channels. The unit of  $MM^2$  in this thesis is  $m_{\pi^0}^2$  where  $m_{\pi^0} = 0.135 \text{ GeV}/c^2$  is the mass of the neutral pion. The peak at  $MM^2 = 1$  clearly shows the presence of the  $\Lambda^0\pi^0$  channel, but equally, Figure 6.1 shows that there is a part of the distribution where the events may be equally interpreted as being due to either  $\Lambda^0$  or  $\Sigma^0$  reactions. The extraction of information about the individual channels in such a region demands an accurate knowledge of the relative channel contributions to the total. This leads to a multi-parameter fit to all the data and it relies on the proper folding in of measurement errors into the expressions for likelihood. In this preliminary analysis, a simpler approach is used that requires first the use of the  $MM^2$  distribution to determine the overall channel fractions and then the extraction of the polynomial coefficients from events in those regions of the  $MM^2$  distribution where one of the  $\Lambda^0$  or  $\Sigma^0$  channels dominated, so that imperfect knowledge about the other background channel would not be important.

The final states contributing to the distribution of  $MM^2$  in Figure 6.1 are  $\Lambda^0\pi^0$ ,  $\Sigma^0\pi^0$ ,  $\Lambda^0\pi^0\pi^0$  and  $\Lambda^0\gamma$  in the momentum range of this experiment. The expected  $MM^2$  distribution for these channels without the effect of measurement errors are shown in Figure 6.2. The

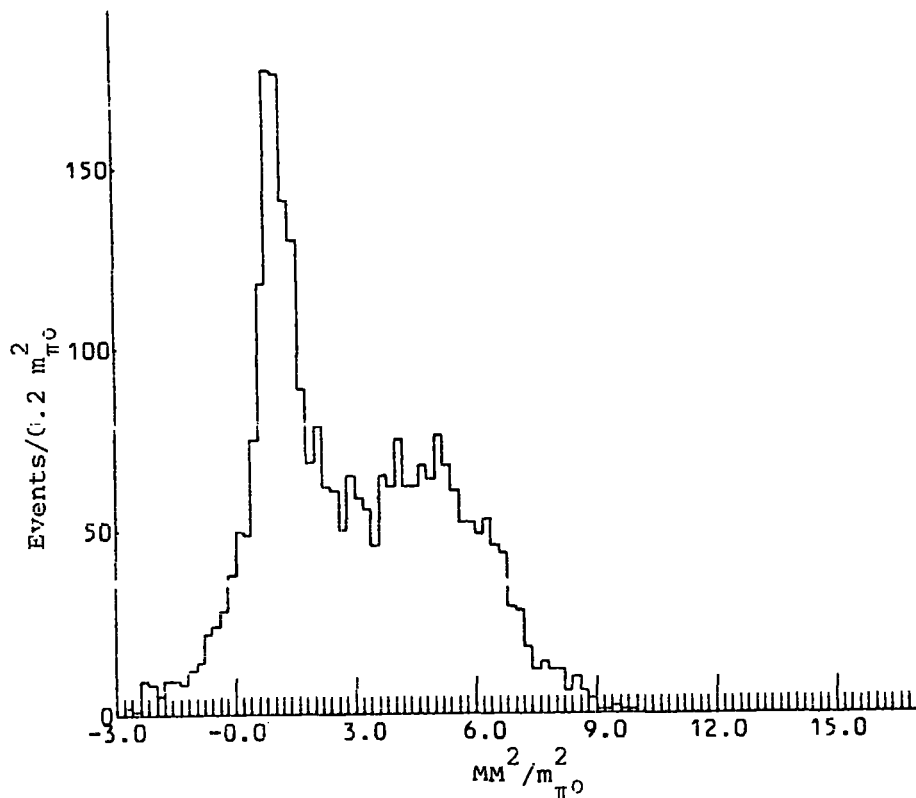


Figure 6.1: Measured distribution of missing mass squared for the reaction  $K^-P \rightarrow \Lambda^0 + \text{neutrals}$ .

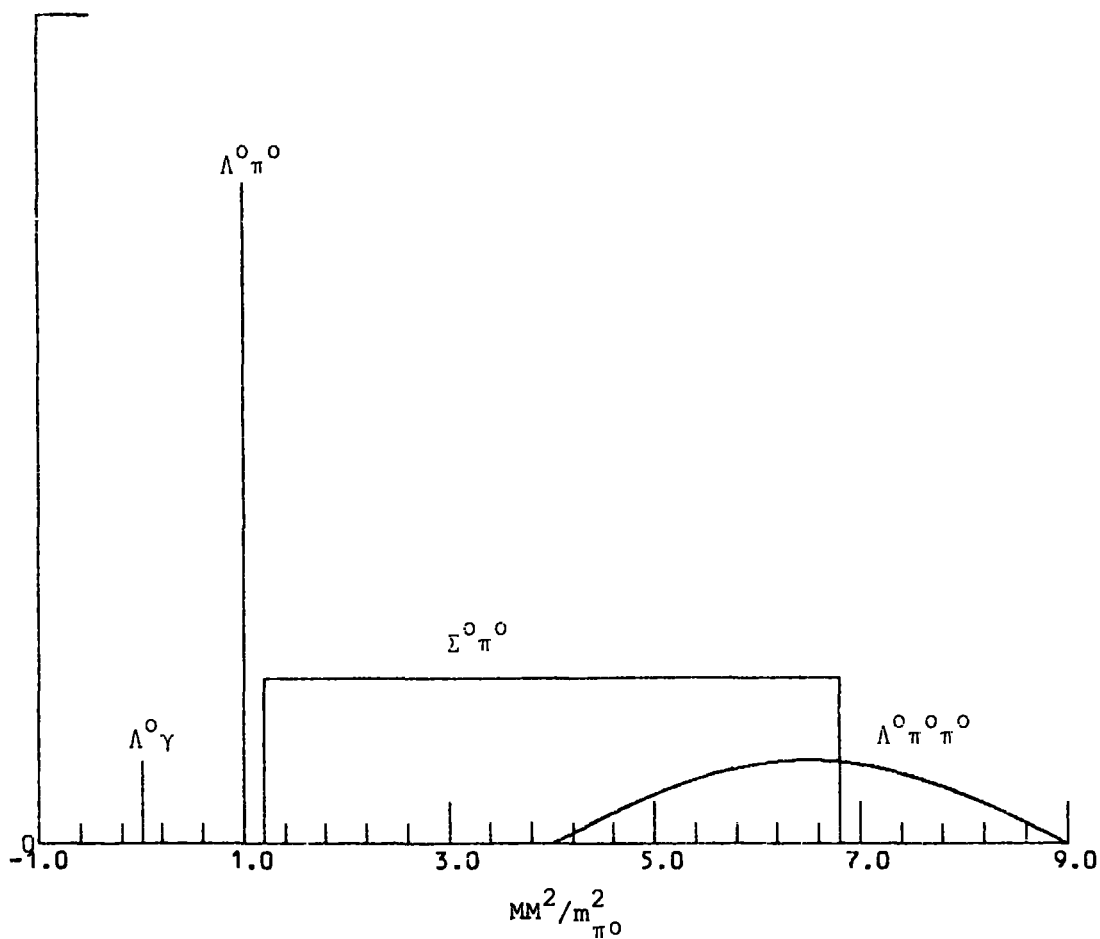
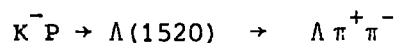


Figure 6.2: Schematic diagram of the  $MM^2$ -distributions expected from different final states.

relative normalisations are arbitrary in this figure. The  $\Lambda^0 \pi^0$  reaction gives events at  $m_{\pi^0}^2$  and the  $\Lambda^0 \gamma$  channel, the electromagnetic decay of the  $Y_0^*$  (1520), gives events at zero. The  $\Sigma^0 \pi^0$  channel contributes a rectangular distribution, the upper and lower limits of which vary slightly with incident  $\bar{K}$ -momentum. This is because the angle between  $\pi^0$  and the gamma ray from the  $\Sigma^0$ -decay forms an isotropic distribution in the  $\Sigma^0$  rest frame. Finally the  $\Lambda \pi^0 \pi^0$  reaction starts with lower limit at  $m_{\pi^0}^2$  and its upper limit varies with the centre of mass energy available. The detailed shape depends on the dynamics of the 3-body process and in Figure 6.2 just a phase-space shape is shown for the purpose of illustration. In this analysis the information for  $\Lambda \pi^0 \pi^0$  events were extracted from measured and fitted events of the type  $\Lambda \pi^+ \pi^-$ . Using charge independence, the number of  $\Lambda \pi^0 \pi^0$  events is then  $\frac{1}{2}$  of the  $\Lambda \pi^+ \pi^-$  events. To make sure that the observed sample of  $\Lambda \pi^+ \pi^-$  events is complete, the cross-section for this channel was compared with the data of reference 6.4 in Figure 6.3 and shown in Table 6.1. The  $\Lambda^0$  selection was identical with that discussed in Chapter 5 for the  $\Lambda^0$ -neutral channel (see Section 5.2). Bearing in mind that the statistics for this channel is about 5% of that in reference 6.4 and that momentum resolution is poorer (see Section 5.8), the agreement is very good. It was found in reference 6.4 that the production of  $\Lambda \pi^+ \pi^-$  events is dominated by the formation reaction



and Figure 6.3 is consistent with this. Therefore, we may consider  $\Lambda \pi^0 \pi^0$  events as all coming from the  $\Lambda(1520)$ . Later when the  $\Lambda^0$ -events are divided into different momentum intervals to evaluate the fractions of  $\Lambda^0 \pi^0$  and  $\Sigma^0 \pi^0$  channels, the shape of the contribution of  $\Lambda \pi^0 \pi^0$  events

in the  $MM^2$ -distribution will be taken to be the same for all intervals. Finally, the distribution of the  $MM^2$  of  $\Lambda\pi^+\pi^-$  events is shown in Figure 6.4.

Table 6.1: Partial Cross-Sections for  $K^-P \rightarrow \Lambda^0\pi^+\pi^-$

Momenum $\left(\frac{\text{MeV}}{C}\right)$	Corrected number of events	Cross-Section (mb)
275	10	.48 ± .29
295	13	.45 ± .33
315	24	.67 ± .27
335	34	.70 ± .39
355	41	.69 ± .26
375	119	1.71 ± .43
395	126	2.16 ± .36
415	160	1.84 ± .49
435	71	1.22 ± .25
455	26	.72 ± .42

The difference between the observed distribution of the  $MM^2$  for  $\Lambda^0$ -events (Figure 6.1) and the expected one (Figure 6.2) arises from the fact that in the former the errors of measurement on the missing mass squared ( $\Delta MM^2$ ) are involved. The following procedures were then adopted to separate  $\Lambda^0\pi^0$  and  $\Sigma^0\pi^0$  reactions.

Events were divided into six intervals of incident  $K^-$ -momentum each consisting of roughly the same number of events except the last interval which had almost half the statistics compared with the rest. The range of incident momentum  $P_{K^-}$  and the number of events in each



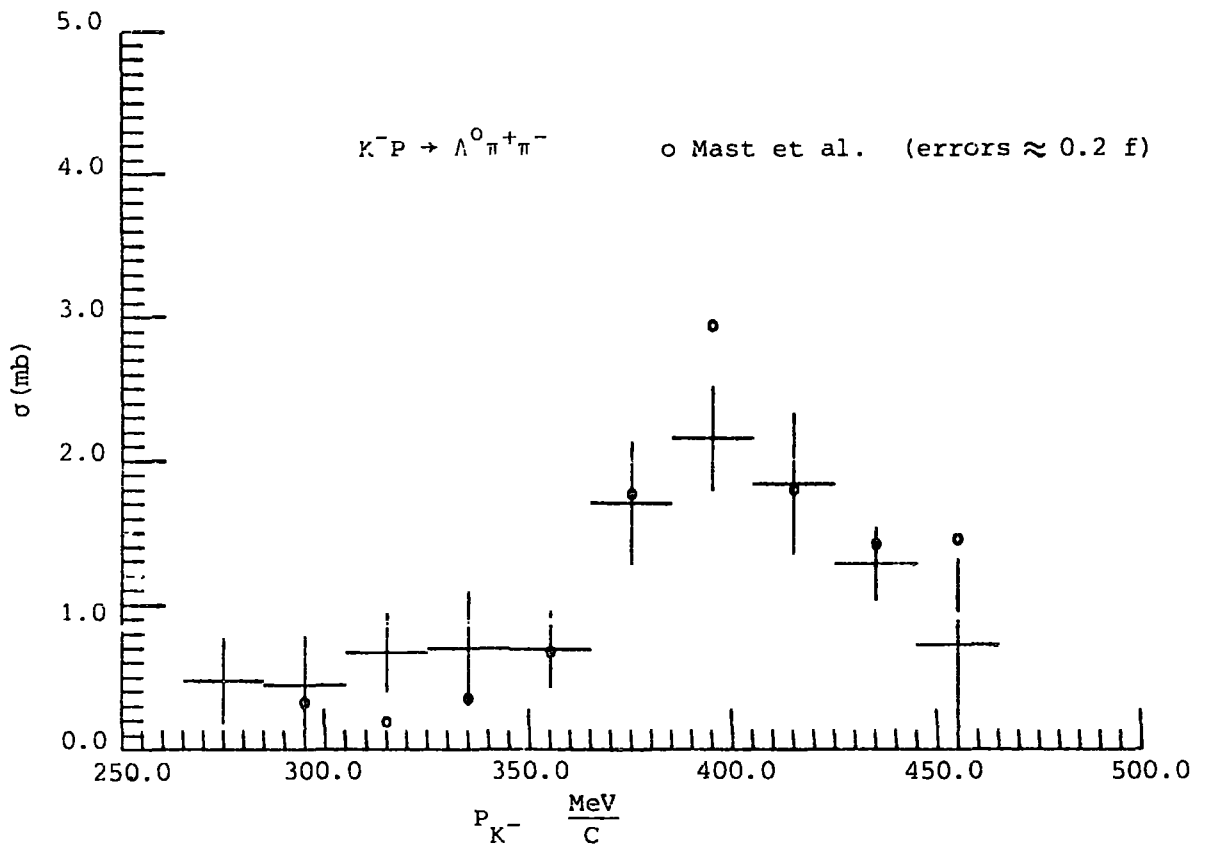


Figure 6.3: Cross-section for the reaction  $K^-P \rightarrow \Lambda^0 \pi^+ \pi^-$  as a function of incident momentum.  $f$  represents the typical error in this experiment. The momentum bin width is shown by horizontal bars.

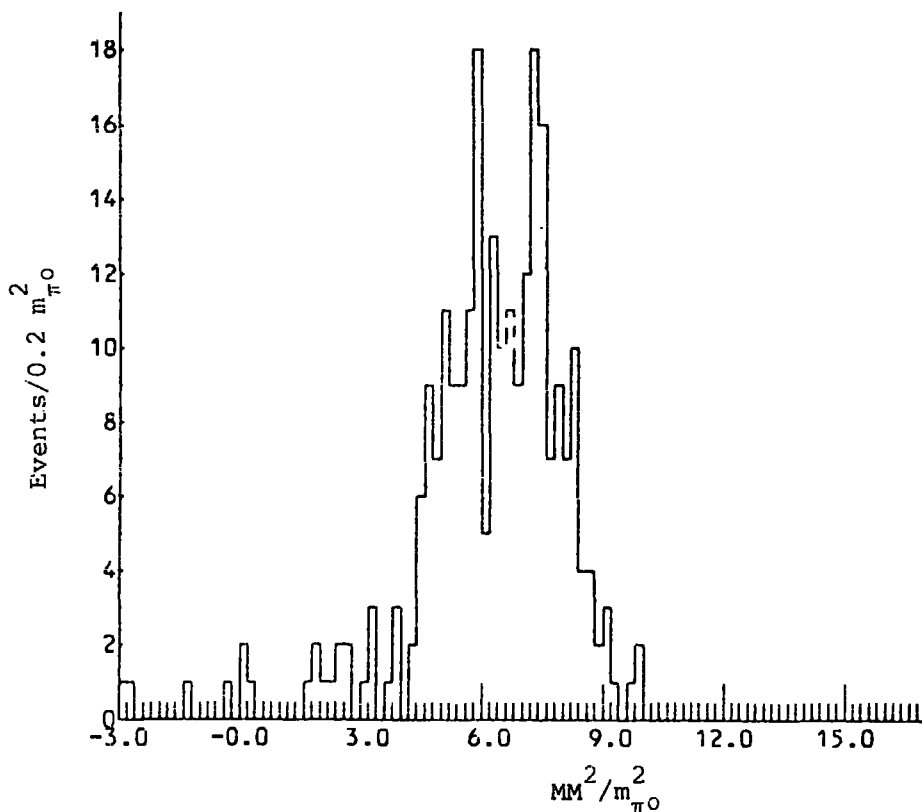


Figure 6.4: Measured distribution of missing mass squared for the reaction  $K^-P \rightarrow \Lambda^0 \pi^+ \pi^-$

interval are shown in Table 6.2. For each momentum interval the distribution of  $\Delta MM^2$  was obtained (see Appendix D) and convoluted into the expected  $MM^2$  distribution assuming the experimental resolution function approximates a Gaussian. This is given by

$$P(MM^2_O, MM^2_E) = \frac{1}{\sqrt{2} (\Delta MM^2)} \exp \left[ - \frac{(MM^2_O - MM^2_E)^2}{2 (\Delta MM^2)^2} \right] \quad (6.2)$$

where  $MM^2_O$  and  $MM^2_E$  are the observed and expected  $MM^2$  respectively. For the  $\Lambda^0 \pi^0$  and  $\Lambda^0 \gamma$  channels,  $MM^2_E$  were set to  $m_{\pi^0}^2$  and zero respectively, and for the  $\Sigma^0 \pi^0$  reaction the exponential term was summed over  $MM^2_E$  from its lower limit to the upper end, these limits being calculated for the centre of each momentum interval. A Chi-square fit was then made to each  $MM^2$  distribution in Figure 6.5 allowing the fraction of the  $\Lambda^0 \pi^0$  to vary. The  $\Lambda^0 \gamma$  fraction was kept fixed at 0.015 (found from ref. 6.5) and the  $\Lambda \pi^0 \pi^0$  contribution put equal to half the observed  $\Lambda \pi^+ \pi^-$  intensity as explained earlier. The program, MINUIT (ref. 6.6), was used for this purpose. The fit then gave the fraction of  $\Lambda^0 \pi^0$  channel contributing to the  $MM^2$  distribution in Figure 6.1. Table 6.2 and Figure 6.6 show the fraction obtained for  $K^- p \rightarrow \Lambda^0 \pi^0$  as a function of incident momentum. Bearing in mind that the statistics are low, the results are in good agreement with the data of ref. 6.2 within the errors. The values of  $\chi^2$  are all larger than expected and are dominated by contributions from a small number of events with negative values of  $MM^2$ . Such events are present in the observed  $MM^2$  distributions of all workers and presumably represent a breakdown in the simple propagation of Gaussian errors used. It is noted that the  $\Lambda^0 \pi^0$  fraction goes through a minimum at  $\sim 390 \frac{\text{MeV}}{c}$ . This is, obviously, because of the presence of  $\Lambda(1520)$  in  $\Sigma^0 \pi^0$  channel and does not contradict the smooth variation of  $\Lambda^0 \pi^0$  cross-section.

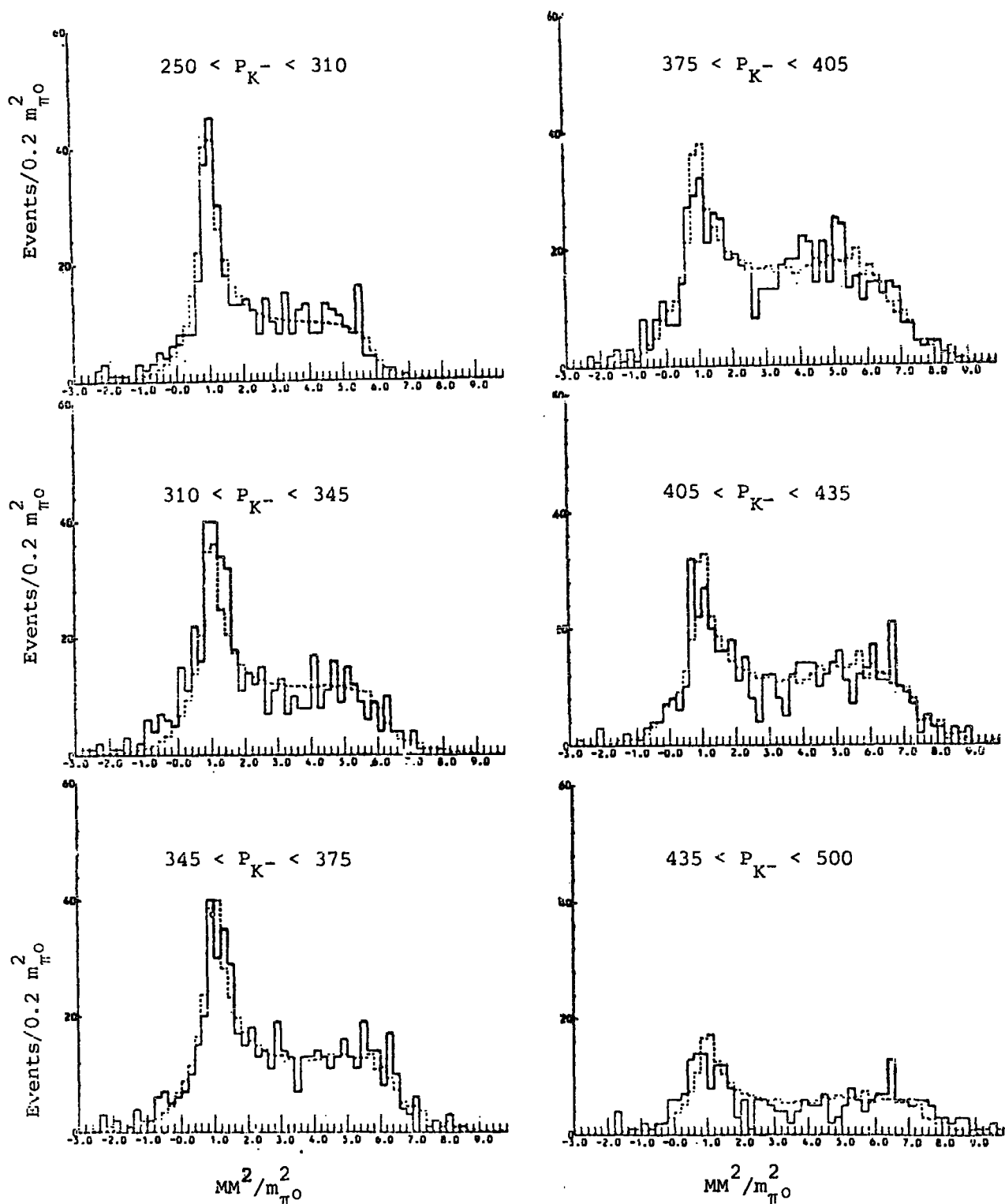


Figure 6.5: Distribution of the square of the missing mass to the  $\Lambda^0$  in the reaction  $K^-P \rightarrow \Lambda^0 + \text{neutrals}$  for the six incident momentum intervals. The dashed histograms are from the fit. The incident momentum is given in  $\frac{\text{MeV}}{c}$ .

Table 6.2: Fraction of  $\Lambda^0\pi^0$  channel to the  $\Lambda^0$ +neutrals

$P_{K^-} \left( \frac{\text{MeV}}{c} \right)$	NEV*	NDF**	$\chi^2$	Fraction $\pm$ error	
250 - 310	519	22	40.48	0.456	0.073
310 - 345	524	29	48.74	0.484	0.063
345 - 375	587	32	40.72	0.385	0.065
375 - 405	503	35	45.61	0.263	0.033
405 - 435	532	35	44.56	0.321	0.084
435 - 500	293	19	50.75	0.380	0.096

\* Number of events

\*\* Number of degrees of freedom

## 6.2 Angular Distribution Expansion Coefficients

In order to obtain the angular distribution expansion coefficients, the production angular distributions were expanded in terms of a Legendre series,

$$\frac{dN}{d(\cos\theta)} = \sum_{\ell} A_{\ell} P_{\ell}(\cos\theta) \quad (6.3)$$

where  $\theta$  is the angle of outgoing  $\Lambda^0$ -hyperon/ $\bar{K}^0$ -meson with the incident  $\bar{K}^-$ -direction in the centre of mass.  $A_{\ell}$  is the coefficient and  $P_{\ell}(\cos\theta)$  is the Legendre polynomial of the order of  $\ell$ . It was found from the previous experiments that terms up to  $\ell = 3$  are sufficient. Fits were then made to angular distribution for different  $\bar{K}^-$ -momentum interval, using MINUIT, to find the coefficients  $A_{\ell}$ . The results for the several neutral channels are discussed in the following three sections:-

### (a) $\bar{K}^-p \rightarrow \bar{K}^0n$

In Table 6.3 the coefficients  $A_{\ell}$  are shown for the charge-exchange reaction  $\bar{K}^0n$  as a function of the average momentum in each momentum interval.

The observed angular distribution for this channel in the interval 375 to 405  $\frac{\text{MeV}}{c}$  is shown in Figure 6.7. On it is drawn the fitted distribution calculated from the coefficients  $A_\ell$ . As can be seen from Table 6.3, below 300  $\frac{\text{MeV}}{c}$  the angular distribution is consistent with being linear in  $\cos\theta$ . In the region of  $\sim 390 \frac{\text{MeV}}{c}$  the distribution shows the  $\cos^2\theta$  dependence from the  $\Lambda(1520)$  resonance (see Figure 6.7). The results are reasonably in agreement with the data of Mast et al (ref. 6.3).

Table 6.3: Legendre polynomial coefficients for  $K^-P \rightarrow \bar{K}^0n$  reaction

Momentum ( $\frac{\text{MeV}}{c}$ )	$A_1/A_0$	$A_2/A_0$	$A_3/A_0$
280	$-0.58 \pm .37$	$0.00 \pm 0.53$	$0.02 \pm 0.82$
327	$-0.22 \pm 0.44$	$0.07 \pm 0.42$	$0.38 \pm 0.57$
360	$0.39 \pm 0.36$	$0.86 \pm 0.37$	$0.76 \pm 0.39$
390	$-0.09 \pm 0.32$	$1.64 \pm 0.22$	$0.09 \pm 0.41$
420	$-0.45 \pm 0.44$	$1.54 \pm 0.31$	$-0.33 \pm 0.49$
455	$-0.36 \pm 0.57$	$1.81 \pm 0.32$	$-0.63 \pm 1.17$

(b)  $K^-P \rightarrow \Lambda^0 \pi^+ \pi^-$

For  $\Lambda \pi^+ \pi^-$  events the values of  $A_\ell$  were obtained, in a similar manner, over the whole incident momentum range. The information from the 'point  $\Lambda^0$ -fit' alone was used, so that the events simulate  $\Lambda^0 \pi^0 \pi^0$ .

$$\begin{aligned}
 A_1/A_0 &= -0.19 \pm 0.28 \\
 A_2/A_0 &= 0.55 \pm 0.32 \\
 A_3/A_0 &= 0.03 \pm 0.42
 \end{aligned}
 \tag{6.4}$$

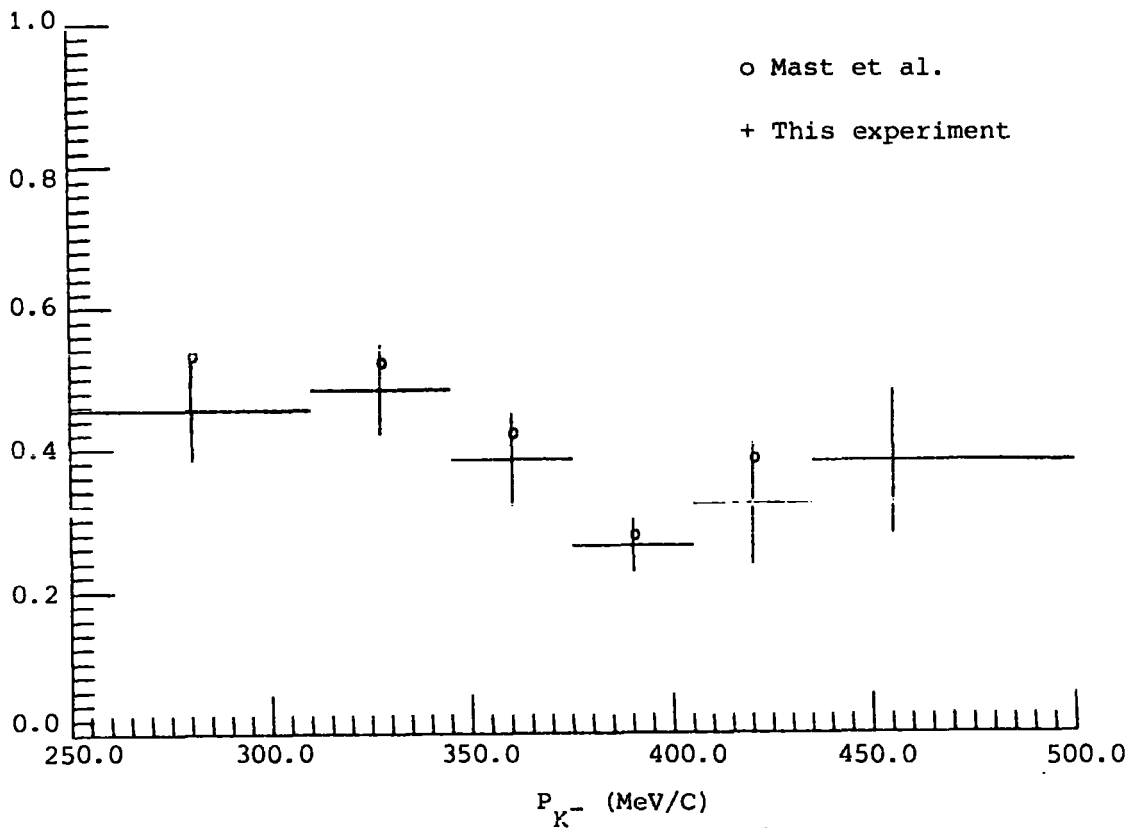


Figure 6.6: The branching ratio of  $K^-P \rightarrow \Lambda^0 \pi^0$  in the reaction  $K^-P \rightarrow \Lambda^0 + \text{neutrals}$  as a function of incident momentum.

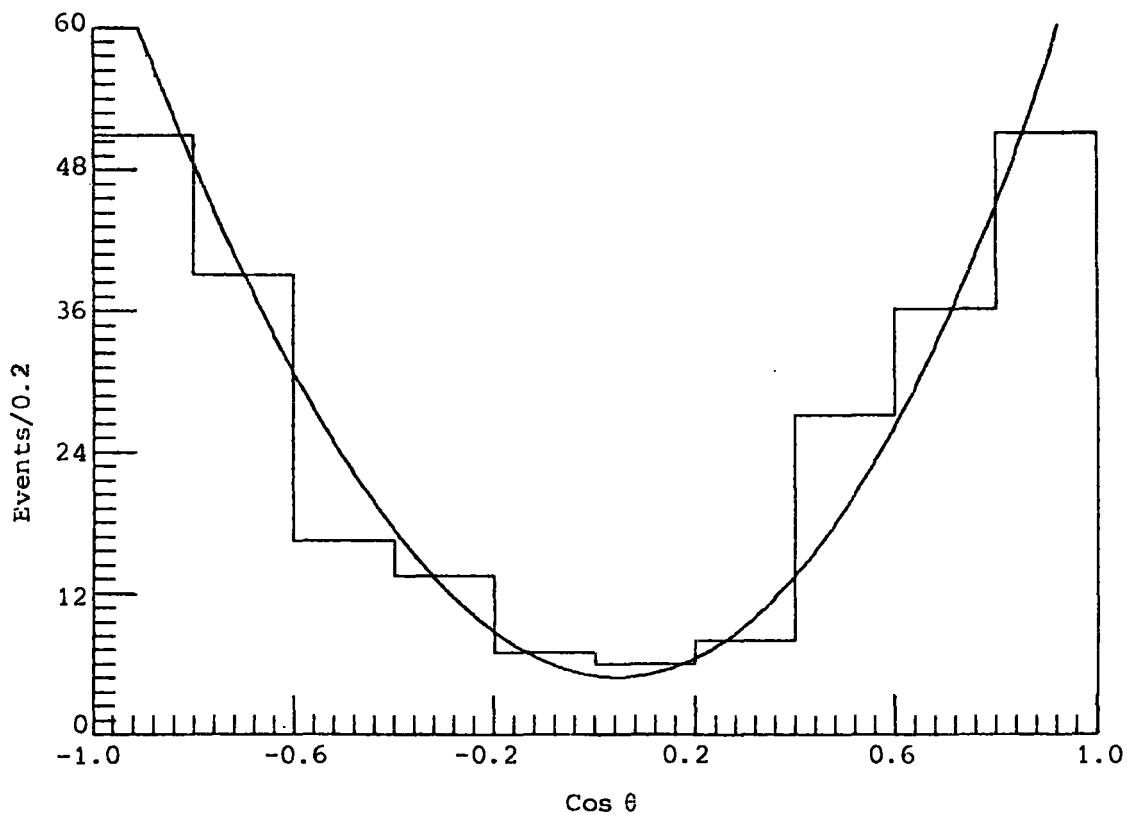
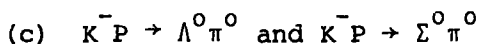


Figure 6.7: Observed angular distribution and fitted curve for the reaction  $K^-P \rightarrow \bar{K}^0 n$  for the momentum interval 375 to 405 MeV/C.

The  $A_\ell$  for  $\Lambda\pi^0\pi^0$  events were assumed to be identical to those listed above for  $\Lambda\pi^+\pi^-$  events and used in extracting  $A_\ell$  for  $\Sigma^0\pi^0$  channel as described below. In Figure 6.8, the observed angular distribution for  $\Lambda\pi^+\pi^-$  events and the curve from the fit to Legendre polynomials are shown.



For the  $\Lambda^0\pi^0$  and  $\Sigma^0\pi^0$  channels the coefficients were determined in the following way:

In Section 6.1 the fraction of  $\Lambda^0\pi^0$  and  $\Sigma^0\pi^0$  channels, in the total  $K^-P \rightarrow \Lambda^0 + \text{neutrals}$  and the distribution of  $P(MM_0^2, MM_E^2)$  were obtained for each momentum interval. It was then possible, using this information, to plot the share from each channel to the  $MM^2$ . Figure 6.9 shows this plot for the momentum interval between 375 to 405  $\frac{\text{MeV}}{c}$ . As can be seen beyond  $MM^2 = 3m_{\pi^0}^2$  the  $\Sigma^0\pi^0$  channel with a small background of  $\Lambda\pi^0\pi^0$  dominate and the contribution of the  $\Lambda^0\pi^0$  channel is negligible. The coefficients  $A_\ell$  describing the angular distribution of these events are, therefore, the weighted average of the two coefficients for  $\Sigma^0\pi^0$  and  $\Lambda\pi^0\pi^0$  channels. By making a fit to the events with  $MM^2$  greater than  $3m_{\pi^0}^2$  and knowing  $A_\ell$  for the 3-body channel (listed in 6.4) it was then possible to determine the coefficients  $A_\ell$  for the  $\Sigma^0\pi^0$  channel.

Returning to Figure 6.9, in order to obtain  $A_\ell$  for the  $\Lambda^0\pi^0$  channel a region of  $MM^2$  distribution was demanded in which the  $\Lambda^0\pi^0$  events dominated with least background from the  $\Sigma^0\pi^0$  reaction. To keep the statistics reasonably large, events between 0 to  $2m_{\pi^0}^2$  were chosen and the fitted values of  $A_\ell$  to the series (6.3) obtained for these events. Knowing the coefficients  $A_\ell$  for  $\Sigma^0\pi^0$  channel, the values of  $A_\ell$  for the  $\Lambda^0\pi^0$  events could be extracted.

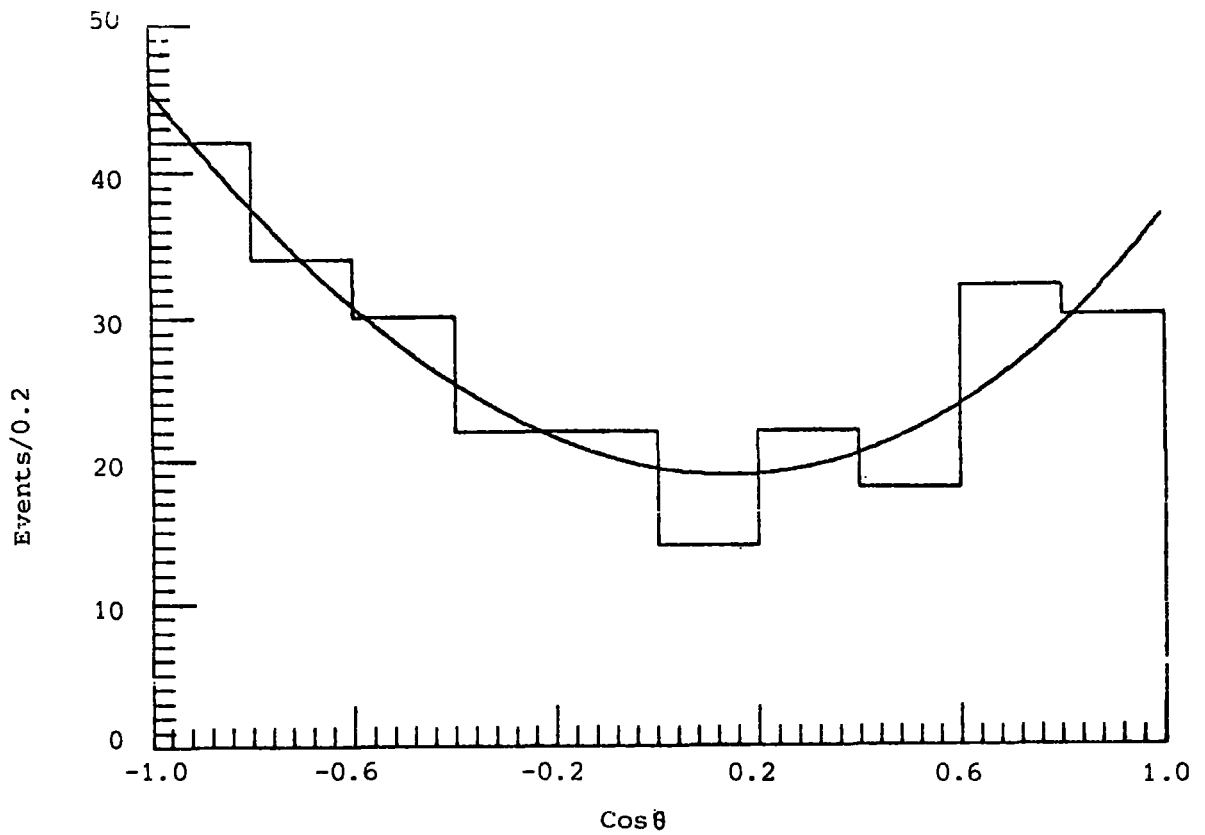


Figure 6.8: Observed angular distribution and fitted curve for the reaction  $K^- P \rightarrow \Lambda^0 \pi^+ \pi^-$ .

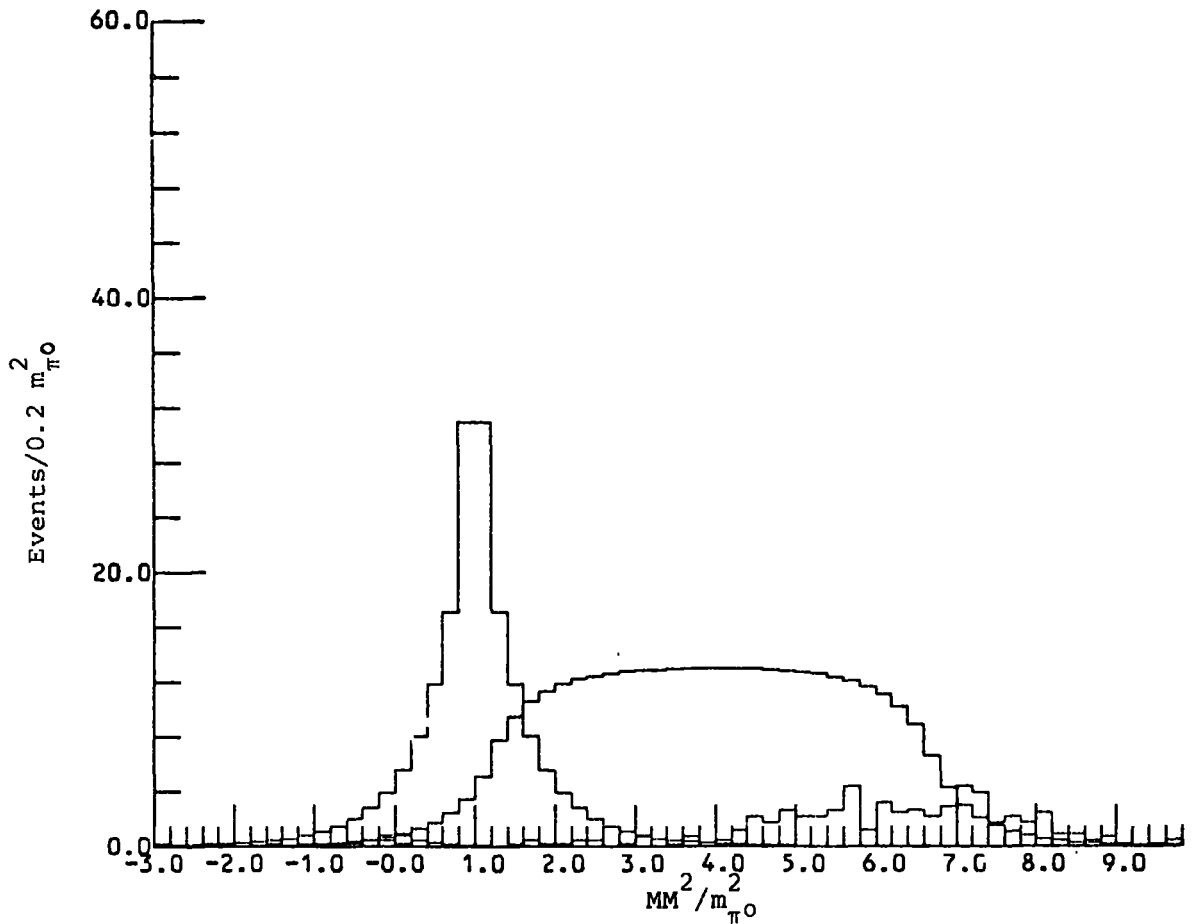


Figure 6.9: Contributions from the final states  $\Lambda^0 \pi^0 \pi^0$ ,  $\Sigma^0 \pi^0$ ,  $\Lambda^0 \pi^0 \pi^0$  and  $\Lambda^0 \gamma$  to the reaction  $K^- P \rightarrow \Lambda^0 + \text{neutrals}$  for the momentum interval 375 to 405  $\frac{\text{MeV}}{c}$ .



There is, of course, one problem here which must be solved. For the  $\Sigma^0 \pi^0$  channel the direction of the  $\Sigma^0$  is unknown ( $\Sigma^0$  cannot be seen) and only the  $\Lambda^0$ -hyperon from the decay of  $\Sigma^0$  is observed. Therefore, the coefficients obtained for these events must be corrected to take into account the effect of the  $\Sigma^0$  direction with respect to that of  $\Lambda^0$ . In order to make this correction, assume  $\theta_\Sigma$  is the angle between  $\Sigma^0$  and the incident  $K^-$  in the centre of mass. It can be shown that  $P_\ell(\cos\theta_\Sigma)$  is related to  $P_\ell(\cos\theta_\Lambda)$  in the following way:

$$P_\ell(\cos\theta_\Sigma) = \frac{4\pi}{2\ell+1} \sum_{m=-\ell}^{m=+\ell} Y_{\ell,m}(\chi, \phi) Y_{\ell,-m}(\theta_\Lambda, 0)$$

where  $\chi$  is the angle between the  $\Sigma^0$  and its decay  $\Lambda^0$  in the centre of mass,  $\theta_\Lambda$  is the centre of mass production angle of  $\Lambda^0$ -hyperon,  $\phi$  is the azimuthal angle of  $\Lambda^0$  around the  $\Sigma^0$  and  $Y_{\ell,m}$  are the spherical harmonic functions. Figure 6.10 shows the relevant geometry, the  $\Lambda^0$  momentum being taken along x-axis and the xy plane containing the beam momentum.

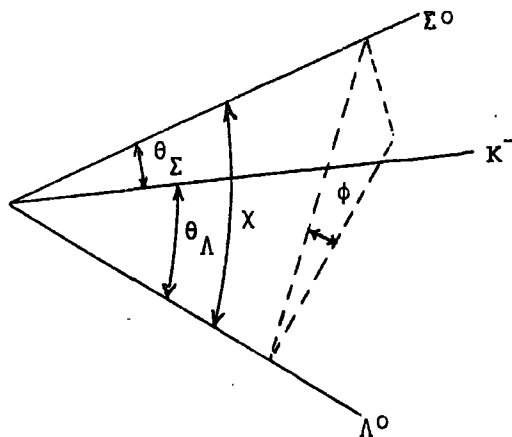


Figure 6.10

Integrating over  $\phi$  gives

$$P_\ell(\cos\theta_\Sigma) = P_\ell(\cos\chi) P_\ell(\cos\theta_\Lambda) \tag{6.5}$$

Equation 6.3, with substitution from equation 6.5, becomes ,

$$\frac{dN}{d(\cos\theta_{\Sigma})} = \sum_{\ell} A_{\ell} P_{\ell}(\cos\chi) P_{\ell}(\cos\theta_{\Lambda})$$

The above equation indicates that to obtain the three coefficients for the  $\Sigma^0\pi^0$  channel, those calculated by fitting to  $\Lambda^0$ -production angular distribution must be divided by the mean value of  $P_{\ell}(\cos\chi)$ . For this purpose, the average of  $P_{\ell}(\cos\chi)$  over each momentum interval was computed for events with  $MM^2$  greater than  $3m_{\pi^0}^2$  using the following equation to calculate  $\cos\chi$ .

$$\cos\chi = \frac{2 E_{\Lambda} E_{\Sigma} - m_{\Sigma}^2 - m_{\Lambda}^2}{2 |\vec{P}_{\Lambda}| |\vec{P}_{\Sigma}|} \quad (6.6)$$

where  $E$ ,  $m$  and  $\vec{P}$  denote energy, mass and momentum in the centre of mass respectively.  $P_{\Sigma}$  was calculated from the relation

$$P_{\Sigma}^2 = \frac{[S - (m_{\Sigma^0} + m_{\pi^0})^2][S - (m_{\Sigma^0} - m_{\pi^0})^2]}{4S}$$

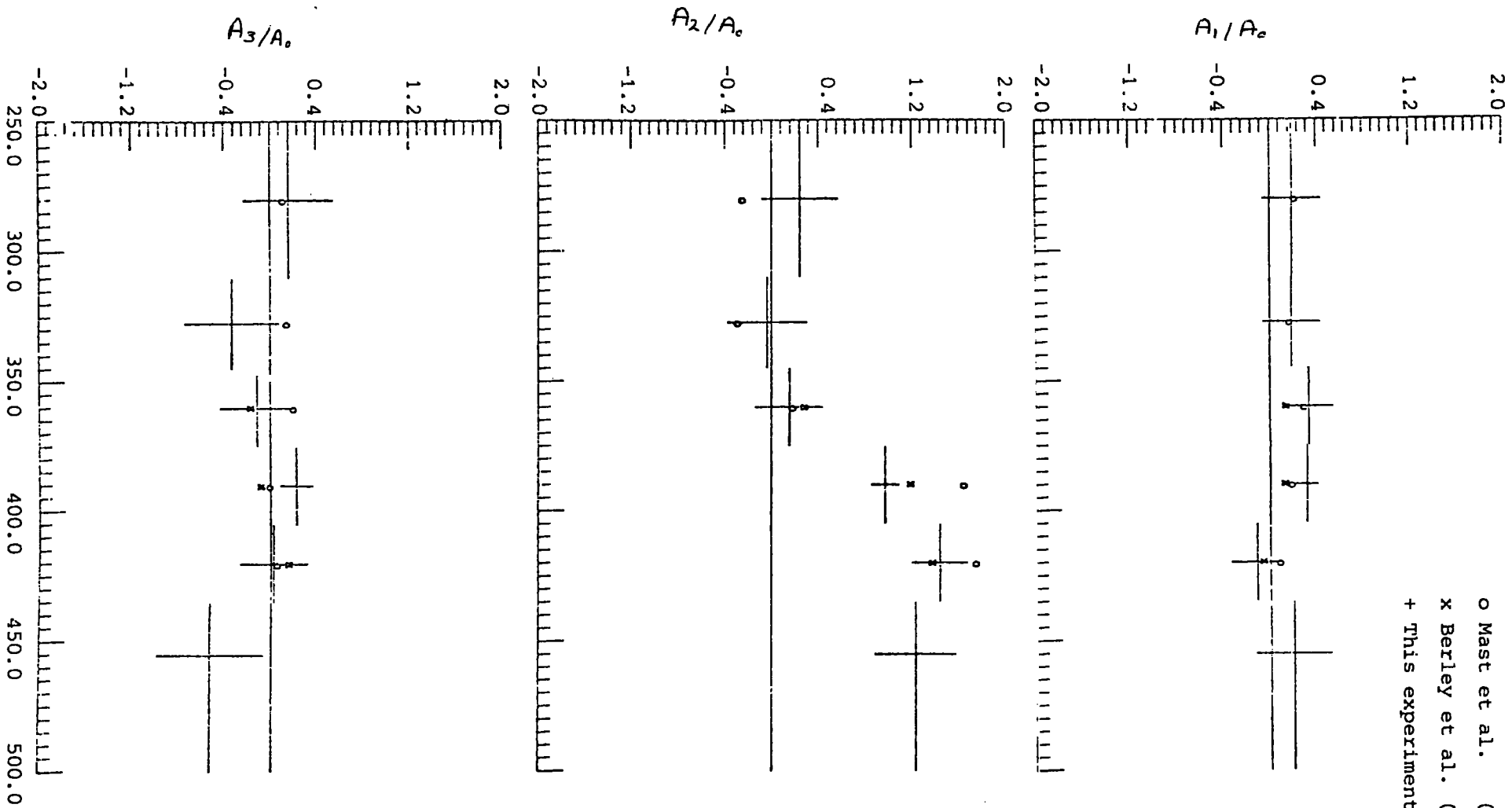
where  $\sqrt{S}$  is the total centre of mass energy. It should be noted that  $P_{\ell}(\cos\chi)$  was never more than 5% away from unity. This is to be expected in the decay of a particle to a massive and a non-massive secondary, that is the  $\Lambda^0$  follows the direction of  $\Sigma^0$  quite closely.

In Table 6.4 the Legendre coefficients for  $\Sigma^0\pi^0$  channel as a function of momentum are shown and also they are plotted in Figure 6.11. The strong contribution from  $\Lambda(1520)$  D wave can be seen in  $A_2/A_0$  distribution. The agreement with refs. 6.1 and 6.2 is very good.

Table 6.4: Production angular distribution  
Legendre coefficients for  $\Sigma^0 \pi^0$  channel

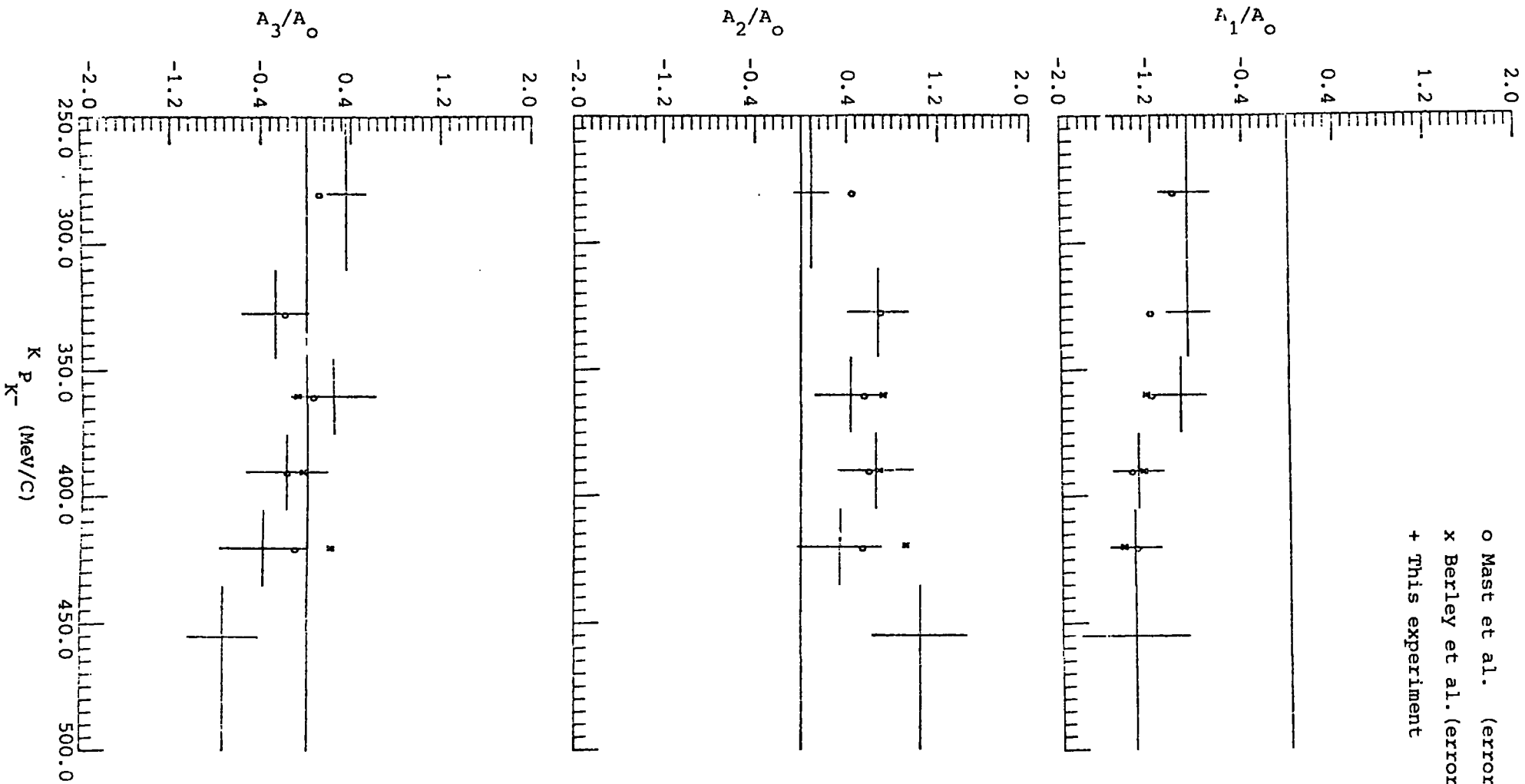
Momentum $\left(\frac{\text{MeV}}{c}\right)$	$A_1/A_0$	$A_2/A_0$	$A_3/A_0$
280	$0.20 \pm 0.25$	$0.25 \pm 0.33$	$0.16 \pm 0.39$
327	$0.19 \pm 0.25$	$-0.04 \pm 0.34$	$-0.33 \pm 0.41$
360	$0.33 \pm 0.21$	$0.16 \pm 0.29$	$-0.11 \pm 0.31$
390	$0.32 \pm 0.10$	$0.98 \pm 0.20$	$0.23 \pm 0.14$
420	$-0.11 \pm 0.22$	$1.45 \pm 0.23$	$0.03 \pm 0.29$
455	$0.19 \pm 0.32$	$1.24 \pm 0.35$	$-0.52 \pm 0.46$

In determining the coefficients to be used for  $\Sigma^0 \pi^0$  events in the sample with  $MM^2$  between 0 to  $2m_{\pi^0}^2$  in order to correct the coefficient for  $\Lambda^0 \pi^0$  events, the average  $P_\ell(\cos\chi)$  were found for  $MM^2$  between 0 to  $2m_{\pi^0}^2$ . In Table 6.5 and in Figure 6.12 the Legendre coefficients for the  $\Lambda^0 \pi^0$  channel are shown for different momentum intervals.  $A_1/A_0$  and  $A_2/A_0$  are significantly non-zero, but  $A_3/A_0$  is consistent with zero. Again the agreement with the data of reference (6.1) and (6.2) is satisfactory. For the  $\Lambda^0$  channel there is no evidence of resonance behaviour.



o Mast et al. (error  $\approx 0.15 F$ )  
 x Berley et al. (error  $\approx 0.30 F$ )  
 + This experiment

Figure 6.11: Production angular distribution Legendre coefficients as a function of incident momentum for the reaction  $K^- P \rightarrow \Sigma^0 \pi^0$ .  $f$  represent the typical error in this experiment. The momentum bin width is shown by horizontal bars.



o Mast et al. (error  $\approx 0.15$  F)  
 x Berley et al. (error  $\approx 0.25$  F)  
 + This experiment

Figure 6.12: Production angular distribution Legendre coefficients as a function of incident momentum for the reaction  $K^-p \rightarrow \Lambda^0 \pi^0$ . f represents the typical error in this experiment. The momentum bin width is shown by horizontal bars.

Table 6.5: Production angular distribution Legendre coefficients for  $\Lambda^0\pi^0$  channel

Momentum ( $\frac{\text{MeV}}{c}$ )	$A_1/A_0$	$A_2/A_0$	$A_3/A_0$
280	$-0.88 \pm 0.20$	$0.09 \pm 0.16$	$0.35 \pm 0.17$
327	$-0.88 \pm 0.19$	$0.68 \pm 0.27$	$-0.28 \pm 0.30$
360	$-0.95 \pm 0.23$	$0.44 \pm 0.32$	$0.24 \pm 0.37$
390	$-1.33 \pm 0.23$	$0.66 \pm 0.33$	$-0.18 \pm 0.36$
420	$-1.36 \pm 0.23$	$0.34 \pm 0.37$	$-0.39 \pm 0.38$
455	$-1.36 \pm 0.47$	$1.05 \pm 0.42$	$-0.74 \pm 0.31$

### 6.3 Polarisation Expansion Coefficients

The polarisation can be measured for  $\Lambda^0\pi^0$  and  $\Sigma^0\pi^0$  channels using the parity non-conservation of the weak decay of the  $\Lambda^0$ -hyperon. For the  $\Sigma^0\pi^0$  channel, however, the effect of not knowing the  $\Sigma^0$  direction must be taken into account.

The  $\Lambda^0\pi^0$  channel, being simpler, will be considered first. For a polarisation  $P$  of the  $\Lambda^0$ , the angular distribution integrated over azimuth of the decay proton in the rest system of the hyperon is given by

$$\frac{dN}{d(\cos b)} = \frac{N_T}{2} (1 + \alpha P \cos b)$$

where  $N_T$  is the total number of events,  $\alpha$  is the decay asymmetry parameter = 0.645 and  $b$  is the angle between the proton and the polarisation direction. Since the production of the  $\Lambda^0$  is due to a parity conserving strong interaction, the hyperon may only be polarised normal to the production plane. The joint distribution of centre of mass

production angle  $\theta_\Lambda$  and decay angle  $b$  can be written generally as

$$\frac{d^2 N}{d(\cos\theta_\Lambda) d(\cos b)} = \frac{N_T}{4} \left[ 1 + \sum_{\ell=1}^3 \frac{A_\ell}{A_0} P_\ell(\cos\theta_\Lambda) + \alpha \cos b \sum_{\ell=1}^3 \frac{B_\ell}{A_0} P_\ell^1(\cos\theta_\Lambda) \right] \quad (6.7)$$

Here the production angular distribution is defined by the Legendre function coefficients  $A_\ell$  which were determined in the last section, and the variation of polarisation with production angle is contained in the value of the coefficients  $B_\ell$  of the associated Legendre polynomials  $P_\ell^1(\cos\theta_\Lambda)$ . The value of  $B_\ell$  can be found by multiplying both sides by  $P_\ell^1(\cos\theta_\Lambda)$  and  $\cos b$  and integrating over  $\cos\theta_\Lambda$  and  $\cos b$ . One then obtains the relation

$$B_\ell = \frac{3(2\ell+1)}{4\ell(\ell+1)} \frac{1}{N_T} \sum_{j=1}^{j=N_T} \cos b P_\ell^1(\cos\theta_\Lambda)_j \quad (6.8)$$

where the integral has been replaced by a sum over the finite sample of  $N_T$  events.

For the  $\Sigma^0 \pi^0$ , the unknown direction of the  $\Sigma^0$  introduces the angle  $\chi$  between the  $\Lambda^0$  and  $\Sigma^0$  in the centre of mass, as explained in the last section. Since the polarisation of the  $\Lambda^0$  depends on the angle  $\chi^*$  between the  $\Lambda^0$  and the  $\Sigma^0$  in the latter's rest frame, the joint distribution function analogous to (6.7) becomes (see Appendix E-a).

$$\frac{d^3 N}{d(\cos\chi^*) d(\cos b) d(\cos\theta_\Lambda)} = \frac{N_T}{8} \left[ 1 + \sum_{\ell=1}^3 \frac{A_\ell}{A_0} P_\ell(\cos\chi) P_\ell(\cos\theta_\Lambda) - \frac{\alpha \cos b}{\ell(\ell+1)} \sin\chi^* \sin(\chi^* - \chi) \sum_{\ell=1}^3 \frac{B_\ell}{A_0} P_\ell^1(\cos\theta_\Lambda) P'_\ell(\cos\chi) \right] \quad (6.9)$$

Figure 6.13 shows the geometry to which equation (6.9) refers.

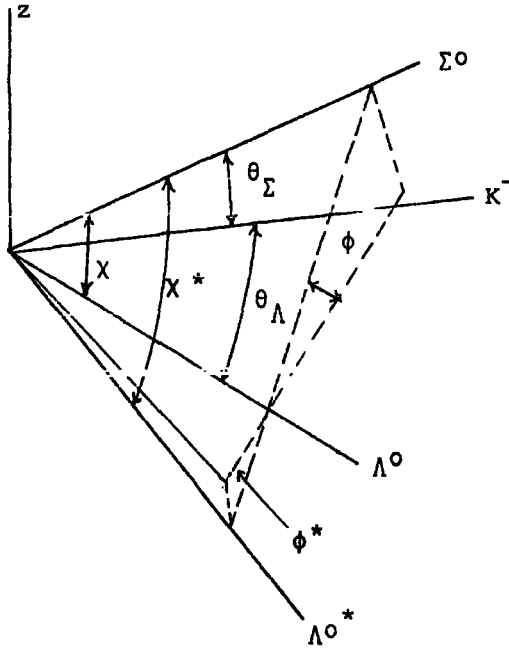


Figure 6.13: The  $\Lambda^0$  momentum is taken along the x-axis and the xy plane contains the beam momentum.

Since, as already mentioned,  $\chi$  is always less than  $15^\circ$ ,  $\cos \chi$  is always within 3% of unity and hence in integrating over  $\cos \chi^*$ , it is a good approximation to replace  $P'_\ell(\cos \chi)$  with  $P'_\ell(1) = \ell(\ell+1)/2$ . For the same reason,  $\sin \chi$  can be taken negligible. The polarisation term in equation (6.9) now becomes:

$$-\frac{\alpha}{2} \cos b \sin^2 \chi^* \sum_{\ell=1}^3 \frac{B_\ell}{A_0} P_\ell^1(\cos \theta_\Lambda)$$

The appropriate expression to project out the values of  $B_\ell$  is now:

$$B_\ell = -\frac{6(2\ell+1)}{\alpha F(\chi_1^*, \chi_2^*) \ell(\ell+1)} \langle \cos b P_\ell^1(\cos \theta_\Lambda) \rangle_{\chi_1^*, \chi_2^*} \quad (6.10)$$

$\chi_1^*$  and  $\chi_2^*$  are the limits of integration over  $\cos \chi^*$  (i.e.  $MM^2$ , see below)



and

$$F(\chi_1^*, \chi_2^*) = 1 - \frac{\chi_1^{*2} + \chi_2^{*2} + \chi_1^* \chi_2^*}{3}$$

As in the last section, events with  $MM^2 > 3m_{\pi^0}^2$  ( $\cos\chi^* < 0.375$ ) were considered as the  $\Sigma^0\pi^0$  sample with a small contamination of the  $\Lambda\pi^0\pi^0$  channel. Appendix E-b shows that the best determination of polarisation is obtained by having a lower limit of  $-0.756$  on  $\cos\chi^*$  (corresponding to  $MM^2 \approx 6.5 m_{\pi^0}^2$ ) since as  $\cos\chi^*$  tends to 1, the amount of polarisation transferred from the  $\Sigma^0$  to the  $\Lambda^0$  becomes zero. To obtain the values of  $B_\ell$  for the  $\Sigma^0\pi^0$  channel, events with  $MM^2$  between 3 and  $6.5 m_{\pi^0}^2$  were used corresponding to  $\chi_2^*$  and  $\chi_1^*$  having values of 0.375 and  $-0.756$  which give  $F(\chi_1^*, \chi_2^*)$  a value of 0.87. The effect of the  $\Lambda^0\pi^0\pi^0$  channel was subtracted using the  $\Lambda^0\pi^+\pi^-$  events as before for which the coefficients are shown below

$$\frac{B_1}{A_0} = 0.06 \pm 0.19$$

$$\frac{B_2}{A_0} = 0.42 \pm 0.27$$

$$\frac{B_3}{A_0} = -0.38 \pm 0.39$$

Shown in Table 6.6 and in Figure 6.14 are the coefficients  $B_\ell$  for  $\Sigma^0\pi^0$  channel as a function of incident  $K^-$ -momentum. The dominance of the  $\Lambda(1520)$  D wave resonance is clearly shown by the behaviour of  $\frac{B_2}{A_0}$ . The agreement with the data of Mast et al (ref. 6.2) and Berley et al (ref. 6.1) is good.

Table 6.6: Polarisation Legendre coefficients for  $\Sigma^0\pi^0$  channel

Momentum ( $\frac{\text{MeV}}{c}$ )	$\frac{B_1}{A_0}$	$\frac{B_2}{A_0}$	$\frac{B_3}{A_0}$
280	$0.47 \pm 0.23$	$-0.33 \pm 0.28$	$0.11 \pm 0.26$
327	$0.02 \pm 0.26$	$0.58 \pm 0.36$	$-0.07 \pm 0.24$
360	$0.16 \pm 0.21$	$0.47 \pm 0.29$	$0.27 \pm 0.19$
390	$0.22 \pm 0.16$	$0.53 \pm 0.26$	$-0.42 \pm 0.21$
420	$0.80 \pm 0.17$	$0.15 \pm 0.31$	$0.44 \pm 0.25$
455	$0.57 \pm 0.27$	$0.11 \pm 0.33$	$-0.04 \pm 0.39$

For  $\Lambda^0\pi^0$  channel, events with  $MM^2$  between zero and  $2m_{\pi^0}^2$  were chosen, subtracting the effect of  $\Sigma^0\pi^0$  contamination, the coefficients  $B_\ell$  were obtained, shown in Table 6.7 and in Figure 6.15. As can be seen the  $\frac{B_1}{A_0}$  is clearly non-zero, but  $\frac{B_2}{A_0}$  and  $\frac{B_3}{A_0}$  are not significantly different from zero. However, a good agreement with the data of refs. 6.1 and 6.2 does exist.

Table 6.7: Polarisation Legendre coefficients for  $\Lambda^0\pi^0$  channel

Momentum ( $\frac{\text{MeV}}{c}$ )	$\frac{B_1}{A_0}$	$\frac{B_2}{A_0}$	$\frac{B_3}{A_0}$
280	$0.13 \pm 0.21$	$0.01 \pm 0.37$	$-0.05 \pm 0.41$
327	$0.43 \pm 0.18$	$-0.05 \pm 0.28$	$0.05 \pm 0.37$
360	$-0.11 \pm 0.25$	$-0.02 \pm 0.26$	$0.12 \pm 0.31$
390	$0.31 \pm 0.15$	$-0.36 \pm 0.19$	$-0.11 \pm 0.28$
420	$0.20 \pm 0.18$	$0.05 \pm 0.32$	$0.18 \pm 0.55$
455	$0.52 \pm 0.23$	$-0.36 \pm 0.42$	$0.23 \pm 0.63$

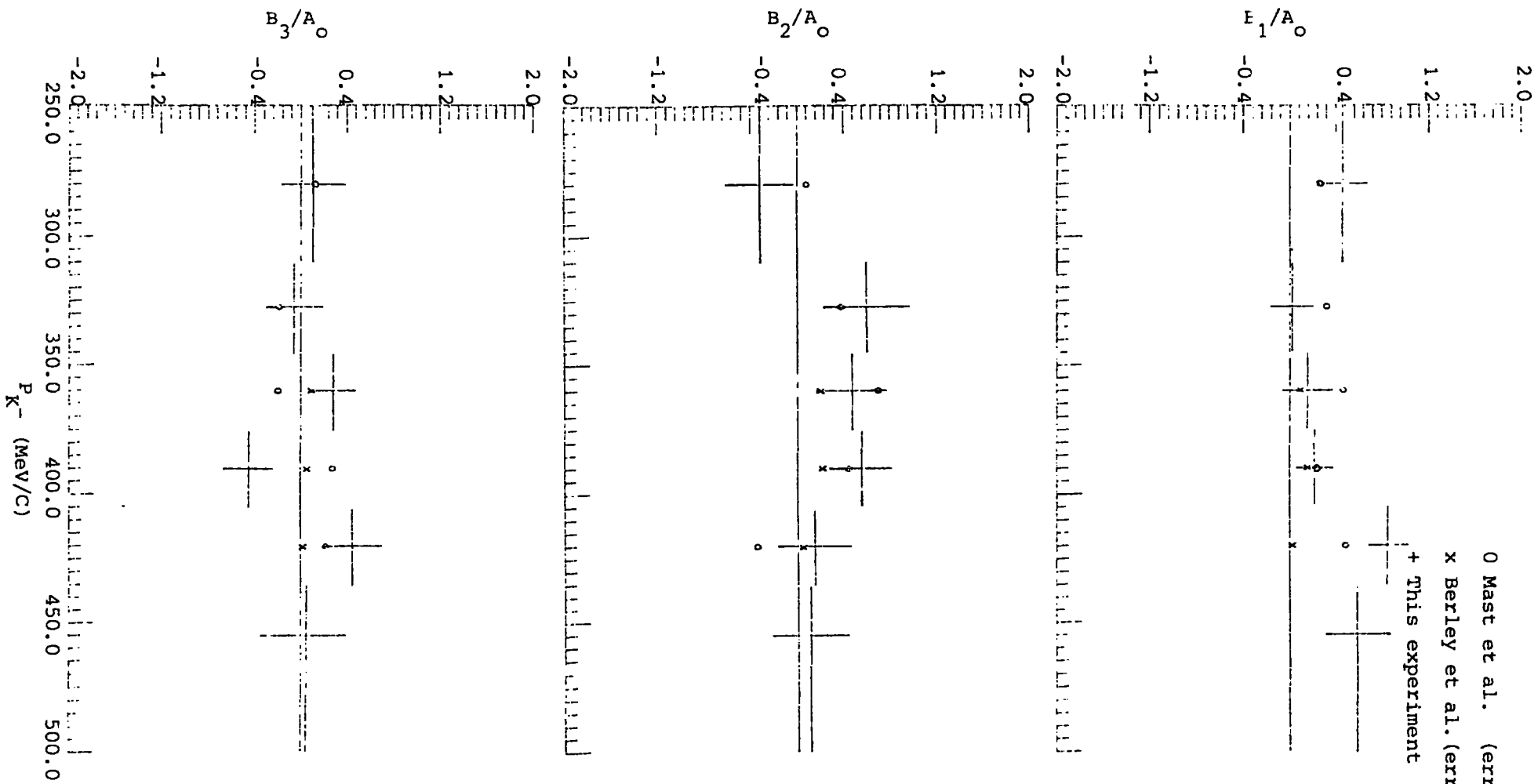


Figure 6.14: Polarisation distribution Legendre coefficients as a function of incident momentum for the reaction  $K^-P \rightarrow \Sigma^0\pi^0$ .  $f$  represents the typical error in this experiment. The momentum bin width is shown by horizontal bars.

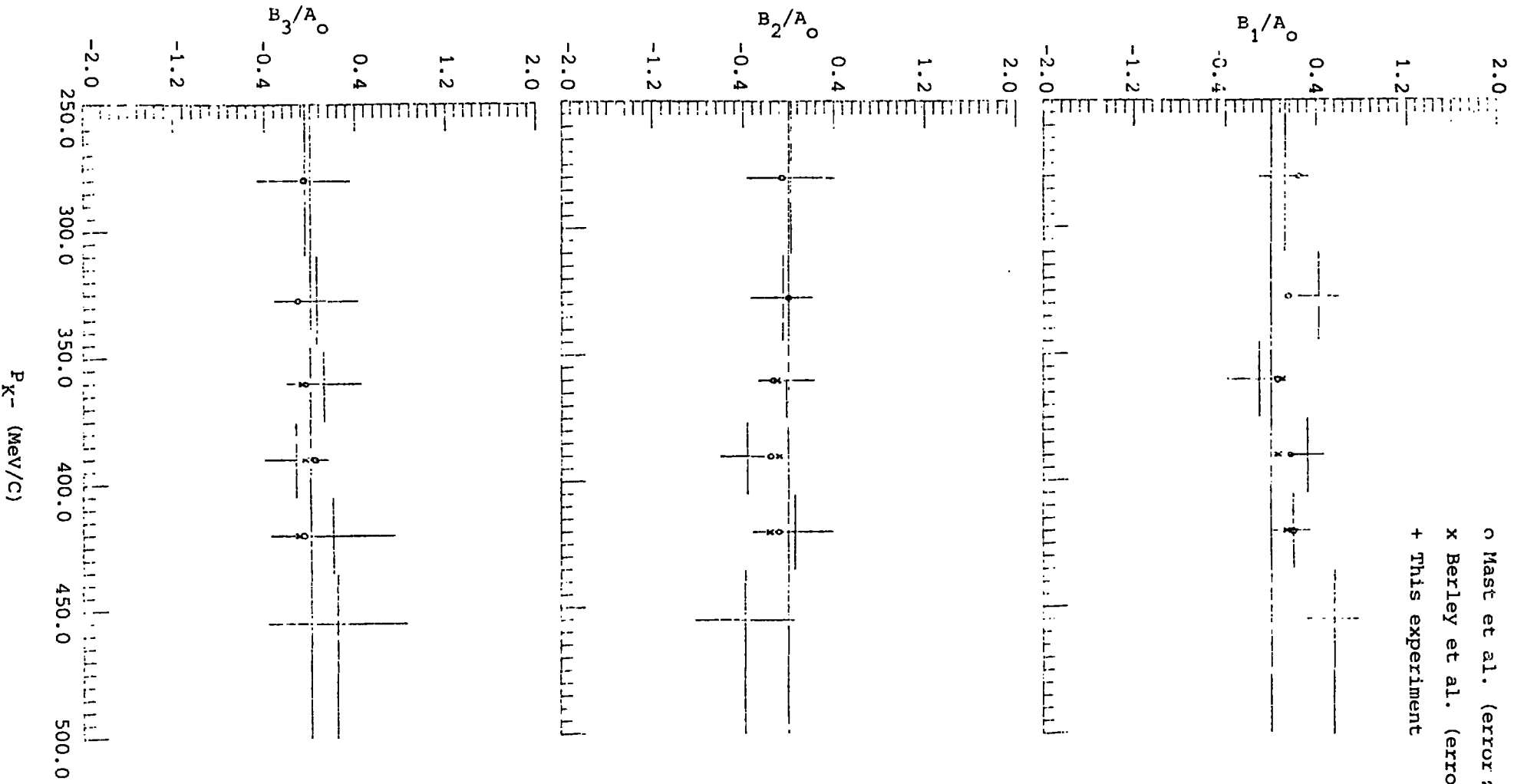


Figure 6.15: Polarisation distribution Legendre coefficients as a function of incident momentum for the reaction  $K^-P + \Lambda^0\pi^0$ . f represents the typical error in this experiment. The momentum bin width is shown by horizontal bars.

#### 6.4 The $\Lambda^0 \pi^0$ and $\Sigma^0 \pi^0$ constrained channels

A fundamental difference between this experiment and the conventional hydrogen bubble chamber experiments is in the detection of gamma-rays ( $e^+ e^-$  pairs). In this section  $\Lambda^0$ -events with one associated gamma-ray are considered. It will be seen that even one associated gamma-ray is enough to make a good separation of  $\Lambda^0 \pi^0$  and  $\Sigma^0 \pi^0$  channels. The results on the angular distribution and polarisation for  $\Lambda^0 \pi^0$  and  $\Sigma^0 \pi^0$  channels are then compared with the weighted average data of references 5.1 and 6.2 which are the two high-statistics experiments within the momentum range of the present experiment.

##### 6.4.1 Separating the Ambiguous $\Lambda^0 \pi^0 / \Sigma^0 \pi^0$ constrained channels

At the time of writing, and with the  $\Lambda^0$  selected within the same criteria as those shown in Table 5.1, a total of 414  $\Lambda^0$ -events were available which fitted the following hypotheses:



The  $(e^+ e^-)$  defines an observed gamma ray for the event. The hypothesis  $K^- P \rightarrow \Sigma^0 \pi^0, \pi^0 \rightarrow \gamma (e^+ e^-)$  cannot be fitted as there are too many missing variables. From the total of 414 events, 178 of them fitted reaction (1), 135 fitted reaction (2) and 101 events were ambiguous between the two reactions. In order to resolve the ambiguity and also as a preliminary check on these events, the angular distribution of the gamma rays in the rest frame of  $\Sigma^0$  was obtained from the  $\Sigma^0 \pi^0$  fitted data. The distribution for unambiguous fits is shown in Figure 6.16, and Figure 6.17 gives the results for the ambiguous events. The distribution for true  $\Sigma^0$ -events is expected to be uniform but as can be seen, it is the combination of the two distributions which is flat. From this, it appears as if a large

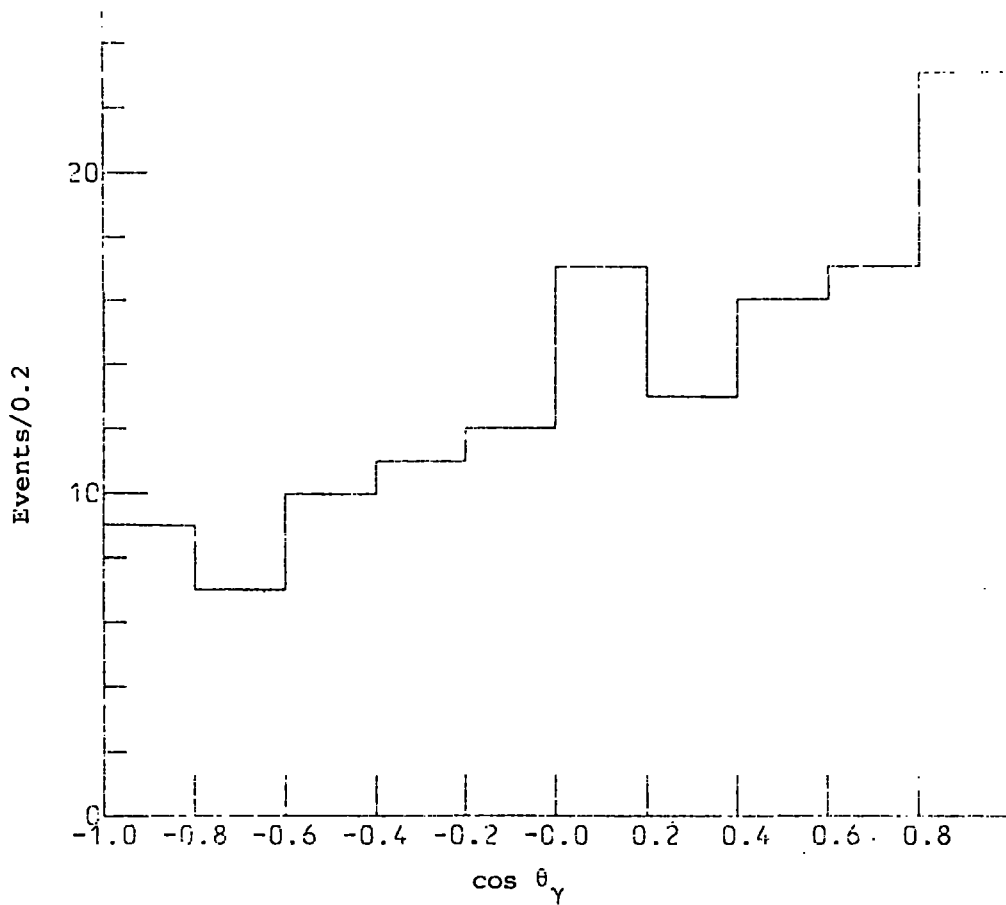


**Figure 6.16:** Gamma ray angular distribution in the rest frame of  $\Sigma^0$  for unambiguous  $\Sigma^0\pi^0$  events.

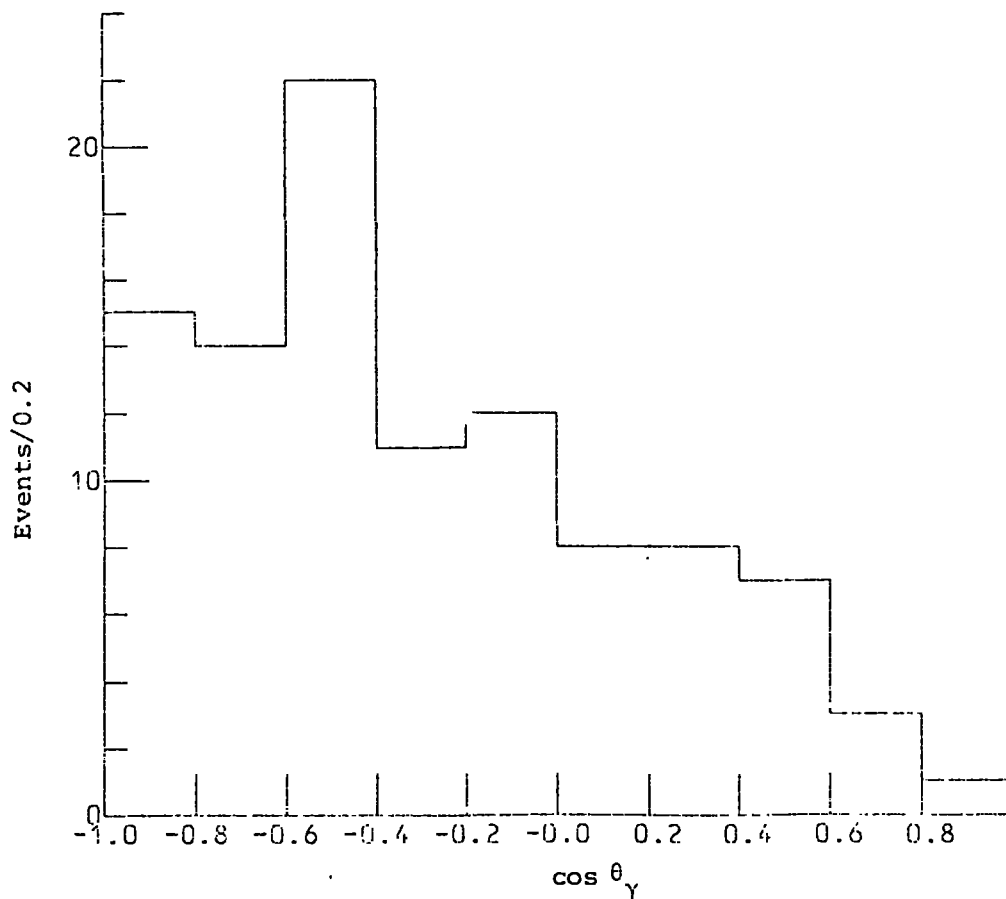


**Figure 6.17:** Gamma ray angular distribution in the rest frame of  $\Sigma^0$  for ambiguous  $\Lambda^0\pi^0/\Sigma^0\pi^0$  events.

majority of the ambiguous events are  $\Sigma^0 \pi^0$ . To check this in an independent approach, the distribution of the square of invariant mass for the  $\Lambda^0$  and gamma ray combination (using the unfitted values for the kinematic variables) was obtained for ambiguous events (Fig. 6.18). As can be seen, there is a large enhancement at  $m_{\Sigma^0}^2$  with a small background. It must be noted that for the ambiguous events, the momentum of one of the electrons was unmeasured for about half of the cases. Because of this there are only 48 events in Figure 6.18. Shown in Figure 6.19 is the square of the invariant mass distribution for  $\Lambda\gamma$  combination for the  $\Lambda^0 \pi^0$  events. This distribution should be flat for true  $\Lambda^0 \pi^0$  events, and Figure 6.19 shows a reasonably uniform shape with evidence of loss in the region of  $m_{\Sigma^0}^2$ . To estimate the loss in this distribution, if any, the mid-point mass squared was calculated  $\left(1.78 \left(\frac{\text{GeV}}{c}\right)^2\right)^*$  and it was then required that the number of events either side of mid-point must be equal. This showed a loss of the order of 10% for the lower half of the distribution which would imply only about 20 events available for the ambiguous class. Therefore, all the ambiguous  $\Lambda^0 \pi^0 / \Sigma^0 \pi^0$  events were taken to be  $\Sigma^0 \pi^0$  and added to the unambiguous  $\Sigma^0 \pi^0$  events. Consequently a sample of 178  $\Lambda^0 \pi^0$  events and a sample of 236  $\Sigma^0 \pi^0$  events became available for further study.

#### 6.4.2 Angular Distributions

The centre of mass production angular distributions (angle between  $K^-$  and hyperon) for the fitted  $\Lambda^0 \pi^0$  and  $\Sigma^0 \pi^0$  events with one gamma ray are shown in Figures 6.20 and 6.21 respectively. Due to the low statistics available for these channels, events with incident  $K^-$ -momentum from 345 to  $435 \frac{\text{MeV}}{c}$  were included in the distributions thus including the  $\Lambda(1520)$ .

---

\* There is a small dependence on incoming  $K^-$ -momentum, which was neglected for this check.

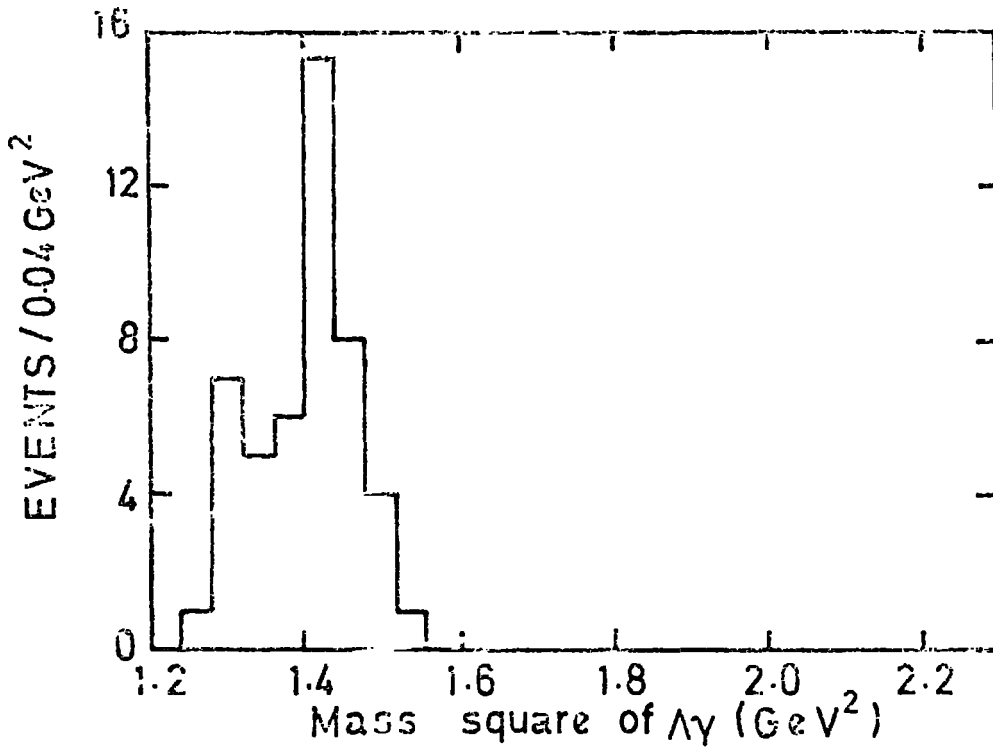


FIG. 6.18 The square of  $\Lambda\gamma$  invariant mass for ambiguous  $\Lambda^0\pi^0/\Sigma^0\pi^0$  events.

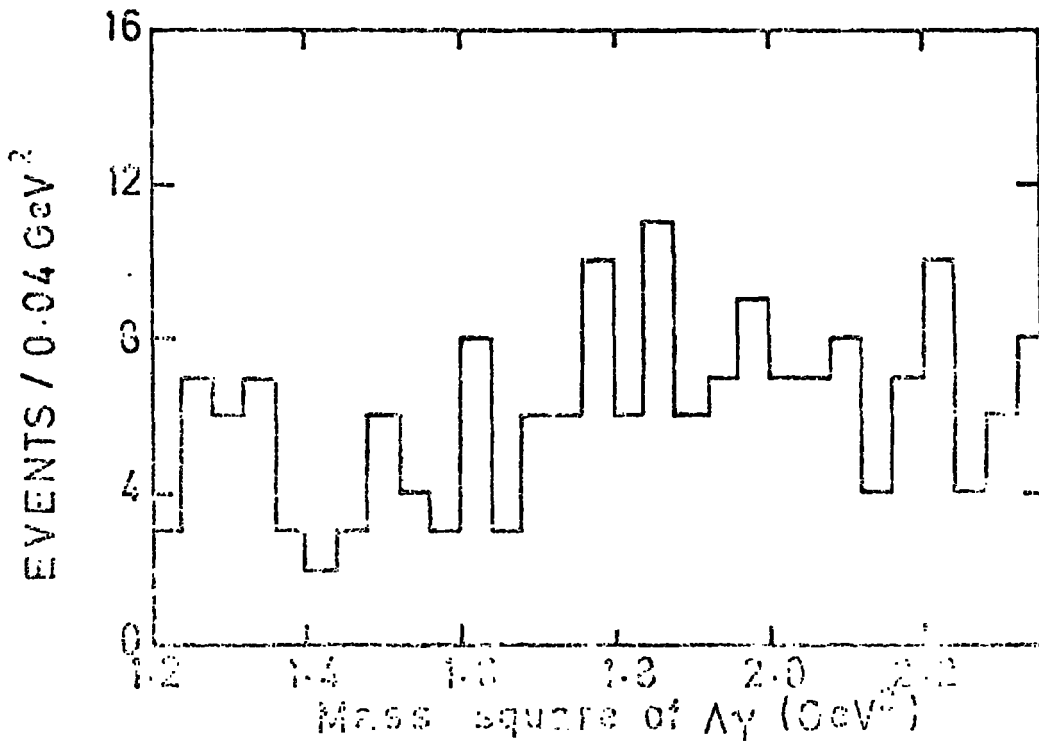


FIG. 6.19 The square of  $\Lambda\gamma$  invariant mass for  $\Lambda^0\pi^0$  events.



The solid curve in each plot is from the fit to Legendre polynomials described in Chapter 6 using the weighted average of the coefficients  $A_\ell$  for the momentum intervals between 345 to 435  $\frac{\text{MeV}}{c}$  (see Table 6.4 and 6.5). As can be seen the agreement is very good. A comparison has also been made between this experiment and the results of the references 6.1 and 6.2 within the same momentum region. For this purpose, the weighted average of the two results for the production angular distribution were plotted in Figures 6.20 and 6.21. These are shown by dashed lines. Again there is a good agreement between the data from the present experiment and the world average.

#### 6.4.3 Polarisation

In order to measure the polarisation, a large number of events is needed. Therefore, with the low statistics available one cannot expect to add significantly to what is already known. Hence in this section only a comparison has been made between the results from the  $\Sigma^0\pi^0$  events with gamma rays and the weighted average data of references 6.1 and 6.2 for the  $\Sigma^0$ -polarisation.

The proton angular distribution from the  $\Lambda^0$ -decay in the  $\Sigma^0\pi^0$  reaction is given by

$$\frac{dN}{d(\cos b)} = \frac{N}{2} (1 + \alpha_\Lambda P_\Lambda \cos b) \quad (6.11)$$

when  $N$  is the number of events,  $\cos b = \hat{n} \cdot \hat{p}$  and  $\hat{p}$  is a unit vector in the direction of the decay proton in the  $\Sigma^0$ -rest frame.  $\hat{n}$  is then the unit vector normal to the production plane defined as

$$\hat{n} = \frac{\vec{K} \times \vec{\Sigma}^0}{|\vec{K} \times \vec{\Sigma}^0|}$$

$\vec{K}$  and  $\vec{\Sigma}^0$  denote incident  $K^-$  and outgoing  $\Sigma^0$ . From equation (6.11), the

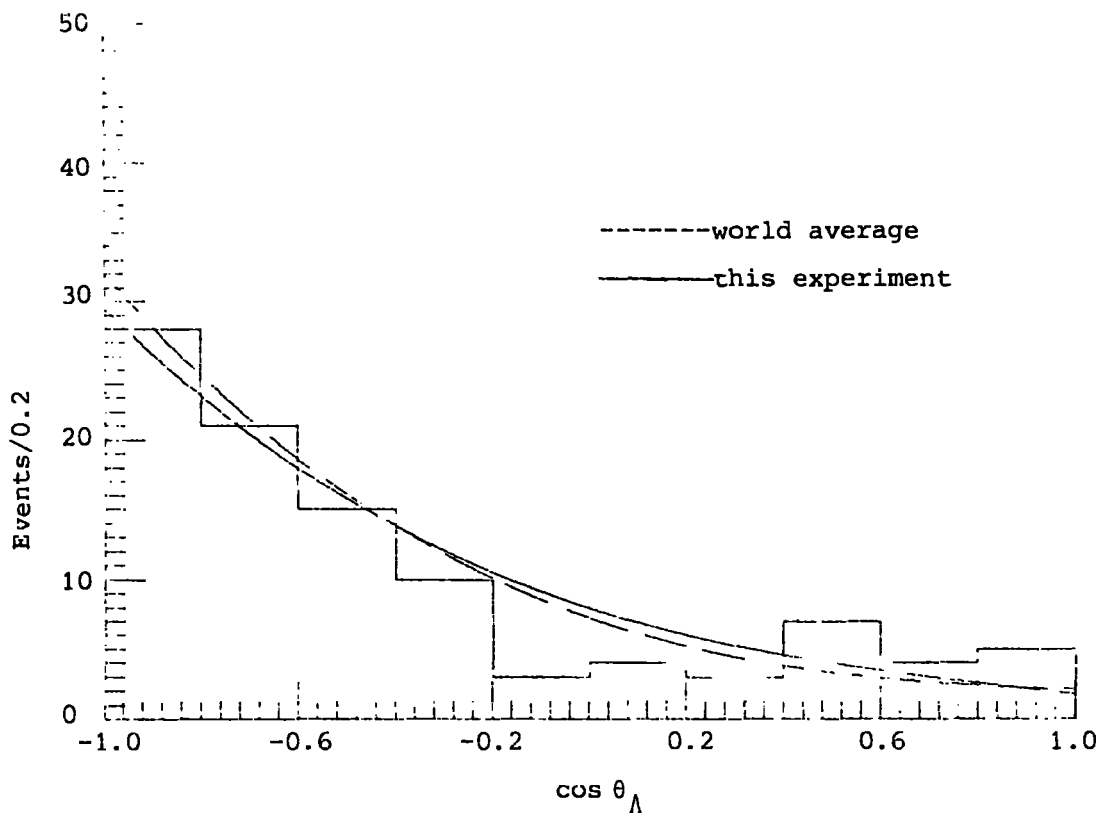


Figure 6.20: Production angular distribution for the fitted  $\Lambda^0 \pi^0$  channel. The curves are from the fitted Legendre coefficients.

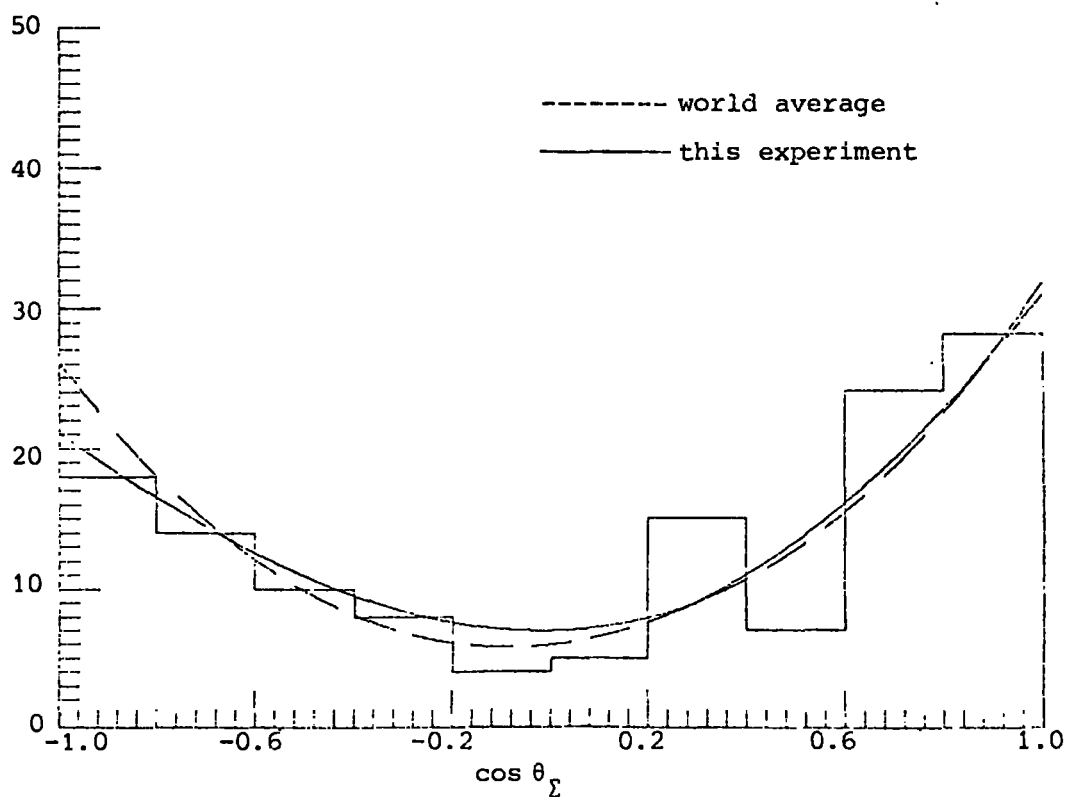


Figure 6.21: Production angular distribution for the fitted  $\Sigma^0 \pi^0$  channel. The curves are from the fitted Legendre coefficients.

average  $\overline{\text{cosb}}$  is given by

$$\overline{\text{cosb}} = \frac{1}{3} \alpha_{\Lambda} \overline{P_{\Lambda}} \quad (6.12)$$

The  $\Sigma^0$ -polarisation can be obtained from the  $\Lambda^0$ -polarisation in the decay of  $\Sigma^0 \rightarrow \Lambda^0 \gamma$  using

$$\vec{P}_{\Sigma} = -3 \vec{P}_{\Lambda} \quad (6.13)$$

Hence

$$\overline{\text{cosb}} = -\frac{1}{9} \alpha_{\Lambda} \overline{P}_{\Sigma} \quad (6.14)$$

where substitution has been made for  $P_{\Lambda}$ .

Events with incident  $K^-$ -momentum between 345 to 435  $\frac{\text{MeV}}{c}$  were divided into two intervals of  $\Sigma^0$ -production angle ,

$$\text{Interval 1} \quad -0.8 \leq \cos\theta_{\Sigma} \leq -0.02$$

$$\text{Interval 2} \quad 0.2 \leq \cos\theta_{\Sigma} \leq 0.8$$

The  $\Sigma^0$ -polarisation is expected to be zero for  $\theta_{\Sigma} = 0^{\circ}$  and  $\theta_{\Sigma} = 180^{\circ}$ .

For each interval  $\overline{\text{cosb}}$  was computed and from equation 6.15, the following results were obtained,

$$\text{Interval 1} \quad \overline{\text{cosb}} = 0.07 \pm .06 \quad (6.16)$$

$$\text{Interval 2} \quad \overline{\text{cosb}} = -0.12 \pm .05$$

To compare this result with that of references 6.1 and 6.2,  $\overline{\text{cosb}}$  were calculated for each interval from the weighted average Legendre coefficients obtained in these references using

$$\overline{P}_{\Sigma} = \frac{\int_{z_1}^{z_2} \sum_{\ell} B_{\ell} P_{\ell}(z) dz}{\int_{z_1}^{z_2} \left[ 1 + \sum_{\ell} A_{\ell} P_{\ell}(z) \right] dz}$$

where  $z \equiv \cos\theta_{\Sigma}$  and  $z_1$  and  $z_2$  are the lower and upper limits of  $\cos\theta_{\Sigma}$  for each interval. The results obtained for  $\overline{P}_{\Sigma}$  are

$$\text{Interval 1} \quad \overline{P}_{\Sigma} = -0.463 \pm 0.11$$

$$\text{Interval 2} \quad \overline{P}_{\Sigma} = 1.109 \pm 0.25$$

It must be noted that, in Interval 2,  $\Sigma^0$  appears to be fully polarised. These values of  $P_{\Sigma}$  are corresponding to the following values for  $\overline{\cos b}$ .

$$\text{Interval 1} \quad \overline{\cos b} = 0.04 \pm 0.01$$

(6.17)

$$\text{Interval 2} \quad \overline{\cos b} = -0.08 \pm .02$$

Comparing the results quoted on 6.16 and 6.17 gives a reasonable good agreement within the errors, but it is clear that the statistics are insufficient for a really significant test.

## CHAPTER 7

### GENERAL CONCLUSIONS

In this thesis a composite chamber has been used consisting of a hydrogen chamber (T.S.T.) inside a second one filled with a neon-hydrogen mixture. The purpose of the surrounding chamber is to enhance the materialisation of gamma rays and these can then be used to detect the presence of neutral pions and to distinguish  $\Sigma^0$  production (where the  $\Sigma^0$  decays to  $\Lambda^0 \gamma$ ) from simple  $\Lambda^0$  production.

The neon-hydrogen mixture consisted of about 70-75% neon (by number of molecules). Since this leads to an expected radiation length associated conversion length for pair production of about 45 cm then it has been possible to measure the  $\lambda$  directly in the composite chamber where total length is 1.5 metres. The value of the conversion length is  $36 \pm \frac{20}{10}$  cm.

Although the chamber was expected to convert about 25% of the  $\gamma$ -rays in practice, at the low momenta of this experiment, approximately 1/3 of the  $\gamma$ -rays have such low energies that the rapid energy loss of their materialised electron-positron pairs makes it impossible to measure them. Consequently the effective materialisation amounted to 14% of the  $\gamma$ -rays.

This raises the question of the viability of the T.S.T. approach to bubble chamber physics. Results from the present experiment are in a preliminary stage, but it is seen quite clearly at the end of Chapter 6 that although the number of  $\Lambda^0$  events with associated  $\gamma$ -rays is quite small, it does lead to a very effective separation of the  $\Lambda^0$  and  $\Sigma^0$  channels which was only possible (in the earlier part of Chapter 6) by a very detailed analysis of the  $MM^2$  distribution to events with  $\Lambda^0$  production. Given adequate statistics, which should be available at the

completion of the experiment, the enhanced  $\gamma$ -materialisation will be seen to be a very effective aid in the analysis of the experiment.

For events without  $\gamma$ -rays it has been seen in Chapter 5 that the narrow T.S.T. has imposed a variety of geometric biases. These have been recognized and identified. Provided suitable selection criteria are imposed (basically of a geometric nature) then the biases can be controlled and corrected for. However, large data samples are required which, again, should be available at the termination of the experiment.

In a sense this thesis describes an experiment to test the usefulness of T.S.T. approach in low momentum kaon physics. It is clear from above (and from detailed results presented in the earlier chapters) that such a chamber can be used successfully. This has been shown by an examination of the data in the region of production of the known  $\Lambda(1520)$ .

The interaction channels reported are  $K^-P \rightarrow \Lambda^0 + \text{neutrals}$  and  $K^-P \rightarrow \bar{K}^0n$ . The momentum range covered was 200 to 500  $\frac{\text{MeV}}{c}$  for cross-sections and 250 to 500  $\frac{\text{MeV}}{c}$  for the rest of analysis. The channels are dominated by the formation of the  $\Lambda(1520)$  at a momentum of 390  $\frac{\text{MeV}}{c}$ . This momentum region has already been reported by two groups having high-statistics (refs. 6.1 and 6.2) for the  $\Lambda^0$ -neutral channel and charge-exchange reaction. The comparisons made in the thesis with the published data, therefore, form a careful calibration of the T.S.T. bubble chamber as well as indicating how high statistics on events with one gamma ray could easily yield definitive results on the separation of  $\Sigma^0\pi^0$  and  $\Lambda^0\pi^0$  channels.

In spite of the limited number of events, the results obtained in this thesis are in a good agreement with those from the high-statistics experiments as discussed briefly below.

The cross-sections for  $\Lambda^0 + \text{neutrals}$  and the charge-exchange channels are consistent, taking into account the momentum resolution,

with the existing data, in particular, the signal from the resonance  $\Lambda(1520)$  is quite marked. Despite the small number of events for the sample of  $\Lambda^0 \pi^+ \pi^-$  events, the cross-section is in a good agreement with that of reference 6.4.

As seen in Figure 6.6, the fraction of  $\Lambda^0$ -events which goes to the  $\Lambda^0 \pi^0$  final state is consistent with the data of reference 6.2 well within the errors, in particular, at incident  $K^-$ -momentum of  $390 \frac{\text{MeV}}{c}$  where the statistics is maximum.

Although a simpler approach in determining the Legendre coefficients describing the angular distribution and polarisation than those adopted in references 6.1 and 6.2, the results are in a good agreement. This is very clear from the coefficients  $\frac{A_2}{A_0}$  and  $\frac{B_2}{A_0}$  in the region of  $\Lambda(1520)$ . Finally events with associated gamma rays seems to lead to effective analysis. This can be seen from Figure 6.20 and 6.21 which compare the angular distributions for the  $\Lambda^0 \pi^0$  and  $\Sigma^0 \pi^0$  constrained channels with the results from fit in the present experiment and with the world average data.

Where this experiment will provide significant new data is in the momentum region below about  $350 \frac{\text{MeV}}{c}$  and between 450 and  $600 \frac{\text{MeV}}{c}$ . Here existing statistics are low and of doubtful quality. What this thesis has shown is that the biases of a T.S.T. chamber can be identified and where these are corrected for the results from the chamber, are in good agreement with those from the largest and most carefully executive experiments of Mast et al. Not only the results are comparable to those from conventional chambers, but with the added information from  $\gamma$ -ray materialisation, the analysis of the data in the lower and higher momentum intervals should be much more penetrating.

APPENDIX A

DERIVATION OF FORMULA (3.1)

The total relative error in momentum of a track can be written in the form

$$\begin{aligned} \left(\frac{dP}{P}\right)^2 &= \left(\frac{dP}{P}\right)_{\text{meas.}}^2 + \left(\frac{dP}{P}\right)_{\text{Coul.}}^2 \quad (\text{A1}) \\ &= \frac{7.8 P}{0.3 H L^2} \left[ f_0^2 + \left( \frac{45}{\beta H \sqrt{\chi_0} L} / \frac{7.8 P}{0.3 H L^2} \right)^2 \right]^{\frac{1}{2}} \end{aligned}$$

where substitution has been made for the terms inside the bracket from eqs. (2.1) and (2.2) respectively (see Section 2.6 for the applied unit). For a given momentum  $P = P_0$ , let  $L_0$  be a typical track length for which,

$$\left(\frac{dP}{P}\right)_{\text{meas.}} = \left(\frac{dP}{P}\right)_{\text{Coul.}}$$

so that, 
$$P_0 = 1.73 L_0^{\frac{3}{2}} / f_0 \beta \sqrt{\chi_0} \quad (\text{A2})$$

and therefore,

$$\begin{aligned} \left|\frac{dP}{P}\right|^2 &= \frac{7.8 P f_0}{0.3 H L_0^2} \left[ 1 + \left(\frac{P_0}{P}\right)^2 \right]^{\frac{1}{2}} \\ &= \left(\frac{dP}{P}\right)_{\text{meas.}} \left[ 1 + \left(\frac{P_0}{P}\right)^2 \right]^{\frac{1}{2}} \end{aligned}$$

Hence the effect of Coulomb scattering in the momentum measurement is equivalent to increasing the measuring inaccuracy  $f_0$  to  $f$  so that ,



$$f = f_o \left[ 1 + \left( \frac{P_o}{P} \right)^2 \right]^{1/2} \quad (A3)$$

In terms of the corresponding radii, (A3) can be written as

$$f = f_o \left[ 1 + \left( \frac{R_o}{R} \right)^2 \right]^{1/2} \quad (A4)$$

Substituting  $P = 0.3 HR$  and  $P_o$  from (A2) in (A3) one gets ,

$$\bar{f} = \bar{f}_o \left( 1 + \frac{C L_o^3}{D^2} \right)^{1/2} \quad (A5)$$

where

$$D = 2R$$

$$C = \left( \frac{11.5}{\bar{f}_o \beta H} \right)^2 \frac{1}{\chi_o}$$

For tracks in hydrogen with  $\beta \sim 1$ ,  $f_o = 0.01$  cm,  $\chi_o = 990$  cm and  $H = 12.33$  Kgauss,  $C$  is of the order of 9.

The on-line system measures the points in the unit of 1 fringe (equal to 25 microns in the y-direction and 50 microns in the x-direction). Therefore describing lengths by this y unit, (A5) will take the following form

$$f = 4 \left( 1 + .02 \frac{L_o^3}{D^2} \right)^{1/2} \quad (A6)$$

where  $L_o$  and  $D$  are in fringes.

Comparing (A6) with eq. (3.1) leads to :

$$C_1 = 4 \quad \text{and} \quad C_2 = .02$$

APPENDIX B

WEIGHTING OF TAU-TRACKLENGTH

In Chapter 5 (see Section 5.3) it was found that the weight which gives the initial number of kaons from the number of seen tau-decays is

$$W(L, P) = 1 / \left[ B \int_0^L \frac{m d\ell}{c \tau P} \right]$$

In deriving the above expression for the weight, the contribution from the strong interactions has not been taken into account. In order to see the effect of the strong interactions in  $W(L, P)$  we proceed as follows:

Assume that  $\lambda_T(P)$  is an effective mean free path for strong interactions and weak decays, then

$$\frac{1}{\lambda_T(P)} = \frac{1}{\lambda_i(P)} + \frac{1}{\lambda_d(P)} = AP^{-S} \quad (B.1)$$

where  $\lambda_i$  and  $\lambda_d$  are the mean free path for interaction and decay respectively. The dependence on momentum is approximated but adequate for the calculation, and  $S$  can be found from the variation of the total  $K^-p$  cross-sections with momentum which is 1.13. The residual range corresponding to the momentum is given by

$$R = K P^n$$

where  $n = 3.6$  and from this relation the momentum of a particle after a distance  $\ell$  from a point where  $P \equiv P_0$  with  $R \equiv R_0$  is

$$P(\ell) = P_0 \left( 1 - \frac{\ell}{R_0} \right)^{1/n} \quad (B.2)$$



so that

$$\frac{1}{\lambda_T(\ell)} = A P_0^{-S} \left(1 - \frac{\ell}{R_0}\right)^{-S/n}$$

The attenuation of the beam is given by

$$-dN(\ell) = N(\ell) A P_0^{-S} \left(1 - \frac{\ell}{R_0}\right)^{-S/n} d\ell$$

which yields

$$N(\ell) = N_0 \exp \left[ \int_0^\ell \left(1 - \frac{\ell}{R_0}\right)^{-S/n} d\ell / \lambda_T(P_0) \right] \quad (\text{B.3})$$

where  $N_0$  is the original number of kaons.

Since  $\frac{\ell}{R_0}$  is small in our momentum region, it is allowed to expand

$\left(1 - \frac{\ell}{R_0}\right)^{-1/n}$  in a binomial series which leads equation B.3 to

$$N(\ell) = N_0 \exp \left[ -\frac{\ell}{\lambda_T(P_0)} \left(1 + \frac{S}{2n} \frac{\ell}{R_0} + \frac{S(1+S)}{6n} \frac{\ell^2}{R_0^2}\right) \right]$$

Also  $\frac{\ell}{\lambda_T} \ll 1$ , so the exponential can be expanded too and therefore

$$N(\ell) = N_0 \left[ 1 - \frac{\ell}{\lambda_T(P_0)} \left(1 + \frac{S}{2n} \frac{\ell}{R_0} + \frac{S(S+1)}{6n} \frac{\ell^2}{R_0^2}\right) + \frac{1}{6} \left(\frac{\ell}{\lambda_T(P_0)}\right)^2 \dots \right]$$

(B.4)

Now, the number of decays in length  $d\ell$  at  $\ell$  is

$$-dN_d = N(\ell) d\ell / \lambda_d(\ell)$$

where

$$\lambda_d^{-1}(\ell) = \frac{m}{c\tau P} = \frac{m}{c\tau P_0} \left(1 - \frac{\ell}{R_0}\right)^{-1/n}$$

which substitution has been made from B.2. Assuming  $L$  is the potential length, then the number of decays within the chamber becomes

$$N_d = \int_0^L N(\ell) \left(1 - \frac{\ell}{R_0}\right)^{-1/n} d\ell / \lambda_d(P_0) \quad (B.5)$$

Integrating B.5 after substituting B.4 for  $N(\ell)$  gives

$$N_d = \frac{N_0 L}{\lambda_d(P_0)} \left[ 1 - \frac{L}{2\lambda_T} + \frac{L}{2nR_0} + \frac{L^2}{18\lambda_T^2} + \frac{n+1}{6n^2} \frac{L^2}{R_0^2} - \frac{S}{6n} \frac{L^2}{\lambda_{TR_0}} \dots \right]$$

Therefore, the observation of a  $\tau$ -decay with entry momentum  $P_0$  and potential length  $L$  implies a total number of kaons entering with those characteristics given by

$$W_i(P_0, L) = \frac{\lambda_d(P_0)}{BL} \left[ 1 - \frac{L}{2\lambda_T} + \frac{1}{2nR_0} \dots \right]^{-1}$$

where  $B$  is the branching ratio ( $\sim 5\%$ ).

To calculate the amount of tracklength per momentum interval, define  $\ell(P_1)$  and  $\ell(P_2)$  as the lower and upper edge of a length corresponding to the momentum interval  $P_1 \rightarrow P_2$ . On average  $W_i(P_0, L)$  kaons contribute a pathlength of  $L_i$  between  $\ell(P_1)$  and  $\ell(P_2)$  such that

$$L_i(P_1, P_2) = \int_{\ell(P_1)}^{\ell(P_2)} N(\ell) d\ell \quad (B.6)$$

$$= \int_{\ell(P_1)}^{\ell(P_2)} W_i(P_0, L) \left[ 1 - \frac{\ell}{\lambda_T(P_0)} - \frac{S}{2n} \frac{\ell^2}{\lambda_{TR_0}} \dots \right]$$

where substitution has been made from B.4.

Integrating B.6 gives

$$L_i(P_1, P_2) = W_i(P_0, L) \left[ \ell \left( 1 - \frac{\ell}{2\lambda_T} \right) + \frac{1}{6} \left( \frac{1}{3\lambda_T^2} - \frac{S}{n} \frac{1}{\lambda_T R_0} \right) \ell^2 \dots \right]_{\ell(P_1)}^{\ell(P_2)}$$

It can be seen from the above relation that the effect of the strong interactions in the amount of tracklength is of the order of  $\frac{\ell}{2\lambda_T}$  which is  $\sim 5\%$  for 50 mb total cross-section.

APPENDIX C

DERIVATION OF EQUATION 5.5

From the decay law, the probability of decay for a tau-meson in length  $l$ ,  $l + dl$  is

$$\frac{dN}{N} = -\frac{dl}{\lambda_d} = -\frac{mdl}{c\tau P} \quad (C.1)$$

where  $\lambda_d = \frac{P}{m} c\tau$  is the decay mean free path. Integrating (C.1) yields

$$\log \frac{N}{N_0} = \int_0^L -\frac{mdl}{c\tau P}$$

where  $L$  is the kaon potential length.

Assuming that  $R = aP^b$  leads to  $dl = -dR = -abP^{b-1}dP$  and

$$\begin{aligned} \log \frac{N}{N_0} &= \int_{P_1}^{P_2} \frac{m}{c\tau} \cdot \frac{ab P^{b-1}}{P} dP = \frac{mab}{c\tau} \int_{P_1}^{P_2} P^{b-2} dP \\ &= \frac{-mb}{c\tau (b-1)} \left( \frac{R_1}{P_1} - \frac{R_2}{P_2} \right) \end{aligned} \quad (C.2)$$

where 1 and 2 refer to the kaon quantities at entrance and exiting of the fiducial volume respectively. From (C.2)

$$N = N_0 \exp \left[ \frac{-mb}{c\tau (b-1)} \left( \frac{R_1}{P_1} - \frac{R_2}{P_2} \right) \right] \quad (C.3)$$

At the entrance to the fiducial volume the number of kaons with momentum  $P, P + dP$  and potential length  $L, L + dL$  is

$$N_0(P, L) dP dL = n_0(P) dP m_0(L) dL$$

by  
experiment

The number of kaons which will survive the potential length L is

$$m(L) dL = m_0(L) dL \exp \left[ \frac{-mb}{c \tau (b-1)} \left( \frac{R_1}{P_1} - \frac{R_2}{P_2} \right) \right] \quad (C.4)$$

in which substitution has been made from (C.3) and it is assumed that

$$R_1 < L.$$

Replacing  $\frac{R}{P}$  by  $a \frac{1}{R} R^{1-1/b}$ ,  $\frac{mb a^{1/b}}{c \tau (b-1)}$  by a constant K and  $R_2$  by  $R_1 - L$ , then

$$m(L) dL = m_0(L) dL \exp \left( -KR_1^{1-1/b} \right) \exp \left[ K(R_1 - L)^{1-1/b} \right]$$

Alternatively the number decaying in  $l (< L)$   $dL$  is

$$\frac{dm(l)}{dL} dL = m_0(L) dL \exp \left( -KR_1^{1-1/b} \right) K \left( 1 - \frac{1}{b} \right) (R_1 - l)^{-1/b} \exp \left[ K(R_1 - l)^{1-1/b} \right]$$

and those decaying by the  $\tau$ -mode are

$$\frac{d\tau(l)}{dL} dL = B \frac{dm(l)}{dL} dL \quad (C.5)$$

where B is the branching ratio for  $\tau$ -decays.

If W is the weighting factor for  $\tau$ -decays then

$$m_0(L) dL = \sum \left[ \frac{d\tau(l)}{dL} dL \cdot W \right] \quad (C.6)$$

Substituting (C.4) and (C.6) in (C.5) gives

$$\frac{d\tau(l)}{dL} dL = B \sum \left[ \frac{d\tau(l)}{dL} dL \cdot W \right] \exp \left( -KR_1^{1-1/b} \right) K \left( 1 - \frac{1}{b} \right) (R_1 - l)^{-1/b} \exp \left[ K(R_1 - l)^{1-1/b} \right] \quad (C.7)$$

If the number of  $\tau$ -decays in bin  $dP$ ,  $dL$ ,  $d\ell$  is shown by  $v$ , then (C.7) can be written in the form of

$$v = B \sum (vw) \exp \left( -KR_1^{1-1/b} \right) K' (R_1 - \ell)^{-1/b} \exp \left[ K(R_1 - \ell)^{1-1/b} \right]$$

which is equation 5.5.



APPENDIX D

CALCULATION OF  $\Delta MM^2$

The error on the missing mass squared ( $\Delta MM^2$ ) were calculated using the following relation ,

$$\begin{aligned} \Delta MM^2 = & \frac{\partial MM^2}{\partial P_K} E\left(\frac{1}{P_K}\right) P_K^2 + \frac{\partial MM^2}{\partial \phi_K} \frac{\partial \phi_K}{\partial P_K} E\left(\frac{1}{P_K}\right) P_K^2 + \frac{\partial MM^2}{\partial \phi_K} E(\phi_K) \\ & + \frac{\partial MM^2}{\partial \lambda_K} E(\tan \lambda_K) \cos^2 \lambda_K + \frac{\partial MM^2}{\partial P_\Lambda} E\left(\frac{1}{P_\Lambda}\right) P_\Lambda^2 + \frac{\partial MM^2}{\partial \phi_\Lambda} E(\phi_\Lambda) \\ & + \frac{\partial MM^2}{\partial \lambda_\Lambda} E(\tan \lambda_\Lambda) \cos^2 \lambda_\Lambda \end{aligned} \quad (D.1)$$

where subscripts K and  $\Lambda$  denote incident  $K^-$  and  $\Lambda^0$ ,  $E(\phi)$ ,  $E(\tan \lambda)$  and  $E\left(\frac{1}{P}\right)$  are the errors on  $\phi$ ,  $\tan \lambda$  and  $\frac{1}{P}$  at the production vertex respectively. The second term in the equation (D.1) accounts for the correlation between the azimuth at the vertex and  $P_K$  at the centre of track. Correlation between other terms assumed to be zero.

By use of equation (6.1),  $\frac{\partial MM^2}{\partial P_K}$ ,  $\frac{\partial MM^2}{\partial \phi_K}$ , ..... could be expressed in terms of the kinematic variables  $P_K$ ,  $P_\Lambda$ , ..... The values of these variables and the errors on them written on the D.S.T. were at the centre of track and, therefore, in order to be used in equation (D.1), they must be swum for charged particles to the production vertex. However, the swum values for the errors on  $\phi$  and  $\tan \lambda$  are only slightly different from those at the centre of track so that central values were used in equation (D.1) for  $E(\phi)$  and  $E(\tan \lambda)$ . Therefore,  $E\left(\frac{1}{P_K}\right)$  was the only quantity which had to be swum to the primary vertex and this was done through the relation,

$$E \left( \frac{1}{P} \right)_V = \left( \frac{P_C}{P_V} \right)^{n+1} E \left( \frac{1}{P} \right)_C \quad (D.2)$$

where C and V denote the centre of track and vertex respectively.

Equation (D.2) was derived by differentiating the range-energy

relation,  $R = KP^n$ , at the centre of track as well as the vertex

and relating the two expressions through the length of the track.

The value of n was taken as 3.6.

APPENDIX E

(a) Derivation of equation (6.7)

From the  $\Sigma^0 \pi^0$  channel, the  $\Sigma^0$ -polarisation must be extracted from that of the observed  $\Lambda^0$ . To do this, choose axes  $\hat{x} = \hat{u}_\Lambda$  and  $\hat{z} = \frac{\hat{u}_\Sigma \times \hat{u}_K}{\sin\theta_\Lambda}$  where  $\hat{u}_\Lambda$  and  $\hat{u}_K$  are unit vectors along the  $\Lambda^0$ -direction and incident  $K^-$  respectively in the laboratory centre of mass (see Figure 6.13).

Consider  $\Lambda^0$  coming from  $\Sigma^0$  which makes an angle  $\chi$  with  $\hat{u}_\Lambda$  and an azimuthal angle  $\phi$  round  $\hat{u}_\Lambda$ , then

$$\hat{u}_\Sigma \times \hat{u}_\Lambda = \sin\theta_\Sigma \hat{u}_{n\Sigma}$$

or

$$\hat{u}_{n\Sigma} = \frac{\hat{u}_\Sigma \times \hat{u}_\Lambda}{\sin\theta_\Sigma} \quad (\text{E.1})$$

where  $\hat{u}_{n\Sigma}$  is a unit vector along the normal to the  $\Sigma^0$  production plane. In terms of angles,  $\hat{u}_{n\Sigma}$  can be written as

$$\begin{aligned} \hat{u}_{n\Sigma} = & \frac{(-\sin\chi \sin\phi \sin\theta_\Lambda)}{\sin\theta_\Sigma} \hat{x} + \frac{(\sin\chi \sin\phi \cos\theta_\Lambda)}{\sin\theta_\Sigma} \hat{y} \\ & + \frac{(\cos\chi \sin\theta_\Lambda - \sin\chi \cos\phi \cos\theta_\Lambda)}{\sin\theta_\Sigma} \hat{z} \end{aligned} \quad (\text{E.2})$$

In the rest frame of  $\Sigma^0$ , the polarisation of  $\Sigma^0$  is along the  $\Lambda^0$ -direction but depends on the  $\Sigma^0$ -production plane normal. Bearing in mind that going from centre of mass to the rest frame of the  $\Sigma^0$  leaves the direction of  $\hat{u}_{n\Sigma}$  and the decay plane of  $\Lambda^0$  unchanged and only the angle  $\chi$  opens up to  $\chi^*$  allows us to write

$$P_\Lambda \hat{u}_{n\Sigma} = -P_\Sigma (\hat{u}_{n\Sigma} \cdot \hat{u}_{\Lambda\Sigma}) \hat{u}_{\Lambda\Sigma} \quad (\text{E.3})$$

where  $\hat{u}_{\Lambda\Sigma}$  is a unit vector associated with  $\Lambda^0$  in the rest frame of

$\Sigma^0$  and can be written as ,

$$\hat{u}_{\Lambda\Sigma} = \cos(\chi^* - \chi) \hat{x} - \sin(\chi^* - \chi) \cos\phi \hat{y} - \sin(\chi^* - \chi) \sin\phi \hat{z} \quad (E.4)$$

Equations (E.2) to (E.4) give,

$$P_{\Lambda} \hat{u}_{\Lambda\Sigma} = P_{\Sigma} \frac{\sin\theta_{\Lambda} \sin\phi \sin\chi^*}{\sin\theta_{\Sigma}} \hat{u}_{\Lambda\Sigma}$$

$\Lambda^0$ -polarisation is measured with respect to the  $\Lambda^0$ -production plane normal. The component of  $\Lambda^0$ -polarisation in this direction is

$$P_{\Lambda} = P_{\Lambda} \hat{u}_{\Lambda\Sigma} \cdot \hat{z} = -P_{\Sigma} \frac{\sin\theta_{\Lambda} \sin^2\phi \sin\chi^*}{\sin\theta_{\Sigma}} \sin(\chi^* - \chi)$$

Now, the probability that an event belonging to  $\Sigma^0\pi^0$  channel is characterised by the angles  $\theta_{\Lambda}$ ,  $b$  and  $\chi$  is

$$\frac{d^3 N}{d(\cos\chi) d(\cos\theta_{\Lambda}) d(\cos b)} = \frac{N_T}{8} \left[ 1 + \sum_{\ell=1}^3 A_{\ell} P_{\ell}(\cos\chi) P_{\ell}(\cos\theta_{\Lambda}) - \frac{\alpha \cos b}{\ell(\ell+1)} \sin\chi^* \sin(\chi^* - \chi) \sin\theta_{\Lambda} \sum_{\ell=1}^3 B_{\ell} P'_{\ell}(\cos\theta_{\Lambda}) P'_{\ell}(\cos\chi) \right]$$

(b) Optimisation of the polarisation

From Figure 6.13, it can be shown that,

$$\cos b^* = \sin\chi^* \sin\phi^*$$

where  $b^*$  is the angle between  $\Lambda^0$  and the normal and  $\phi^*$  is the azimuthal angle of  $\Lambda^0$  with respect to  $\Sigma^0$ , both in the rest frame of  $\Sigma^0$ . For a fixed value of  $\chi^*$ , the average  $|\vec{P}_{\Lambda}|$  over the azimuth  $\phi^*$  (see equation E.3) is

$$\langle | \vec{P}_\Lambda(x^*) | \rangle = \frac{1}{2} P_\Sigma \sin^2 \chi^*$$

calling  $\chi^* = x$  and integrating over  $x$  from  $-x_1$  to  $+x_2$  gives

$$\langle P_\Lambda(-x_1, +x_2) \rangle = \frac{1}{2} P_\Sigma \left( 1 - \frac{x_2^2 + x_1^2 - x_1 x_2}{3} \right)$$

For events with  $MM^2 > 3m_{\pi^0}^2$ ,  $P_\Lambda$  is maximum for  $\cos\chi^* = -0.756$ . The angle  $\chi^*$  is related to  $MM^2$  in the following way:

$$\cos \chi^* = \frac{2MM^2 - (MM_{\min}^2 - MM_{\max}^2)}{MM_{\min}^2 - MM_{\max}^2}$$

where max and min denote upper and lower limit of  $MM^2$ . From this equation  $\cos\chi^* = -0.756$  becomes equivalent to  $MM^2 \approx 6.5 m_{\pi^0}^2$ . The slow variation of  $\chi^*$  with respect to incident  $K^-$ -momentum is ignored in this optimisation.

## ACKNOWLEDGEMENTS

I would like to thank Professors A.W. Wolfendale and B.H. Bransden, who, as sequential heads of the physics department, made available the facilities of the department during my work for this thesis. My particular thanks go to my supervisor, Dr. J.V. Major, who has been a constant source of encouragement and advice in all phases of this work.

I would also like to thank Dr. D. Evans for his many discussions and comments during the course of the work. My thanks are due also to my colleagues in the High Energy Nuclear Physics Group at Durham for their help with various stages of the work, in particular Mr. A.P. Lotts and Dr. P.S. Jones.

The work of all scanning and measuring staff at the University of Durham is gratefully acknowledged.

I would like to acknowledge the financial support of the University of Isfahan and the Ministry of Science and Higher Education, as well as their encouragement during the work.

Lastly, but by no means least, I express my gratitude to my wife, Azam, for all her help and encouragement during the work.

This work was financed by the Science Research Council.

REFERENCES

Chapter 1

- 1.1 William E. Humphrey and Ronald R. Ross, Phys. Rev. 127,  
1305 (1962)
- 1.2 J.K. Kim, Ph.D. Thesis, Coulombia University (1966)
- 1.3 R.H. Dalitz and S.F. Taun, Ann. Phys. (N.Y.) 10, 307 (1960)
- 1.4 R.H. Dalitz and S.F. Tuan, Phys. Rev. Letters 2, 425 (1959)
- 1.5 D. Berley et al., Phys. Rev. D1, 1996 (1970)
- 1.6 T.S. Mast et al, Phys. Rev. 183, 1200 (1969),  
Phys. Rev. Letters 21, 1715 (1968),  
Phys. Rev. D7, 5 (1973),  
Phys. Rev. D7, 3212 (1973),  
Phys. Rev. D11, 3078 (1975),  
Phys. Rev. D14, 13 (1976).
- 1.7 M.B. Watson et al., Phys. Rev. 131, 2248 (1963)
- 1.8 Particle Data Group, Rev. Mod. Phys. 48, pt.2 (1976)
- 1.9 J.K. Kim, Phys. Rev. Letters 27, 356 (1971)
- 1.10 R. Armenteros et al. Nucl. Phys. B21, 15 (1970)
- 1.11 Bowen et al., Phys. Rev. D 2, 2599 (1970)
- 1.12 D. Tovee et al., Nucl. Phys. B 33, 493 (1971)
- 1.13 A.D. Martin, Phys. Lett. 65 B, 346 (1976)
- 1.14 C.M. Fisher, Proceedings of 1973 International Conference on  
Instrumentation for High Energy Physics, Frascati, pg.21
- 1.15 M. Chretien et al., Nucl. Instr. And Meth. 20, 120 (1963)
- 1.16 P. Musset and P. Queru, Ind. Atomiques 67, 8 (1964)
- 1.17 M. Goldhaber, BNL (unpublished)
- 1.18 W.B. Streett and C.H. Jones, J. Chem. Phys. 42, 3989 (1965)
- 1.19 H. Leutz, CERN/TC/BEBC, 66-21 (1966)

- 1.20 CERN-DESY Collaboration, R. Florent et al., Nucl. Instr. And Meth. 56, 160 (1967)
- 1.21 Referring to Figure 1.1, the abbreviations and references are:
- LBL 1965: see reference 1.6
- HYBUC 1973: R. Settles, private communication
- BMV 1965: see reference 1.5
- CHS 1967: see reference 1.10
- CHM 1970: H. Oberlack, private communication
- Tenn. Mass 1969: E. Hart, private communication
- BNL 1964: D. Berley et al., Phys. Rev. Letters 15 64 (1965)
- CHS 1964: R. Armentoros et al., Nucl. Phys. B 8, 233 (1968)
- Mary'd 1964: R.P. Vhlig et al., Phys. Rev. 155, 1448 (1967)
- LBL 1964: D.F. Kane, Phys. Rev. D 5, 1583 (1972 $\mu$ )
- Ch. LBL 1970: D. Merrill et al., Berkeley APS Meeting 1973
- RHEL-ICL: G. Kalms, private communication
- CERN 1968: M. Ferro-Luzzi, CERN/D.Ph. 11 Phys. 71-9
- Saclay 1969: M. Ferro-Luzzi, ibid
- LBL 1962: D.O. Huwe, Phys. Rev. 181, 1824 (1969)
- CRS 1967: P.J. Litchfield et al., Nucl. B 30 , 125 (1971)
- CH 1969: M. Ferro-Luzzi, ibid
- UCLA 1962: P.M. Dauber, UCLA Report 90024 (Thesis) (1966)
- K: see reference 1.2
- CK: J. Chan and J. Kadyk, private communication of an unpublished Berkeley experiment

## Chapter 2

- 2.1 W.T. Welford, Applied Optics, Vol. 2, 981 (1963)
- 2.2 J.F. Ayres et al., Nucl. Instr. And Meth., 107, 131 (1973)



- 2.3 H. Leutz, P.R. Williams, Proceedings of 1973 International Conference on Instrumentation for High Energy Physics, Frascati, pg.60.
- 2.4 C.M. Fisher, Design study for a high magnetic field hydrogen bubble chamber for use on NIMROD, RHEL/S/101, Chapter 2.
- 2.5 Geometry program manual, Computer applications group, RHEL, Didcot.

### Chapter 3

- 3.1 The Geometrical reconstruction of bubble chamber tracks, J.W. Burren and J. Sparrow, NIRL/R/14
- 3.2 Theoretical Studies Group, RHEL, Didcot
- 3.3 D. Evans and G. Fleming, Durham University, private communication

### Chapter 4

- 4.1 Y.A. Hamam, Durham University, private communication

### Chapter 5

- 5.1 T.S. Mast et al., Phys. Rev. D 11, 3078 (1975) and D 14, 13 (1976)

### Chapter 6

- 6.1 D. Berley et al., Phys. Rev. D 1, 1996 (1970)
- 6.2 T.S. Mast et al., Phys. Rev. D 11, 3078 (1975)
- 6.3 T.S. Mast et al., Phys. Rev. D 14, 13 (1976)
- 6.4 T.S. Mast et al., Phys. Rev. D 7, 5 (1973)
- 6.5 T.S. Mast et al., Phys. Rev. Letters 21, 1715 (1968)
- 6.6 MINUIT Long Write-up CERN Computer Program Library, F. James and M. Reos D506, D516 (1971)

